# Study of the $\nu_\mu$ interactions via charged current in the T2K near detector

**Alfonso Andrés García Soto**

Tesis presentada para optar al grado de

DOCTOR EN FÍSICA

---

**Supervisada por:**

Dr. Federico Sánchez Nieto (Director)

Dr. Enrique Fernández Sánchez (Tutor)

**y evaluada por:**

Dr. Juan Antonio Caballero Carretero (Presidente)

Dra. Lluïsa-Maria Mir (Secretaria)

Dr. Kenneth Long (Vocal)

**Cerdanyola (Barcelona), 15 de Mayo de 2017**

# Part IV

# Appendices

# Appendix A

# SMRD and ECAL Fiducial Volume

The momentum by range is computed using the length of a track and the energy loss (under certain particle hypothesis) within certain volume. Therefore, in order to reconstruct the momentum by range the track must be fully contained in ND280 volume.

In this analysis, BarrelECal and SMRD subdetectors were used to compute the momentum by range for tracks with no reliable TPC information (see Sec. 8.5). It was found that the performance of such variable, in terms of bias and resolution, is not acceptable when the track ends at the edges of these subdetectors. Therefore, it has been decided to reduce the fiducial volume in which tracks must finish.

In BarrelECal, the idea has been to remove the edge layer in XYZ. The size of the layers is $10 \times 10 \times 40$ mm$^3$. In SMRD, roughly quarter of a counter has been remove ($60 \times 60 \times 125$ mm$^3$). Fig. A.1 shows an scheme of the fiducial volume used in both subdetectors.

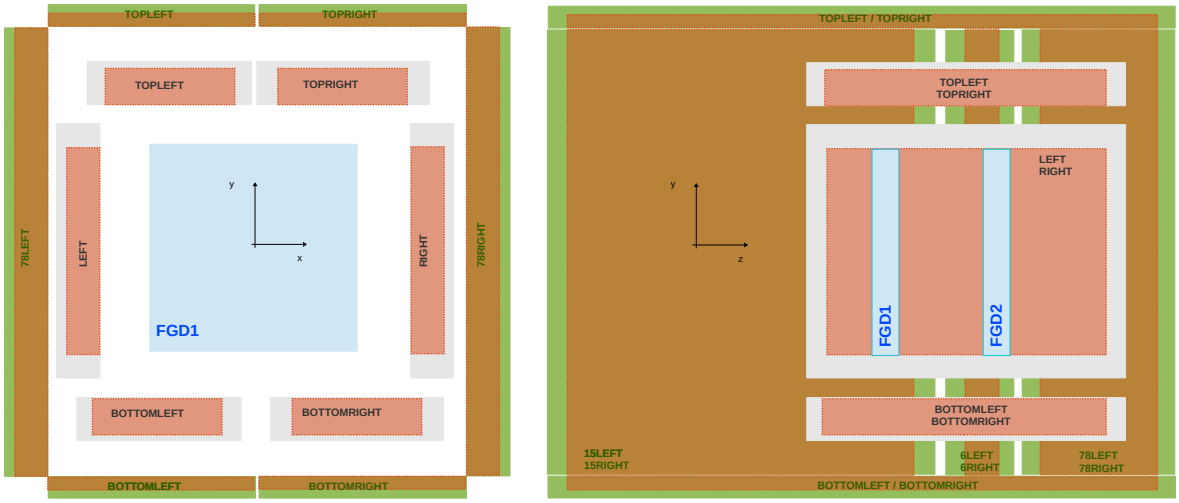


Figure A.1: Schematic view of BarrelECal (gray), SMRD (green) and FGD (blue) subdetectors of ND280. Orange boxes indicate the fiducial volume of each subdetector.

# Appendix B

# Electric Field Distortions in ND280 TPCs

Electromagnetic fields are one of the key ingredients of the TPC track reconstruction. Most of the simulation steps are performed using Geant4, which does not take into account non uniformities for these fields. Therefore, detector simulation of ND280 assumes homogeneous field while in reality distorted fields are possible. Consequently, these distortions must be understood, parametrized and corrected on data.

On the one hand, the motion of charge particles will be deflected when they cross a magnetic field. A perfect magnetic field configuration, $\vec{B} = (0.2\ \mathrm{T}, 0, 0)$, is currently used for the MC simulation. Nevertheless, from calibration using Hall probes, it is known that the magnetic field has distortions specially in the TPC3 region (see Sec. 6.3.1). These distortions are corrected on data using the measured magnetic field information (see Sec. 9.3.1).

On the other hand, electric field in the TPCs is used to drift the electron cloud, produced by ionization of the gas, towards the MM (see Sec. 6.3.6). In the presence of an electromagnetic field, the motion of the electrons can be characterized by the Langevin equation:

$$\vec{v} = \frac{\mu}{1+\omega^2\tau^2}\left[\vec{E} - \frac{\omega\tau}{|\vec{B}|}(\vec{E}\times\vec{B}) + \frac{\omega^2\tau^2}{\vec{B}^2}(\vec{E}\cdot\vec{B})\vec{B}\right] \tag{B.1}$$

Ideally, the electric field should have only an X component (parallel to the magnetic field) so that the drift velocity $\vec{v}$ is parallel to X. However, small distortion of this field can be found (possibly due to inhomogeneities of the TPC geometry). As for the magnetic field, MC assumes a perfect electric field, so a correction on data should be applied in order to remove such distortions.

To quantify the electric field distortions in the TPCs, a hit-track residuals study is performed using information from the reconstruction. The idea is to select tracks crossing the TPC and to measure the residuals between the fitted and raw Y position of the hits in each pad column of the MicroMegas (MM). If the magnetic field was properly corrected previously, the distribution of the residuals should

be centered at zero. Consequently, any deviation from zero can be caused by electric field distortions.

In the following sections, a detailed explanation of the hit-track residuals study is shown. Firstly, a control sample will be produced. Secondly, the hit-track residuals maps will be obtained for each TPC and readout plane (RP) independently. Thirdly, those maps will be fitted using a model that reproduce E field distortions. Finally, distortion will be corrected in data and the impact of this correction in the momentum resolution will be studied.

## B.1 Hit-track Residuals

The first step is the design of a control sample. This selection skims events with tracks having very small X angles (i.e. parallel to the MM plane). An event is selected when at least one TPC segment is found with the following features:

- The transverse momentum higher than 3 GeV/c. This condition is included to use only tracks with small curvature.
- The number vertical pad columns activated is higher than 60 (two consecutive MM have 36×2=72 vertical modules).
- The distance along X between the beginning and the end of the segment is lower than 45 mm and the cathode is not crossed.

This selection criteria is run over data using spill and cosmic $\mu$. It is important to notice that the magnetic field correction is already applied in those events. Fig B.1 shows some of the main features of the tracks contained in the control sample, in which each entry of the histograms does not represent an individual track but its associated clusters.

The hit-track residuals can be obtained for each reconstructed segment in the TPC using the following methodology:

- Fit the full segment and save the projected angle in the XZ plane, diffusion and curvature parameters.
- Fit again the track fixing the saved parameters.

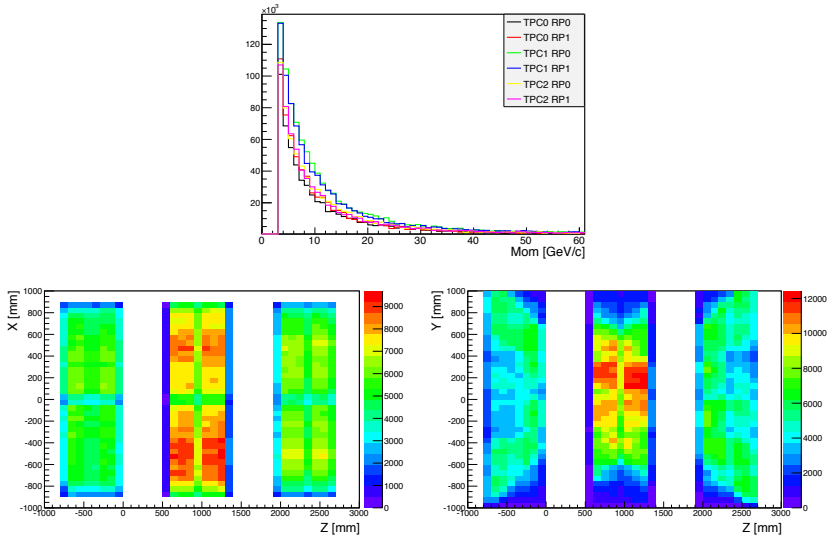


Figure B.1: Left: Momentum distribution (top) and 2D distributions for the Z versus X position (bottom left) and Z versus Y position (bottom right) for each track that fulfills the previous requirements.

- In both fits, evaluate the value of y in each vertical pad column in the MM.

- Compute the residuals of the position for each pad column $i$ of the MM using $y^i_{BIAS} = y^i_{global} - y^i_{local}$.

These residuals (maximum of 72 per segment) are computed for all TPC segments from the control sample. Then, a map containing such information (so called, distortion map) can be computed grouping the segments depending on their X position within the TPCs. With current statistics, it was decided to group the segments in 10 different regions along X for each drift volume (3 TPC $\times$ 2 RP = 6 drift volumes) as shown in Fig. B.2. $y^i_{BIAS}$ distribution is obtained for each column pad $i$ of the MM in each drift volume. Finally, the distortion maps are obtained using the mean and width of $y^i_{BIAS}$ distributions.

Fig B.3 shows the mean and width of the $y_{BIAS}$ distribution for very forward going segments ($\theta_{YZ} \sim 0$) crossing three different volumes in the middle region along X and in the positive or negative region along Y. Fig. B.4 shows the distortion maps in different regions of the TPC along the X axis and different angular conditions.

From these maps it can be concluded that the distortion shows a dependency on the X position and on the $\theta_{YZ}$ angle but not on the Y coordinate.

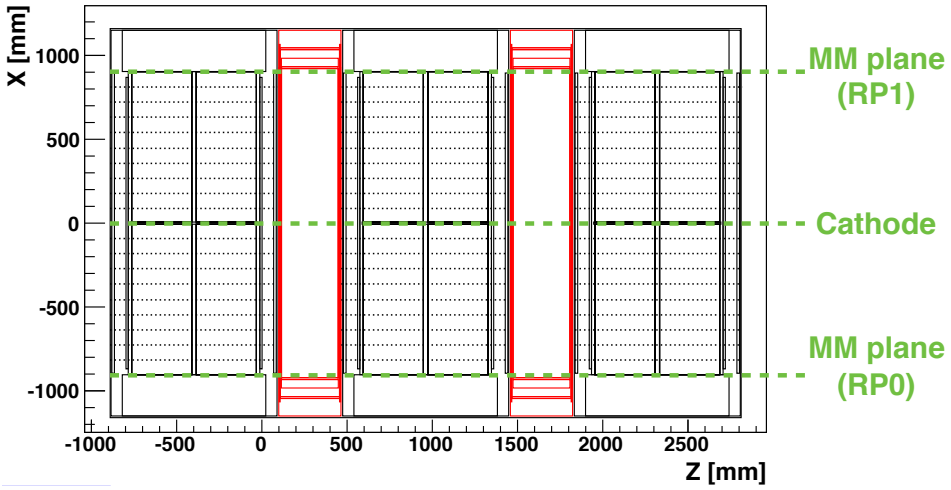


Figure B.2: Schematic view of the three TPCs (black) and two FGDs (red). Dashed lines indicate the different regions along X used for the hit-track residuals maps.

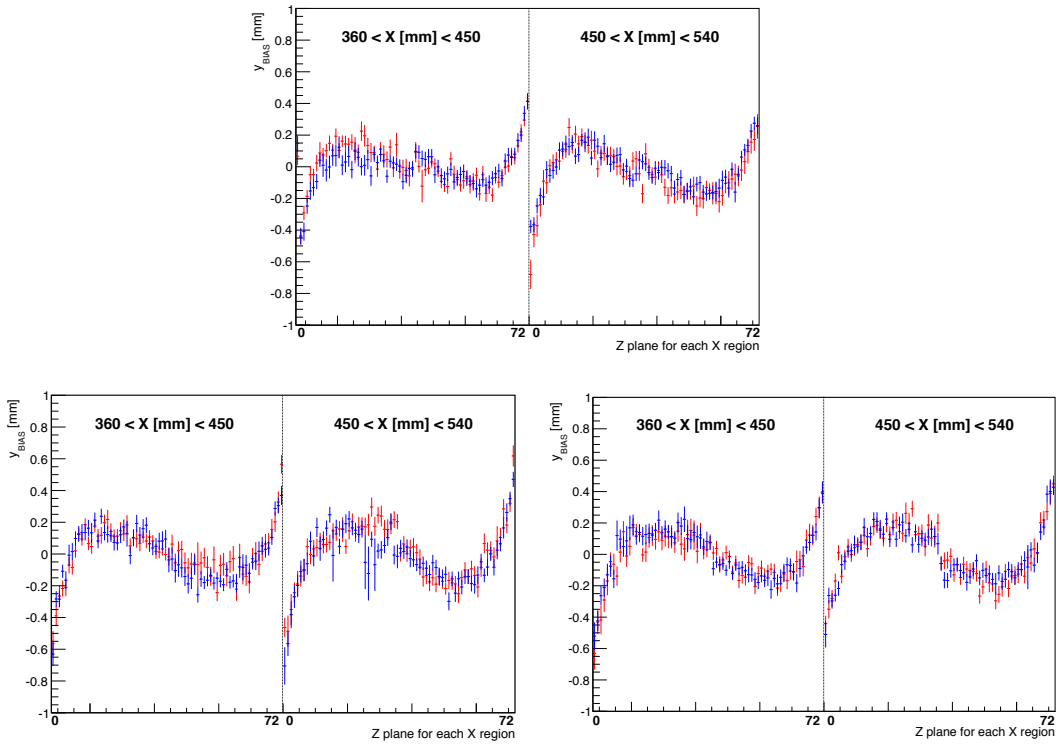


Figure B.3: Distortion map for TPC1-RP1 (left), TPC2-RP0 (middle) and TPC3-RP0 (right) in the middle region along the X axis and for very forward angles. Red (blue) line shows clusters with its Y position higher (lower) than zero.

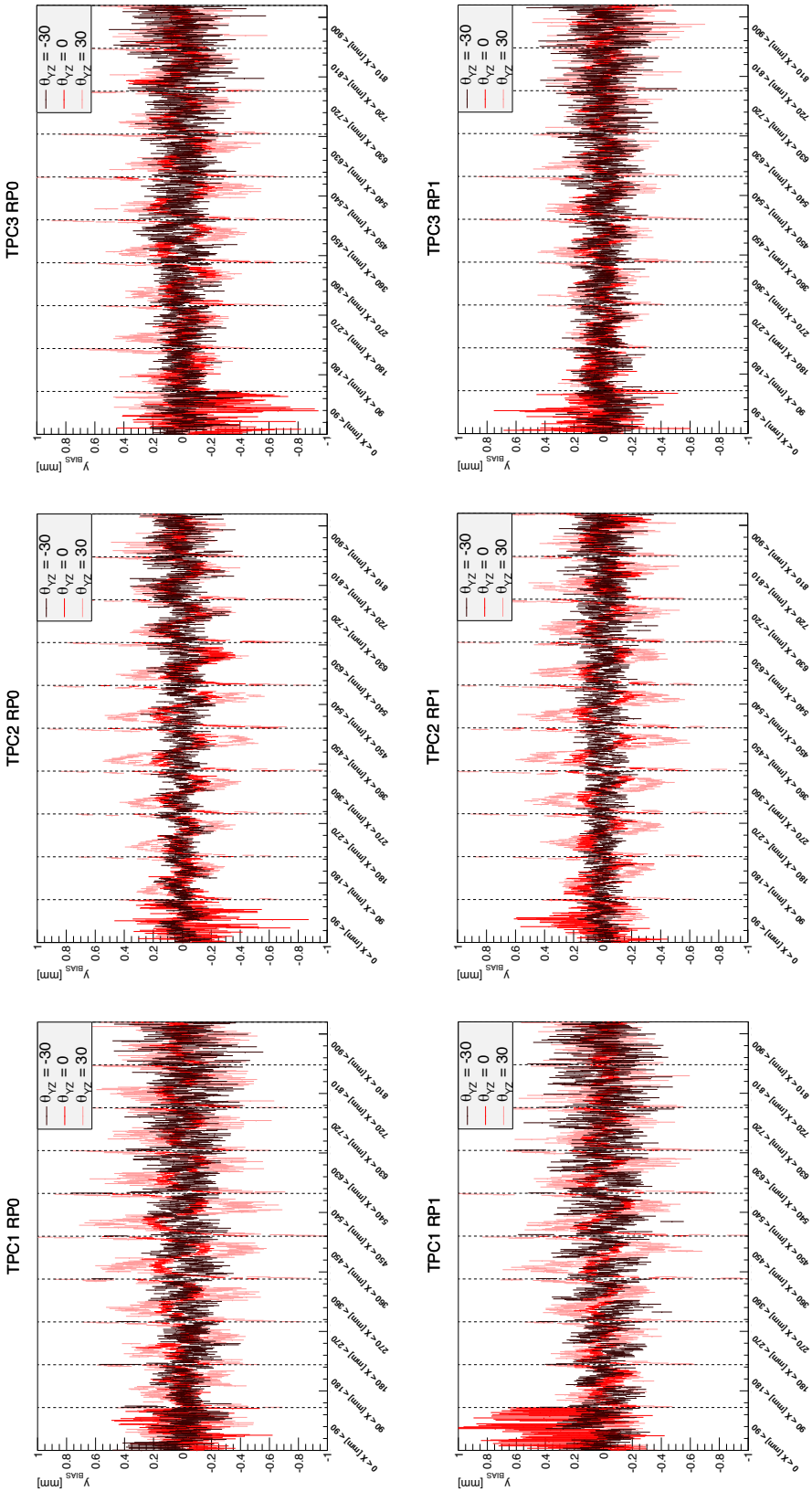


Figure B.4: Distortion map for each TPC and RP for data from the control samples in which magnetic field distortions has been corrected. It shows the profiled $y^i_{bias}$ for each pad column $i$ in each X region. Dashed lines indicate each X region where the first block is the X region closer to the cathode and the last block the one closer to the anode.

## B.2 E Field Model

The idea is to construct an electric potential $\phi$ (decoupled from the homogeneous electric field) that can reproduce the behavior observed in the distortion maps shown in Fig B.4.

To begin with, two approximations will be used.

- The potential does not depends on the Y coordinate (see Fig B.3).

- The drift volume of the TPC is a free-charge region of space (i.e. the charge density is zero).

Therefore, the potential should follow the 2D Laplace equation in the XZ plane:

$$\nabla^2\phi(z,x) = 0 \implies \frac{\partial^2}{\partial z^2}\phi(z,x) + \frac{\partial^2}{\partial x^2}\phi(z,x) = 0 \tag{B.2}$$

Particularly important is the definition of the boundary conditions for this equation, which has been inferred using the distortion maps from Fig B.4.

- The residuals are centered at 0 when the TPC segments are close to the cathode or anode. Besides, the shape of the residuals has a symmetric behavior towards the central region of the drift volume. This fact suggests that the charge accumulation (due to distortions) in the cathode, anode and middle region of the drift volume is negligible ($\phi(z,0) = \phi(z,L) = \phi(0,L/2) \sim 0$ where $L$ is the length in X of the drift volume).

- The shape of the residuals in each region along the X axis is symmetric between the first and second half of the pad columns. Consequently, a similar charge accumulation can be assumed in both walls of the drift volume ($\phi(+K/2,x) = \phi(-K/2,x) = f(x)$ where $K$ is the length in Z of the drift volume).

Thus, Eq. B.2 can be solved assuming previous boundary conditions using the separation of variables

method. The potential can be expressed as follows:

$$\begin{aligned}\phi(z,x) &= \sum_{n=0}^{\infty} A_n sin\left(\lambda_n^{1/2}x\right)\frac{\cosh\left(\frac{1}{b_n}z\right)}{\cosh\left(\frac{1}{b_n}\frac{K}{2}\right)} \\ A_n &= \frac{2}{L}\int_0^L f(x)\sin\left(\lambda_n^{1/2}x\right)dx \\ \lambda_n &= \left(\frac{1}{b_n}\right)^2 = \left(\frac{2\pi n}{L}\right)^2\end{aligned} \tag{B.3}$$

Furthermore, if the drift volume is split in two regions along X and the $|f(x)|$ is the same for the two regions, then a relation between $A_n$ parameters can be obtained. If the sum is truncated in the third term, the following potential is obtained:

$$\begin{aligned}\phi(z,x) = A_1\Bigg[&0.1345\sin\left(\frac{2\pi}{L}x\right)\cosh\left(\frac{2\pi}{L}z\right) + 0.0046\sin\left(\frac{4\pi}{L}x\right)\cosh\left(\frac{4\pi}{L}z\right) \\ &+0.0002\sin\left(\frac{6\pi}{L}x\right)\cosh\left(\frac{6\pi}{L}z\right)\Bigg]\end{aligned} \tag{B.4}$$

Obviously, several assumptions where made to obtain the potential from Eq. B.4 so this model will not reproduce the real electric distortion in the TPC. However, it can give a first order estimation of the distortion shape. Fig. B.5 shows the value of the distorted electric field for one of the drift volumes in the X and Z coordinates using this potential when $A_1 = 1$ V ($E_y = 0$ in this model).

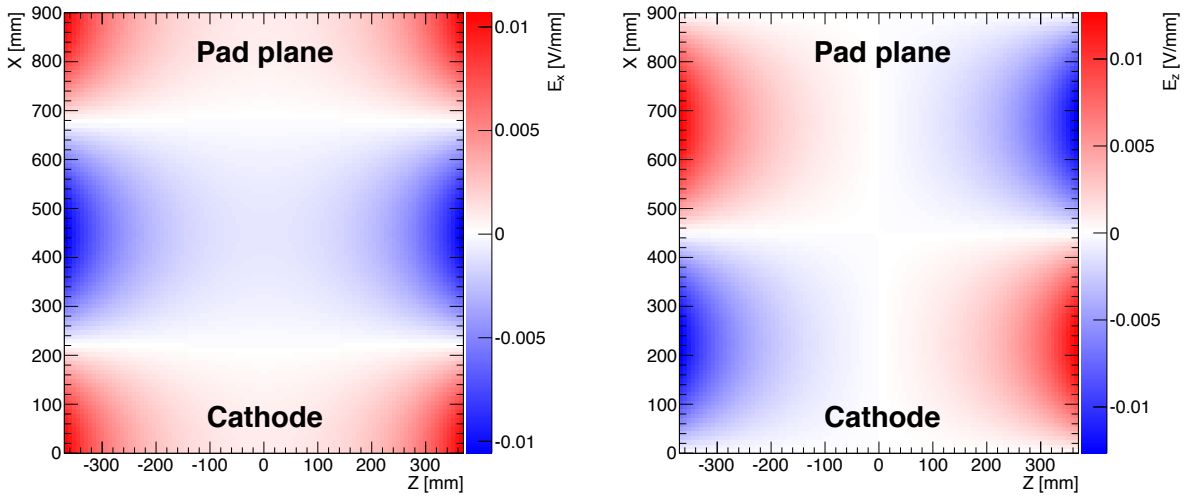


Figure B.5: Distorted electric field for one drift volume in the X (left) and Z (coordinates) coordinates using Eq. B.4 when $A_1 = 1$ V.

## B.3 Fitter

Once the electric potential is parametrized, the next step is to obtain the strength of those parameters comparing the model with the data. The model defined in the previous section had only one free parameter, so some extra parameters have been included in order to give more freedom to the model:

$$\phi(z,x) = \mathbf{A}\left[\sin\left(\frac{2\pi}{L}x\right)\cosh\left(\frac{2\pi}{L}z\right) + \mathbf{c}\cdot\sin\left(\frac{4\pi}{L}x\right)cosh\left(\frac{4\pi}{L}z\right) + \mathbf{d}\cdot\sin\left(\frac{6\pi}{L}x\right)\cosh\left(\frac{6\pi}{L}z\right)\right] \tag{B.5}$$

Where the free parameters are marked in bold. Many distortion maps can be generated from MC varying the parameters of the electric potential.

Firstly, 72 electron clouds are simulated placing them at the pad plane and in the middle of each pad column. Then, those clouds are drifted back to the center of the 10 regions along X using Eq. B.1 (assuming homogeneous B field). Finally, their new Y positions are fitted with a straight line to reproduce the tracking (this is the main motivation for the 3 GeV/c cut in momentum) and the residuals are computed for that variable.

All the simulated distortion maps can be compared with the observed ones. Then, a fit is performed to extract the parameters of the electric potential that minimized the following $\chi^2$ for each TPC and RP:

$$\chi^2 = \sum_{i=0}^{\#pads} \frac{(y^i_{bias,DATA} - y^i_{bias,MODEL}(A,c,d,e))^2}{2\sigma(y^i_{bias,DATA})^2} \tag{B.6}$$

This minimization includes an extra degree of freedom, so called **M**. This parameter is able to account for the MM misalignment in an effective way. It shift up or down the prediction for the first 36 pad columns and the opposite for the other half. It is important to notice that this parameter is not included as part of the electric potential (which is independent from the misalignment).

This minimization is very complicated because it uses several degrees of freedom that can be highly correlated. Therefore, it is not desirable to use a very complex model for the potential. It has been tried to include free parameters in the phases, to add odd terms in the sum or to increase the dimensions of the potential from Eq. B.4. Adding this extra level of complexity does reduce the $\chi^2$ but the correlation between the parameters and the computational time increases.

The correlation problem is partially overcome a defining range of validity for the free parameters (using the order of magnitude obtained Eq. B.4). Besides, some of the parameters can be useless and this

would slow down the minimization process. Fig B.6 compares the distortion maps for the data and the best fit potential. The best fit parameters are shown in Table B.1.

| | A [V] | c ($\times 10^{-4}$) | d ($\times 10^{-5}$) | M ($\times 10^{-3}$) [mm] |
|---|---|---|---|---|
| TPC1-RP0 | $0.73 \pm 0.01$ | $-22 \pm 8$ | $177 \pm 7$ | $60 \pm 3$ |
| TPC1-RP1 | $-0.75 \pm 0.01$ | $-6 \pm 8$ | $113 \pm 7$ | $-103 \pm 3$ |
| TPC2-RP0 | $0.72 \pm 0.01$ | $47 \pm 8$ | $150 \pm 6$ | $44 \pm 3$ |
| TPC2-RP1 | $-0.75 \pm 0.01$ | $93 \pm 8$ | $126 \pm 6$ | $23 \pm 3$ |
| TPC3-RP0 | $0.66 \pm 0.01$ | $20 \pm 10$ | $113 \pm 8$ | $28 \pm 3$ |
| TPC3-RP1 | $-0.54 \pm 0.01$ | $-40 \pm 10$ | $95 \pm 8$ | $-107 \pm 3$ |

Table B.1: Value of the parameters from Eq. B.5 and the misalignment after the minimization process.

Currently, misalignment and some of the model parameters are highly correlated. This means that some of the values might not be reliable. The best solution would be to improve the current MM misalignment correction on data. This could reduce drastically the impact of the parameter associated to the misalignment in the fit.

## B.4 Validation: $\Delta y$

Data and the prediction from electric potential model show good agreement for the hit-track residuals study. Nevertheless, it is useful to check the performance of the model using other observables. The so called $\Delta y$ quantity is very useful to validate the model. The idea is to use tracks crossing at least two TPCs and propagate their TPC segments to the same Z position. Distortion should bias the Y position of the two propagated segments (see Fig. B.7).

The same control samples from the hit-track residuals study are used: long TPC segments with small deviation along X. Fig B.8 shows $\Delta y$ profiled for each region of the track X position. Similarly to the hit-track residuals study, it seems that the distortions has a clear dependency on the X position and the projected angle in the YZ plane. Besides, it seems that the order of magnitude of this distortion is very similar for the three TPCs.

The result from the model was included using particle guns that mimic the features of the control sample. Then, the electron clouds were drifted using the same technique as in B.3, but drifting towards the anode. The tendency in data and the prediction is similar, but the asymmetric behavior observed in data is not predicted by the simulation. This might be due to misalignment between the detectors or additional odd terms in the electric potential (very difficult to measure with the distortion map fit).

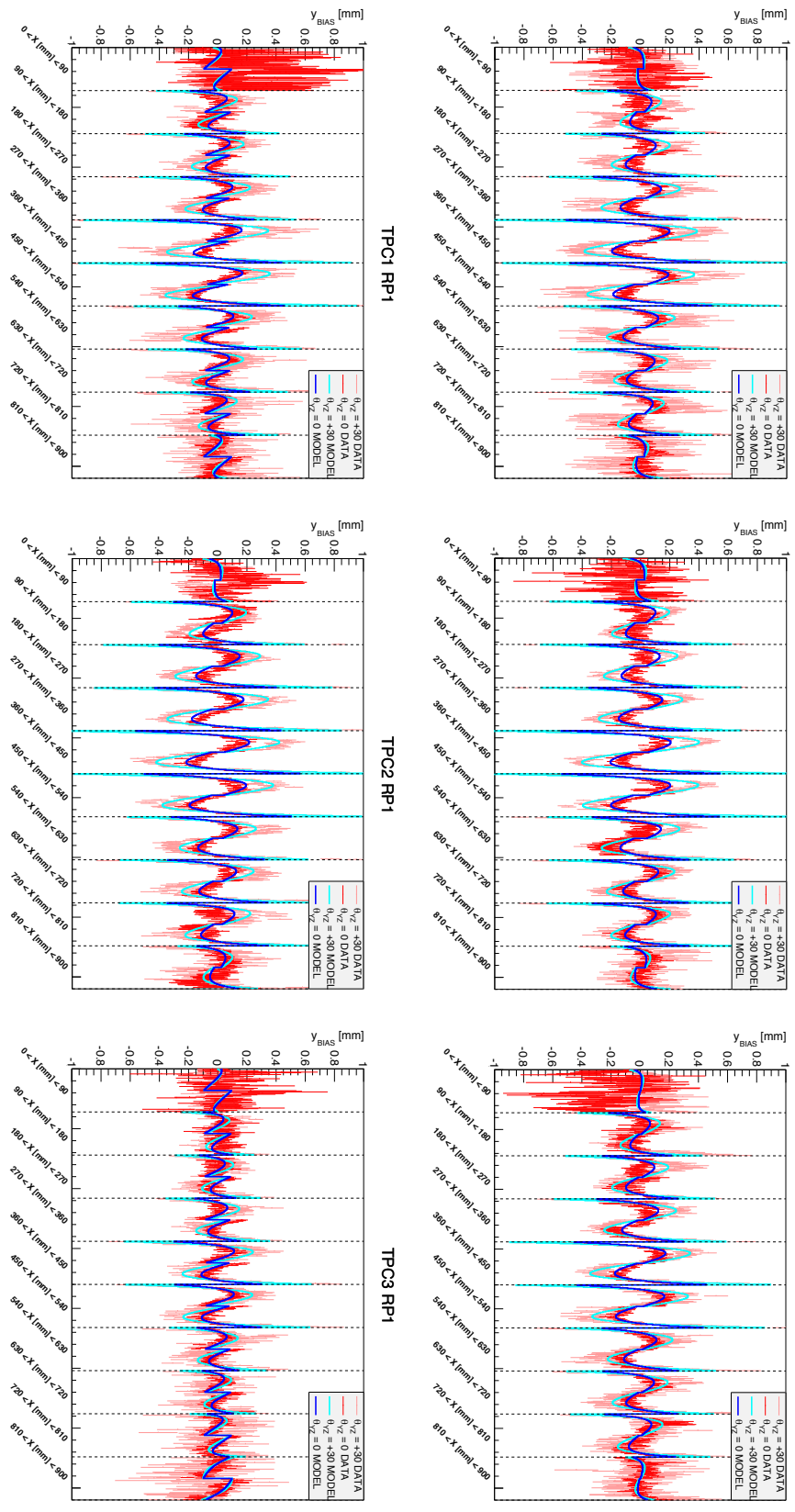


Figure B.6: Distortion map for each TPC and RP for data from the control samples in which magnetic field distortions has been corrected (red points) and the model (blue lines). It shows the profiled $y^i_{bias}$ for each pad column $i$ in each X region. Dashed lines indicate each X region where the first block is the X region closer to the cathode and the last block the one closer to the anode.

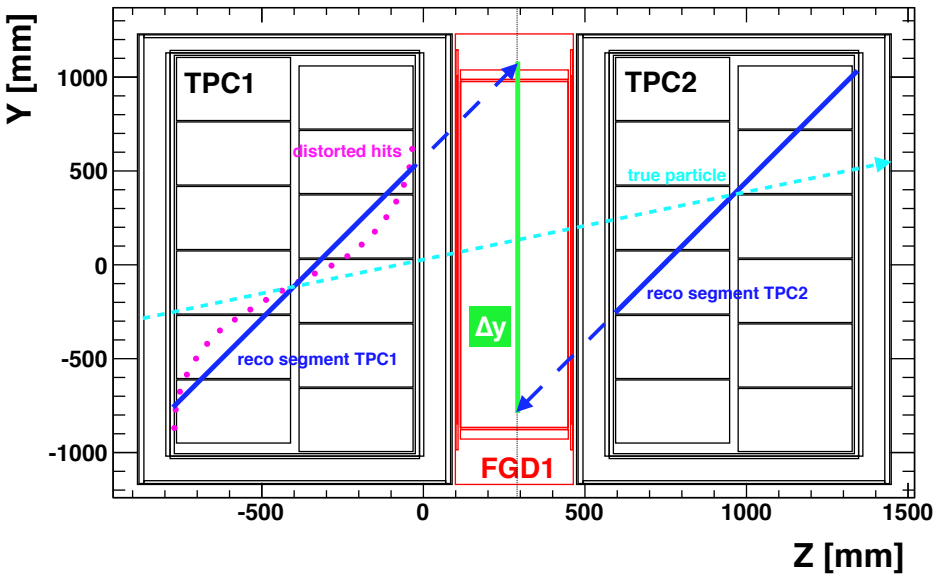


Figure B.7: Schematic view of the $\Delta y$ using segments from TPC1 and TPC2. The effect of the distortion is magnified.

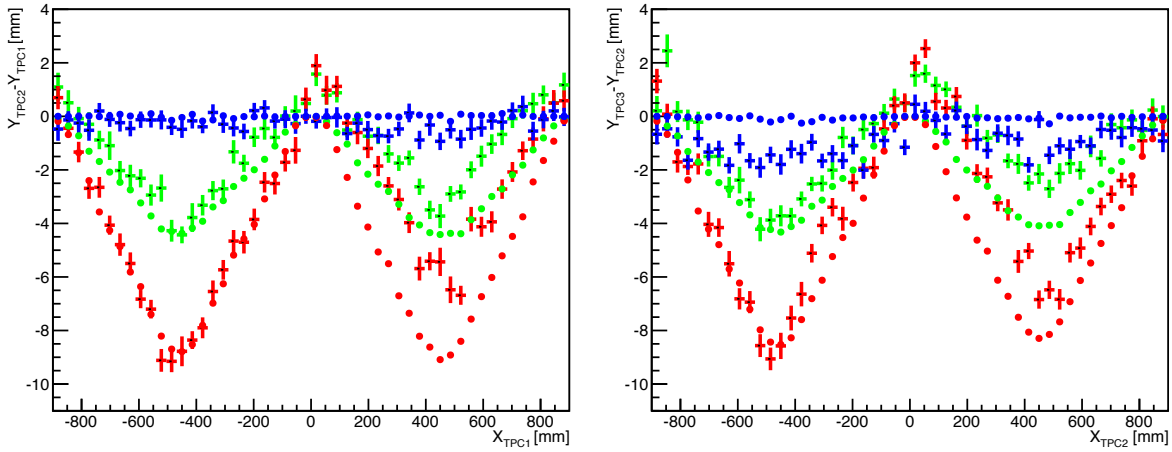


Figure B.8: Profile distribution between $\Delta Y$ and X position for different angles: $30 \pm 2$ (red); $0 \pm 2$ (green) and $-30 \pm 2$ (blue). Crosses indicate the result on data from the control samples in which magnetic field distortions has been corrected. Dots represent the prediction from the simulation.

## B.5 Data Correction

It is possible to correct the electric field distortions on the data using the model for the electric potential and the best fit parameters. The method corrects the position of the electron clouds measured in the pad planes by taking into account the distorted field when Eq. B.1 is used. Then, all the reconstruction is reprocessed. Finally, the hit-track residuals and $\Delta y$ studies can be repeated to check the performance of the correction.

On the one hand, Fig. B.10 shows the distortion maps in different regions of the TPC along the X axis and different angular conditions after the electric field distortions have been corrected. The shapes for the different X volumes and angles becomes flat along the pad plane. On the other hand, Fig B.9 shows $\Delta y$ profiled for each region of the track X position after the correction is performed. In this case, the bias seems to be centered around zero for any value of X.

In general, the correction seems to reduce the impact of the electric field distortion drastically. Nonetheless, it is important to remind that this methodology can be used to extract the even terms of the electric potential, while odd terms remain unknown.

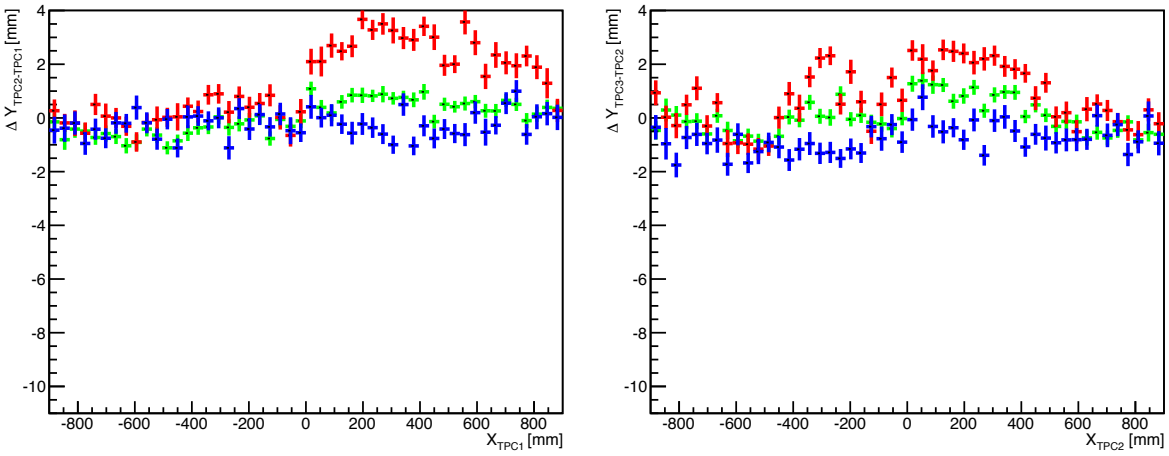


Figure B.9: Profile distribution between $\Delta Y$ and X position for different angles: $30 \pm 2$ (red); $0 \pm 2$ (green) and $-30 \pm 2$ (blue). Crosses indicate the result on data from the control samples in which both magnetic and electric field distortions has been corrected.

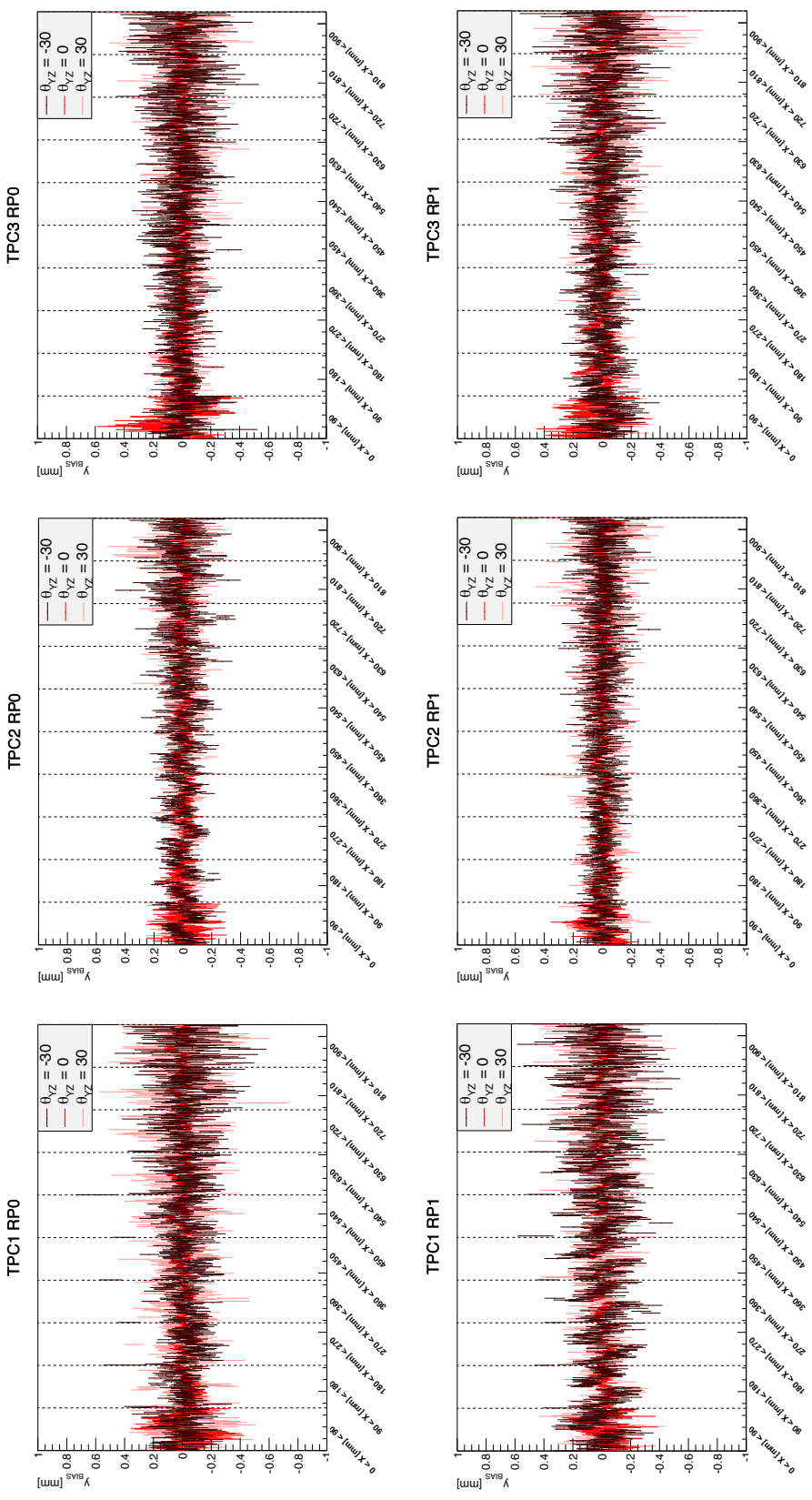


Figure B.10: Distortion map for each TPC and RP for data from the control samples in which both magnetic and electric field distortions has been corrected. It shows the profiled $y^i_{bias}$ for each pad column $i$ in each X region. Dashed lines indicate each X region where the first block is the X region closer to the cathode and the last block the one closer to the anode.

## B.6 Field Distortions and Momentum Resolution-Bias

Electromagnetic field distortions might have an effect on the momentum reconstruction. In this section, the impact of the field corrections on both the momentum resolution and bias is study in detail. The same method used in Sec. 9.3.1 will be followed to perform this analysis.

The same control samples as in previous sections are used to study the momentum resolution in data applying different field corrections. MC is obtained using the analysis files from Run-3c (produced with `NEUT`).

Fig B.11 compares the normalized kinematical distributions of the selected global tracks in data and MC. It is evident that discrepancies are found between data and MC mainly in the momentum and the angular distribution due to the usage of different samples. However, an agreement is also found in some regions of the phase space, allowing to compare data and MC safely (for instance the high momentum region).

Fig B.12 compares the momentum resolution for different configurations of the field corrections distinguishing between different TPCs. For the case of the bias, the results are shown in Fig B.13. Several conclusions can be extracted from these plots:

- Magnetic field corrections reduce mainly the momentum bias in the TPC2-TPC3 case. This is because the distortions are more pronounced in TPC3 (located close to the end of the magnetized volume). For the TPC1-TPC2 case, an improvement is also observed. Concerning the momentum resolution, the impact is less evident.
- Electric field correction affects mainly to the momentum resolution in both TPC1-TPC2 and TPC2-TPC3. It reduces the discrepancy between data and MC.
- Discrepancies between data and MC are not completely fixed with the field corrections. Strange dependencies are observed between momentum resolution-bias and the Y position. This might point to the MM misalignment.

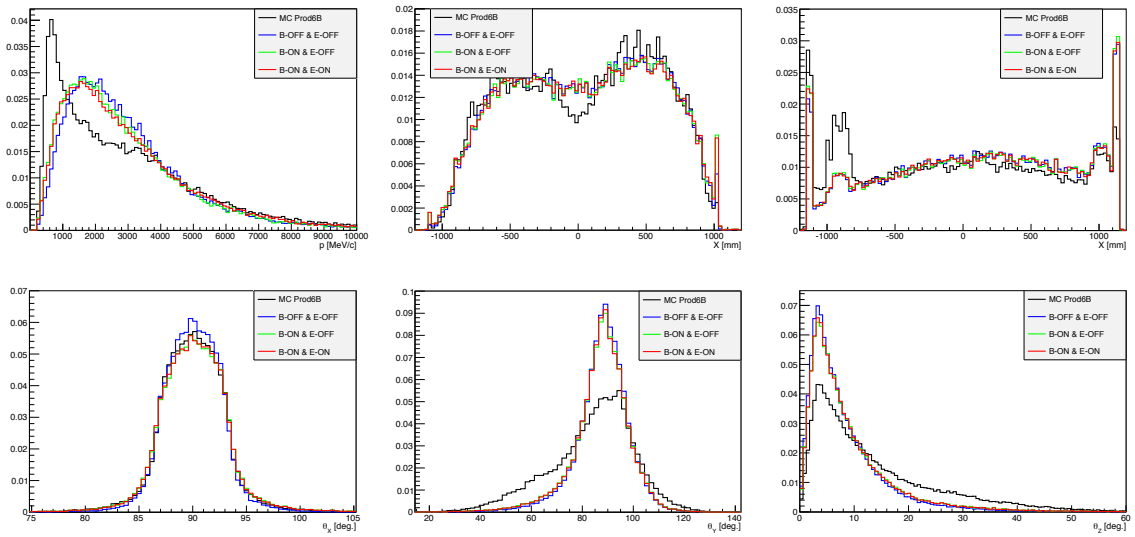


Figure B.11: Normalized distributions for the selected tracks in the selection: Momentum (top left); start position in X (top middle) and Y (top right); director angle X (bottom left), Y (bottom middle) and Z (bottom right). Colors indicate different samples and configuration of the field correction.

## B.7 Conclusions

Field distortions in the TPC of ND280 has been studied in detail. The underlying physics of these distortions is not fully understood yet. Some preliminary studies were showing that defects in the TPC walls could be causing such distortions. Currently, a correction (based on empirical studies) can be applied to the data in order to reduce both magnetic and electric inhomogeneities.

For the E field distortions, an effective electric potential has been implemented to correct them. The performance of the model is satisfactory, showing good agreement with data both for hit-track residuals and $\Delta y$ studies. Nevertheless, this correction is not able to reduce totally observed discrepancies between data and MC in momentum resolution and bias.

Currently, the process to extract the electric potential has several problems:

- Using very complex potential leads to high correlated parameters and slowness in the minimization process.
- MM misalignment is strongly correlated to some of the parameters from the electric potential.
- Odd terms in the electric potential can be absorbed by the curvature in the reconstruction, making them invisible in the s shape distribution.

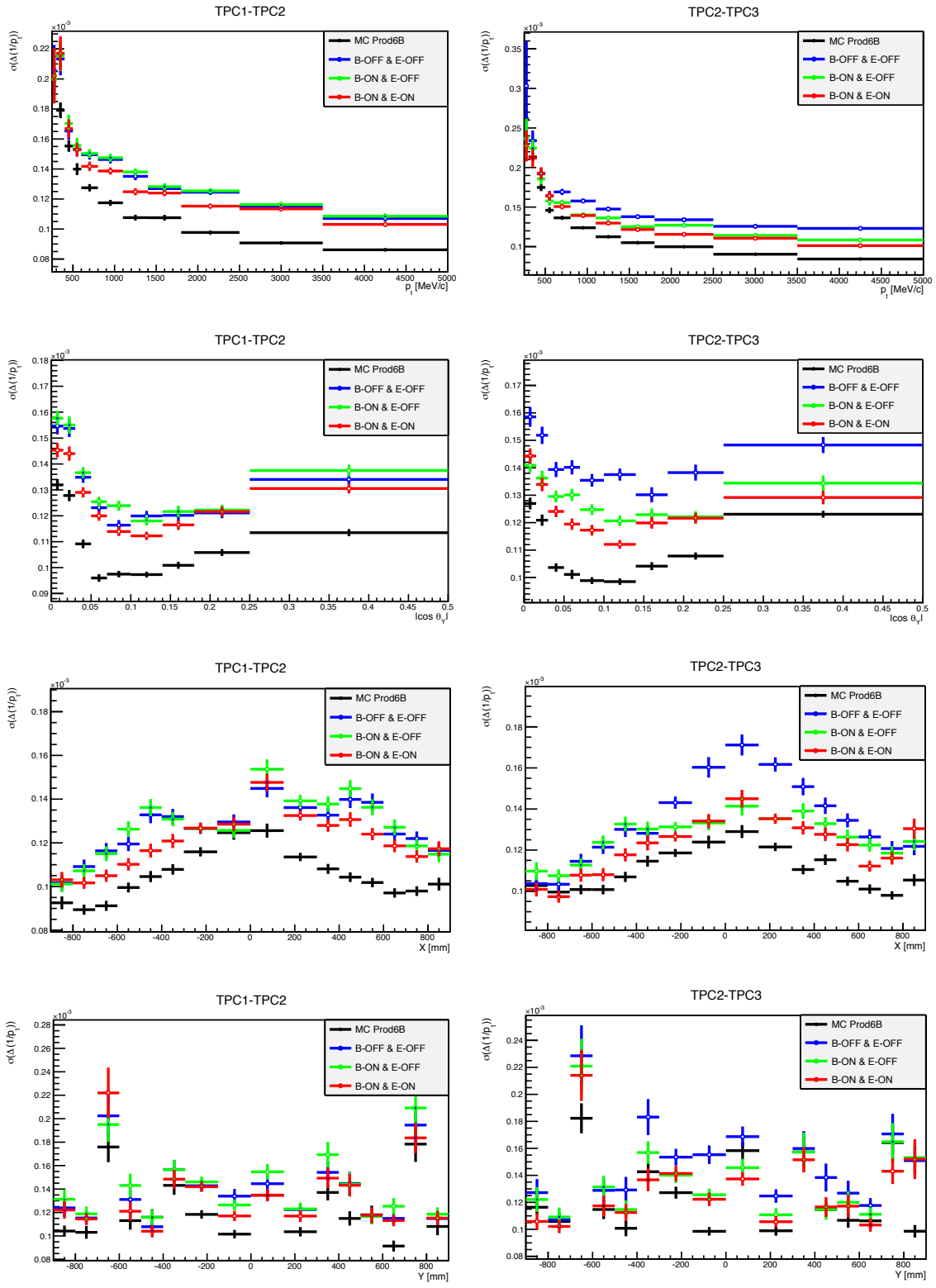


Figure B.12: Momentum resolution as function of the transverse momentum, cosine of the director angle in Y, position X and position Y using TPC1-TPC2 (left) and TPC2-TPC3 (right). Colors indicate the different samples and configuration of the field correction.

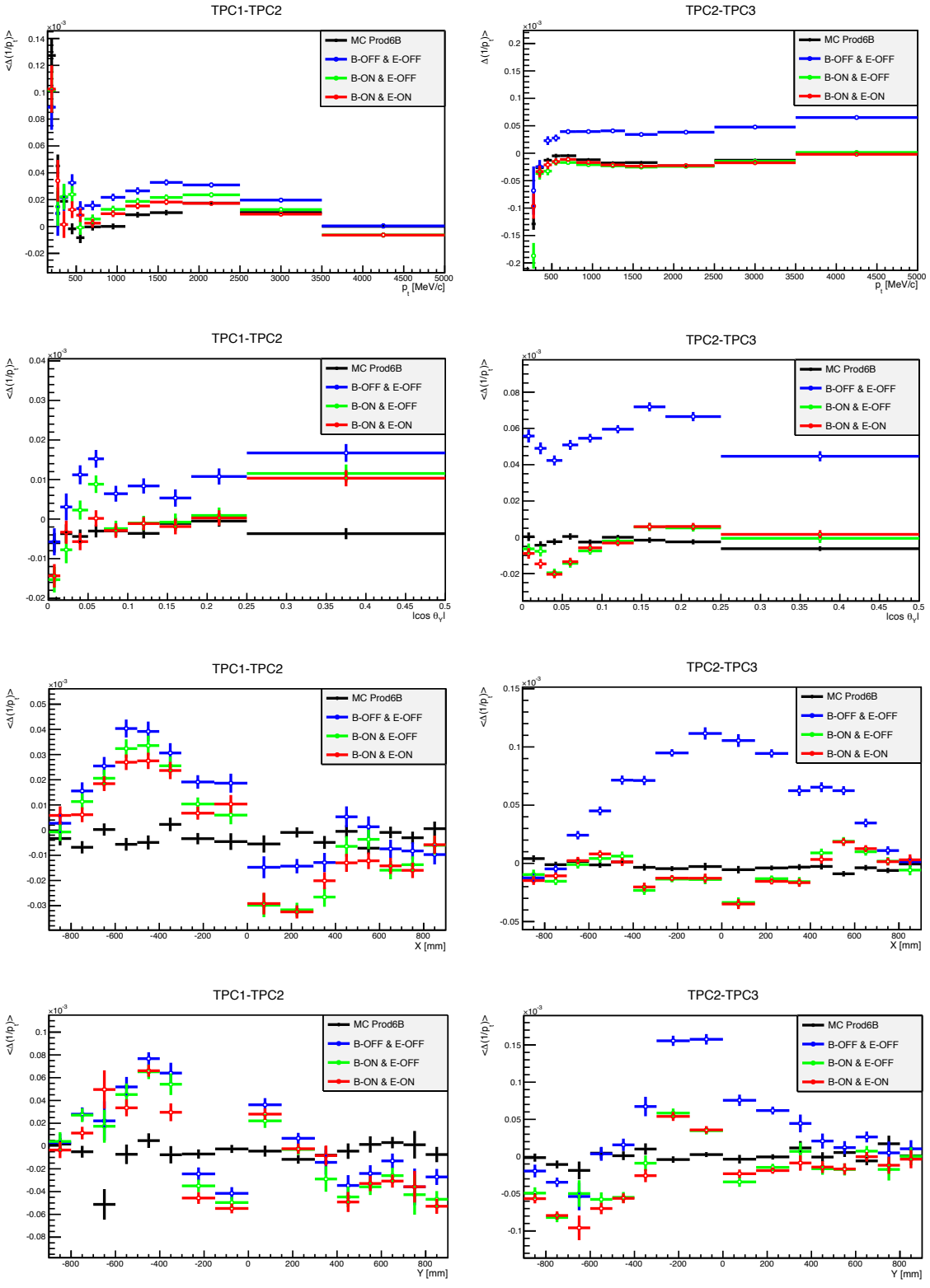


Figure B.13: Momentum bias as function of the transverse momentum, cosine of the director angle in Y, position X and position Y using TPC1-TPC2 (left) and TPC2-TPC3 (right). Colors indicate the different samples and configuration of the field correction.

An interesting idea for future checks is to perform the studies described in this section using data when the magnetic field is OFF. This would reduce the impact of the electric field distortions, but it would allow us to decouple them from the magnetic field distortions. Besides, particle would cross the detector completely straight, reducing the impact of the curvature in the study and making feasible to study odd terms in the electric potential.

# Appendix C

# Time of Flight and Sense Corrections

## C.1 Time of flight Correction

The time of flight between detectors is used to include the sense concept in the reconstructed tracks. At the time this analysis was done, timings from P0D, FGDs, BarrelECal and DsECal were available and calibrated, with ongoing work for PECal and SMRD ones.

Hit patterns in each subdetector affects to the ToF computation. Therefore, the timing distributions will be different depending on the features of the tracks (PID, momentum, number of nodes, etc.). However, it has been found that there are Data/MC discrepancies for these ToF variables even when the features of the tracks are similar in data and MC.

In order to reduce these discrepancies, MC ToF must be biased and smeared so that the shape of its distributions matches data. The Data/MC ToF discrepancies are quantified by fitting each ToF with a sum of two Gaussians. A correction following a Gaussian distribution is then added to the MC ToF:

$$\begin{aligned} ToF_{Corrected} &= ToF + T \\ P(T=t) &= \frac{1}{\sigma_{Corr}\sqrt{2\pi}} \exp \frac{(t - mean_{Corr})^2}{2\sigma^2_{Corr}} \\ mean_{Corr} &= mean_{Data} - mean_{MC} \\ \sigma^2_{Corr} &= \sigma^2_{Data} - \sigma^2_{MC} \end{aligned} \tag{C.1}$$

Firstly, to obtain the correction factors, control samples that mimic the properties of potential $\mu^-$ candidates are constructed. Usually, cosmic $\mu$ are used as control sample, but in this case cosmic $\mu$ (rarely stop in any of the ND280 subdetectors) have very different ToF distributions than beam $\mu$ (often start and stop in any ND280 subdetectors). Therefore, beam $\mu$ will be used as control sample.

A detailed study has been performed to ensure the safety of this correction and it concludes that data/MC ToF discrepancies are due to differences at the reconstruction level between data and MC.

In other words, large ToF discrepancies are not expected only due to theoretical mismodeling of the MC. Data/MC comparison has been made for several variables (length, momentum, direction) when the ToF bias is large between data and MC. For the distributions of those variables the agreement between data and MC is good, which points to a reconstruction problem for the ToF discrepancies.

Four control samples are created. In the following paragraphs, each of them is explained in detail.

***LA-Start***: In this sample highest momentum low angle (more than 18 TPC nodes) track starting in FGD1 is selected. For these tracks, timing information from FGD1-FGD2 and FGD1-BarrelECal can be used.

Looking at the ToF distribution obtained from FGD1-FGD2 (see Fig. C.1), it is clear that a correction is needed. The correction factors for data and MC (distinguishing between magnet and sand $\mu$) are shown in Table C.1.

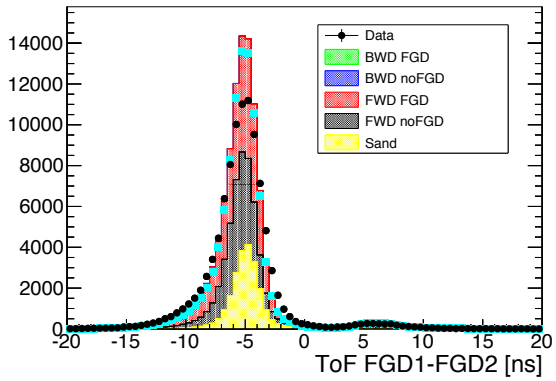


Figure C.1: ToF between FGD1-FGD2 for tracks in *LA-Start* control sample. Colors indicate true sense and whether the true start position is within FGD1. Data/MC discrepancies are non negligible. Light blue markers represent `GENIE` prediction.

| | MC Magnet | MC Sand | Data |
|---|---|---|---|
| $mean_-$ | -5.359+-0.001 | -4.955+-0.003 | -5.199+-0.006 |
| $\sigma^2_-$ | 1.783+-0.003 | 1.198+-0.006 | 2.467+-0.019 |
| $mean_+$ | 6.374+-0.010 | - | 6.139+-0.054 |
| $\sigma^2+$ | 4.669+-0.050 | - | 6.872+-0.232 |

Table C.1: Correction factors obtained after fitting a sum of two Gaussians to the ToF FGD1-FGD2 distributions in the *LA-Start* control sample.

In the case that the timing information is obtained from FGD1-BarrelECal, tracks with one (shower like) or more the one nodes (track like) in BarrelECal are distinguished (see Fig. C.2). The correction factors for data and MC (distinguishing between magnet and sand $\mu$) are shown in Table C.2.

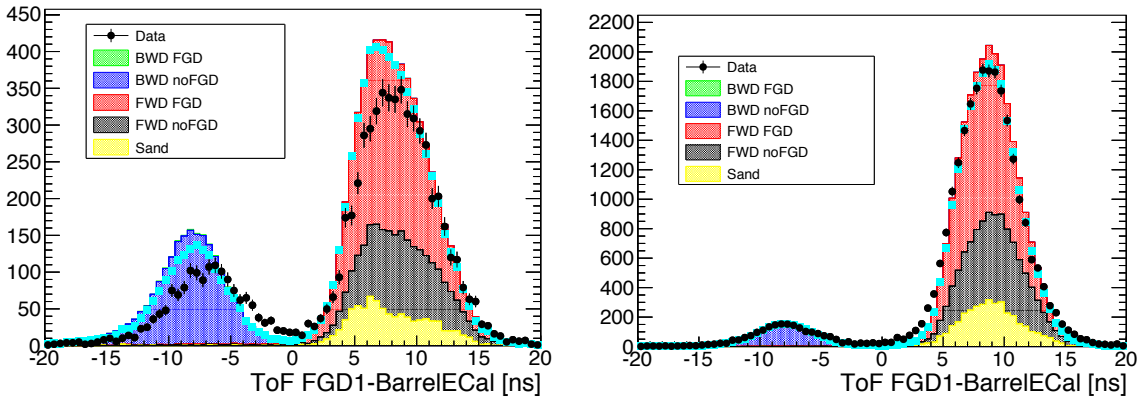


Figure C.2: ToF between FGD1-BarrelECal for tracks in *LA-Start* control sample when the number of nodes in BarrelECal is equal to one (left) and higher than one (right). Colors indicate true sense and whether the true start position is within FGD1. Light blue markers represent `GENIE` prediction.

| | BarrelECal Nodes = 1 | | | BarrelECal Nodes > 1 | | |
|---|---|---|---|---|---|---|
| | MC Magnet | MC Sand | Data | MC Magnet | MC Sand | Data |
| $mean_-$ | -8.264+-0.014 | - | -6.856+-0.085 | -7.992+-0.012 | - | -7.817+-0.068 |
| $\sigma^2_-$ | 7.697+-0.071 | - | 9.762+-0.483 | 6.006+-0.051 | - | 8.482+-0.382 |
| $mean_+$ | 8.243+-0.009 | 8.135+-0.041 | 8.483+-0.043 | 8.858+-0.004 | 8.921+-0.014 | 8.692+-0.017 |
| $\sigma^2_+$ | 8.261+-0.038 | 8.524+-0.144 | 9.404+-0.207 | 5.400+-0.012 | 5.795+-0.051 | 6.725+-0.073 |

Table C.2: Correction factors obtained after fitting a sum of two Gaussians to the ToF FGD1-BarrelECal distributions in the *LA-Start* control sample.

***LA-End***: In this sample highest momentum low angle (more than 18 TPC nodes) track ending in FGD1 is selected. For these tracks, timing information from FGD1-P0D and FGD1-BarrelECal can be used.

In the case that the timing information is obtained from FGD1-P0D, tracks are split depending on the number of nodes reconstructed in P0D, one (shower like) or more the one (track like) (see Fig. C.3). It is clear that the timing does not perform well when the number of nodes is equal to one. Therefore, no correction is applied in that case. The correction factors for data and MC (distinguishing between magnet and sand $\mu$) are shown in Table C.3.

| | MC Magnet | MC Sand | Data |
|---|---|---|---|
| $mean_-$ | -6.744+-0.003 | -7.714+-0.003 | -7.842+-0.008 |
| $\sigma^2-$ | 3.405+-0.008 | 1.858+-0.007 | 3.625+-0.031 |
| $mean_+$ | 6.575+-0.014 | - | 5.575+-0.088 |
| $\sigma^2+$ | 2.440+-0.041 | - | 4.600+-0.276 |

Table C.3: Correction factors obtained after fitting a sum of two Gaussians to the ToF FGD1-P0D distributions in the *LA-End* control sample.

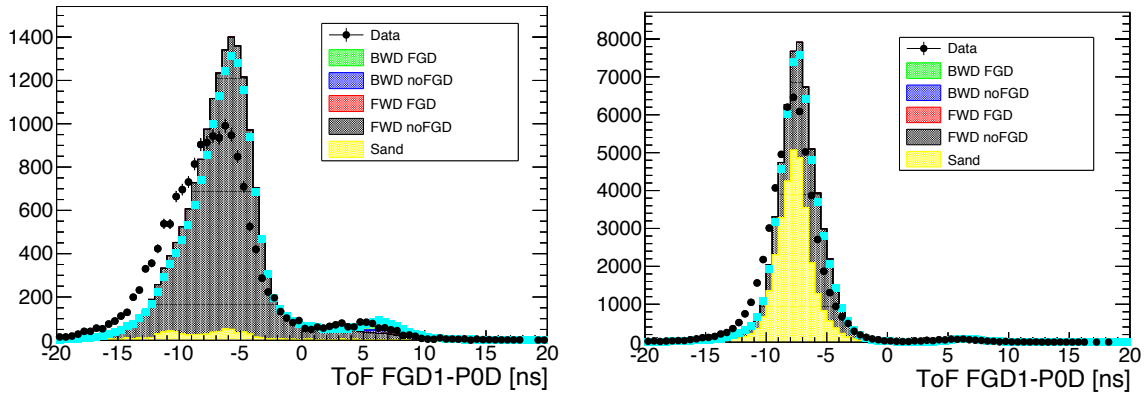


Figure C.3: ToF between FGD1-P0D for tracks in *LA-End* control sample when the number of nodes in P0D is equal to one (left) and higher than one (right). Colors indicate true sense and whether the true start position is within FGD1. It is clear that when the nodes are equal to one the ToF can not distinguish properly between forward and backward going tracks. Light blue markers represent `GENIE` prediction.

In the case that the timing information is obtained from FGD1-BarrelECal, tracks are split depending on the number of nodes reconstructed in BarrelECal: one (shower like) or more the one (track like) (see Fig. C.4). The correction factors for data and MC (distinguishing between magnet and sand $\mu$) are shown in Table C.4.

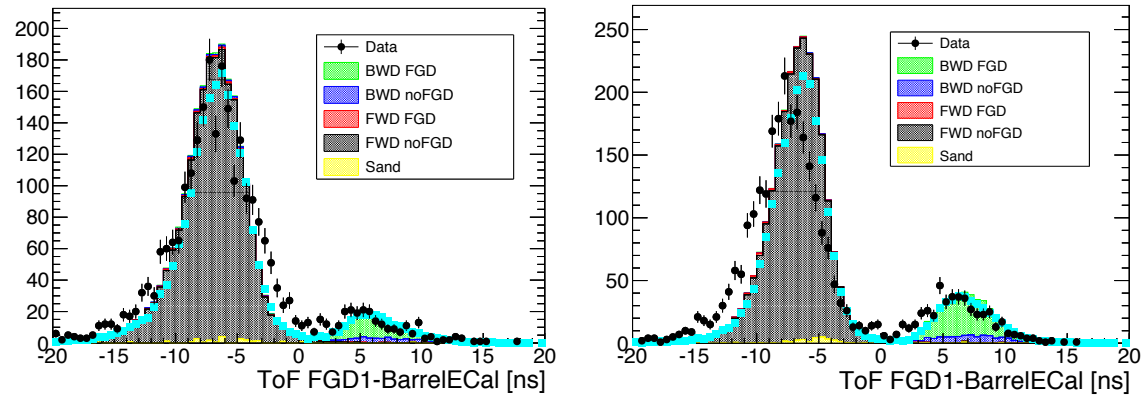


Figure C.4: ToF between FGD1-BarrelECal for tracks in *LA-End* control sample when the number of nodes in BarrelECal is equal to one (left) and higher than one (right). Colors indicate true sense and whether the true start position is within FGD1. Light blue markers represent `GENIE` prediction.

***HA-Start***: In this sample highest momentum high angle (less than 18 TPC nodes) track starting in FGD1 and ending in SMRD or BarrelECal FV (see Appendix A) is selected. For these tracks, timing information from FGD1-BarrelECal can be used. Tracks with one (shower like) or more the one nodes (track like) are split in BarrelECal (see Fig. C.5). The correction factors for data and MC

| | BarrelECal Nodes = 1 | | | BarrelECal Nodes > 1 | | |
|---|---|---|---|---|---|---|
| | MC Magnet | MC Sand | Data | MC Magnet | MC Sand | Data |
| $mean_-$ | -6.943+-0.012 | - | -6.845+-0.072 | -6.760+-0.010 | - | -7.764+-0.057 |
| $\sigma^2-$ | 5.693+-0.050 | - | 10.135+-0.455 | 4.126+-0.033 | - | 6.916+-0.271 |
| $mean_+$ | 6.170+-0.039 | - | 5.509+-0.242 | 6.886+-0.025 | - | 5.999+-0.133 |
| $\sigma^2+$ | 6.711+-0.194 | - | 7.585+-1.371 | 5.189+-0.092 | - | 7.406+-0.649 |

Table C.4: Correction factors obtained after fitting a sum of two Gaussian to the ToF FGD1-BarrelECal distributions in the *LA-End* control sample.

(distinguishing between magnet and sand $\mu$) are shown in Table C.5.

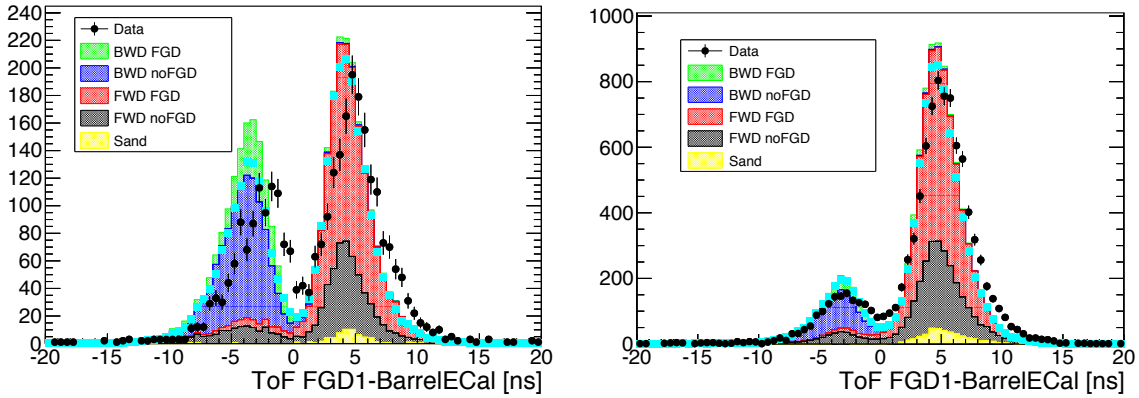


Figure C.5: ToF between FGD1-BarrelECal for tracks in *HA-Start* control sample when the number of nodes in BarrelECal is equal to one (left) and higher than one (right). Colors indicate true sense and whether the true start position is within FGD1. Light blue markers represent `GENIE` prediction.

| | BarrelECal Nodes = 1 | | | BarrelECal Nodes > 1 | | |
|---|---|---|---|---|---|---|
| | MC Magnet | MC Sand | Data | MC Magnet | MC Sand | Data |
| $mean_-$ | -3.938+-0.013 | - | -2.767+-0.092 | -3.336+-0.011 | - | -3.077+-0.075 |
| $\sigma^2-$ | 3.812+-0.050 | - | 4.961+-0.397 | 3.577+-0.044 | - | 4.617+-0.290 |
| $mean_+$ | 4.425+-0.010 | 4.479+-0.058 | 5.125+-0.066 | 4.892+-0.005 | 5.262+-0.038 | 5.311+-0.027 |
| $\sigma^2+$ | 2.934+-0.035 | 1.457+-0.118 | 4.832+-0.305 | 3.091+-0.017 | 3.225+-0.111 | 4.553+-0.118 |

Table C.5: Correction factors obtained after fitting a sum of two Gaussians to the ToF FGD1-BarrelECal distributions in the *HA-Start* control sample.

***HA-End***: In this sample highest momentum high angle (less than 18 TPC nodes) track starting in SMRD or BarrelECal FV (see Appendix A) and ending in FGD1 is selected. For these tracks, timing information from FGD1-BarrelECal can be used. Again, tracks are split depending on the number of nodes in BarrelECal: one (shower like) or more the one (track like) (see Fig. C.6). The correction factors for data and MC (distinguishing between magnet and sand $\mu$) are shown in Table C.6.

This correction factors are used to bias and smear the MC. Clear improvement can be observed in the timing distributions in the following section.

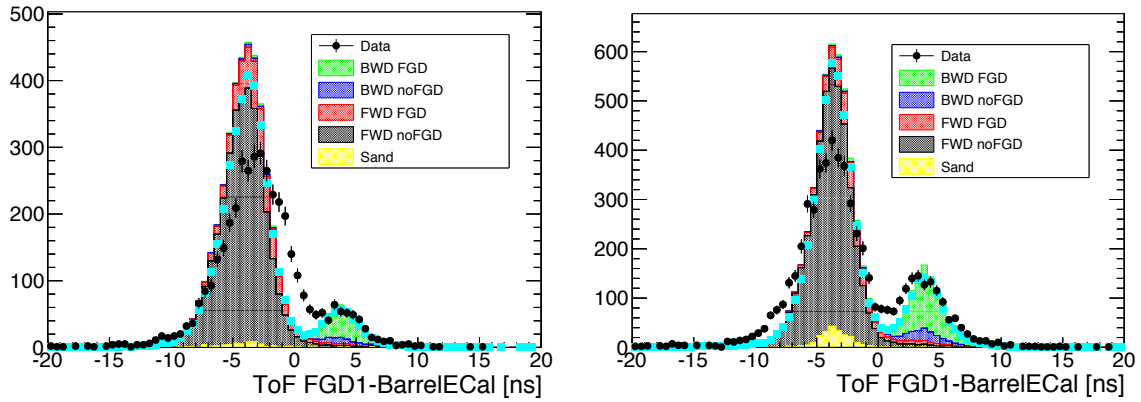


Figure C.6: ToF between FGD1-BarrelECal for tracks in *HA-End* control sample when the number of nodes in BarrelECal is equal to one (left) and higher than one (right). Colors indicate true sense and whether the true start position is within FGD1. Light blue markers represent `GENIE` prediction.

| | BarrelECal Nodes = 1 | | | BarrelECal Nodes > 1 | | |
|---|---|---|---|---|---|---|
| | MC Magnet | MC Sand | Data | MC Magnet | MC Sand | Data |
| $mean_-$ | -4.102+-0.007 | -4.386+-0.113 | -3.220+-0.051 | -3.757+-0.006 | -4.016+-0.041 | |
| $\sigma^2-$ | 3.262+-0.022 | 2.728+-0.440 | 6.777+-0.259 | 2.796+-0.018 | 1.381+-0.062 | 5.321+-0.200 |
| $mean_+$ | 3.804+-0.020 | - | 3.271+-0.124 | 3.845+-0.012 | - | 3.788+-0.076 |
| $\sigma^2+$ | 2.664+-0.065 | - | 4.735+-0.375 | 2.472+-0.037 | - | 3.706+-0.288 |

Table C.6: Correction factors obtained after fitting a sum of two Gaussians to the ToF FGD1-BarrelECal distributions in the *HA-End* control sample.

## C.2 Sense Correction

This correction allows to distinguish between forward (meaning $z_{start} < z_{end}$) and backward (meaning $z_{start} > z_{end}$) going tracks. The idea is to correct the sense of the reconstructed track when timing information provided by the time of flight variable (ToF) fulfill certain criteria. Therefore, when this correction is applied there will be a flip between the following reconstructed variables:

$$\text{PositionStart} \leftrightarrow \text{PositionEnd}$$

$$\text{DirectionStart} \leftrightarrow \text{-DirectionEnd}$$

Furthermore, at global reconstruction the momentum of the track is computed under the assumption of forward (Momentum) and backward (MomentumFlip) sense of the track. In the case of the charge, it is always computed under the forward going assumption. Therefore, long TPC tracks, for which the reconstructed momentum and charge are reliable, the sense correction is also applied for these variables in the following way:

Momentum $\leftrightarrow$ MomentumFlip

Charge $\leftrightarrow$ -Charge

At the reconstruction level, in the previous analysis, the sense concept was only introduced for tracks with ToF computed with FGD1-FGD2 detectors. In this analysis, the concept will be extended for tracks with timing information obtained from FGD1-P0D, FGD1-BarrelECal. In the following paragraphs, the correction criteria is described in detail.

In a first step all tracks are forced to be forward going. In order to apply the sense correction in a consistent way, only tracks with corrected ToF will be taken into account. Furthermore, in previous section it was shown that the timing information is different depending on the properties of the tracks. Therefore, the sense correction will be different for each of the groups (see Sec. C.1).

***LA-Start***: For these tracks, the flip method is applied using two different timing information: FGD1-FGD2 and FGD1-BarrelECal. Fig. C.7 and Fig. C.8 show the timing information and the red arrow indicates which tracks are flipped.

***LA-End***: For these tracks, the flip method is applied using two different timing information: FGD1-P0D and FGD1-BarrelECal. Fig. C.9 and Fig. C.10 show the timing information and the red arrow indicates which tracks are flipped.

***HA-Start***: For these tracks, the flip method is applied using only one timing information: FGD1-BarrelECal. Fig. C.11 shows the timing information and the red arrow indicates which tracks are flipped.

***HA-End***: For these tracks, the flip method is applied using only one timing information: FGD1-BarrelECal. Fig. C.12 shows the timing information and the red arrow indicates which tracks are flipped.

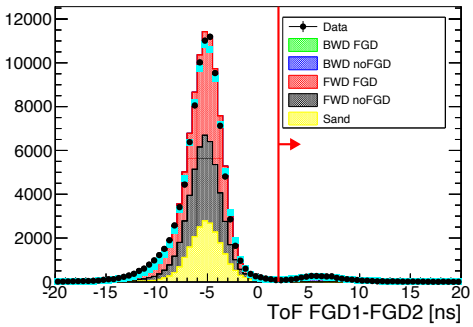


Figure C.7: ToF between FGD1-FGD2 for tracks in *LA-Start* sample. Colors indicate true sense and whether the true start position is within FGD1. Red arrow indicates the flipped region. Light blue markers represent `GENIE` prediction.

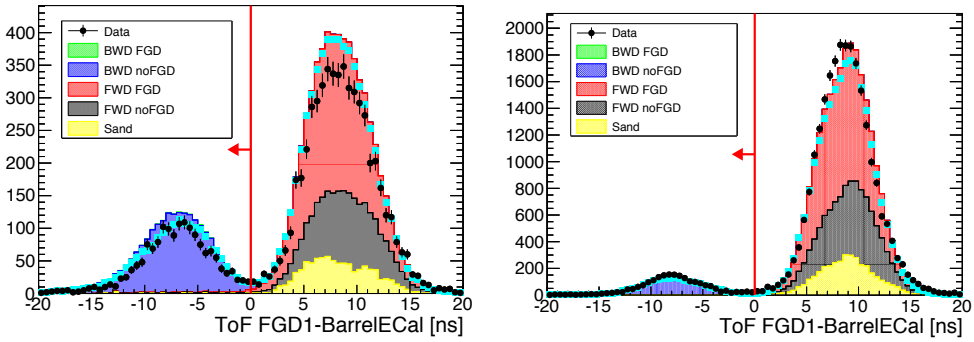


Figure C.8: ToF between FGD1-BarrelECal for tracks in *LA-Start* sample when the number of nodes in BarrelECal is equal to one (left) and higher than one (right). Colors indicate true sense and whether the true start position is within FGD1. Red line indicates the correction value. Light blue markers represent `GENIE` prediction.

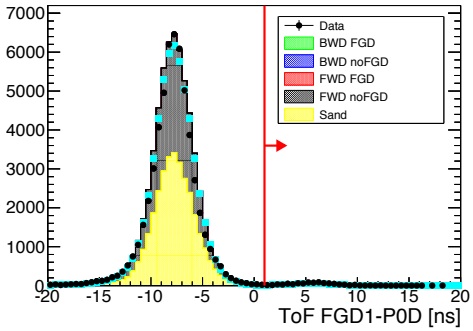


Figure C.9: ToF between FGD1-POD for tracks in *LA-End* sample when the number of nodes in P0D is higher than one. Colors indicate true sense and whether the true start position is within FGD1. Red arrow indicates the flipped region. Light blue markers represent `GENIE` prediction.

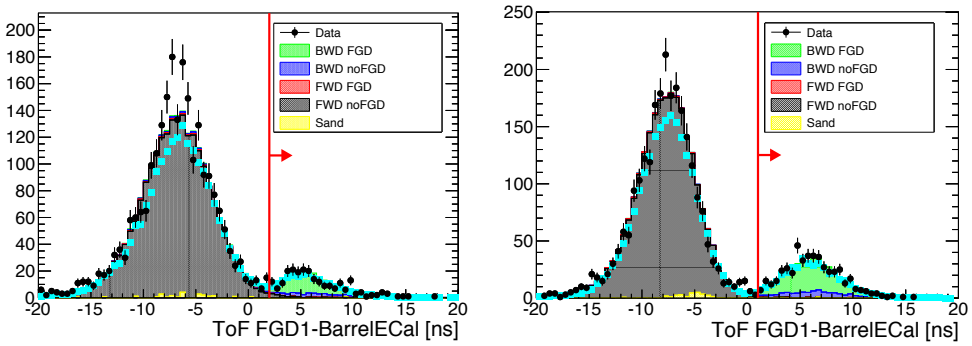


Figure C.10: ToF between FGD1-BarrelECal for tracks in *LA-End* sample when the number of nodes in BarrelECal is equal to one (left) and higher than one (right). Colors indicate true sense and whether the true start position is within FGD1. Red arrow indicates the flipped region. Light blue markers represent `GENIE` prediction.

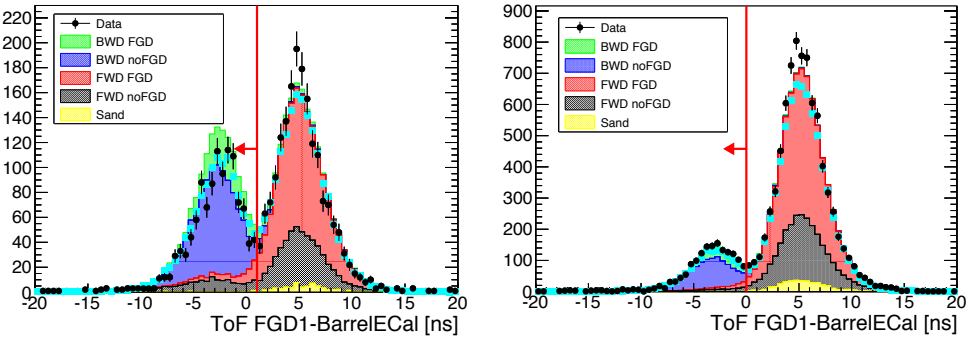


Figure C.11: ToF between FGD1-BarrelECal for tracks in *HA-Start* sample when the number of nodes in BarrelECal is equal to one (left) and higher than one (right). Colors indicate true sense and whether the true start position is within FGD1. Red arrow indicates the flipped region. Light blue markers represent `GENIE` prediction.

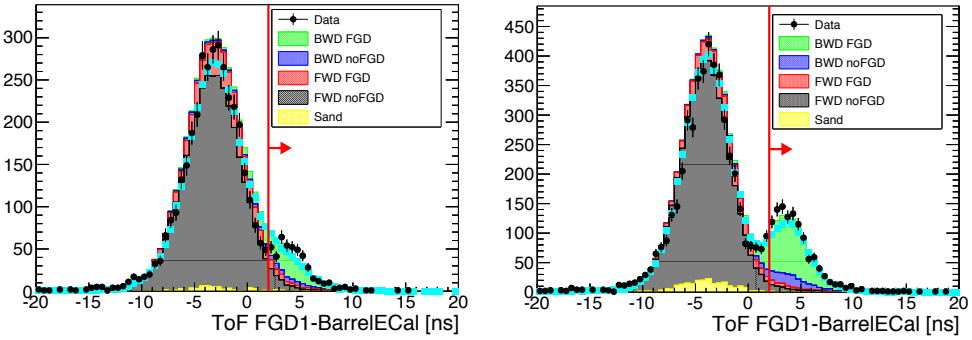


Figure C.12: ToF between FGD1-BarrelECal for tracks in *HA-End* sample when the number of nodes in BarrelECal is equal to one (left) and higher than one (right). Colors indicate true sense and whether the true start position is within FGD1. Red arrow indicates the flipped region. Light blue markers represent `GENIE` prediction.

# Appendix D

# Vertex Migration due to Hadrons

In this analysis, the vertex is defined by the start position of the $\mu^-$ candidate. This information is mainly extracted from TPC-FGD matching, which uses an incremental matching procedure based on Kalman Filter from `RecPack` (see Sec. 6.3.7). The basic workflow for this matching is the following:

- The seeds are the TPC reconstructed segments.
- Only use FGD hits that are in the same time bin as the TPC objects and charge>5 pe.
- Extrapolate TPC track to the closest layer of hits.
- $\chi^2$ minimization for all the hits in the layer.
- If $\chi^2 < 15$, then hit is matched and seed is recomputed (repeated for all hits in layer).
- Repeat previous steps for the next layer. The extrapolation will stop if we skip more than one layer without hits (not when $d(y,x)/dz < 0.07$).
- After extrapolation stops, final refit, which smooths the reconstructed track.

Due to the current resolution of the FGD, directly related with the size of the scintillator bars, this matching algorithm might face some problems:

- For events in which the outgoing lepton and an hadron are produced back to back (parallel to each other), it is difficult to define the initial position for each of them (see Fig. D.1).
- When the particle multiplicity is high, hits produced by particles (which are not the lepton) might be matched to the reconstructed FGD segment associated to the $\mu^-$ candidate. Low momentum hadrons are the main contributors (see Fig. D.1).

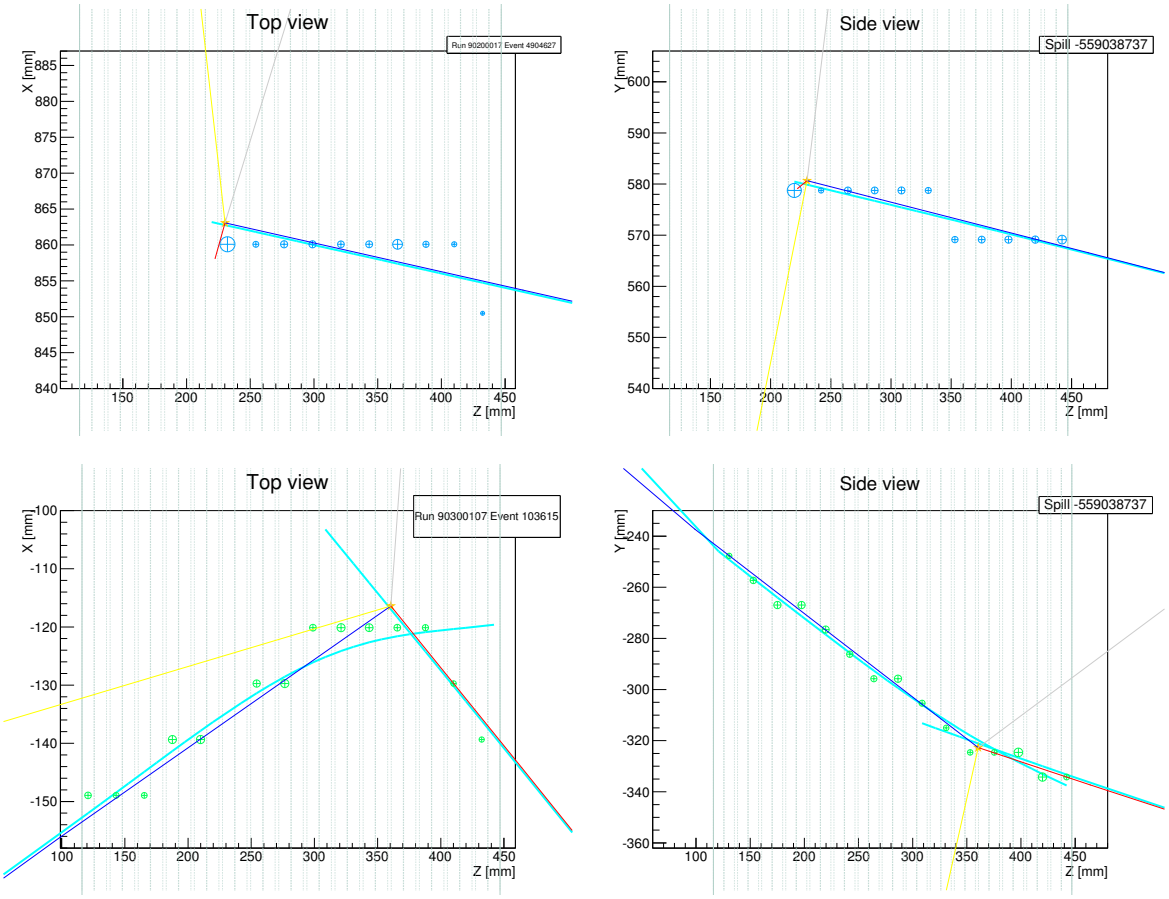


Figure D.1: Display of two events for which the vertex is migrated in FWD (top) and BWD (bottom) samples from `NEUT`. Lines represents the true trajectory for different particles ($\mu$=blue, proton=red, photon=yellow, gray=neutron). Thick light blue lines represent the reconstructed tracks. Circles represent the layers with a hit (size is proportional to the deposited charge). Dashed gray lines indicate the borders of the FGD1 layers.

The reconstructed vertex will be affected by both hadron production and kinematics at the interaction point. This migration might have a non negligible effect in three different aspects of analysis using FGD as target:

- Reconstructed momentum uses the momentum lost within the FGD, which is based on the length of the FGD segment. The migration of the vertex will change the length of the segment, producing a bias in the momentum reconstruction.
- Reconstructed angle mainly for low energy particles.
- Interactions happening out of fiducial volume can be reconstructed within the fiducial volume due to the migration of the vertex.
- Interactions happening within fiducial volume can be reconstructed out of fiducial volume due to the migration of the vertex.

The main problem is that our current MC generators do not predict accurately the kinematics of the outgoing hadrons, which depends on both cross section and FSI models. This might lead to differences between data and MC in the amount of events that suffer from these migrations. Besides, the length of this migration might also differ between data and MC.

It is important to understand the impact of this issue on the selection. Fig. D.2 shows how the vertex migrates in each sample. It is clear that the behavior is completely different depending on the sample. Indeed, in FWD and HAFWD samples, the effect is less relevant than in the BWD and HABWD case. Furthermore, the length of the migration seems to be higher in the BWD and HABWD selections. This is due to the fact that the incremental matching algorithm was optimized for forward going tracks.

Another interesting fact is the nature of the interaction associated to the vertex migration in each sample. For BWD and HABWD selections, the dominant reaction is CCQE (see Fig. D.2), so back to back topologies (between $\mu^-$ and proton) are the dominant cause of the migration. In the FWD and HAFWD cases, the high multiplicity is playing an important role (dominated by CCDIS and CCRES interactions).

It is important to notice that all the vertex migration observed in Fig. D.2 are not produced by hadrons. Indeed, part of the migrations appears because the sense of the $\mu^-$ candidate is not properly reconstructed. Table D.1 summarizes the true impact of the migrations due to secondary particles.

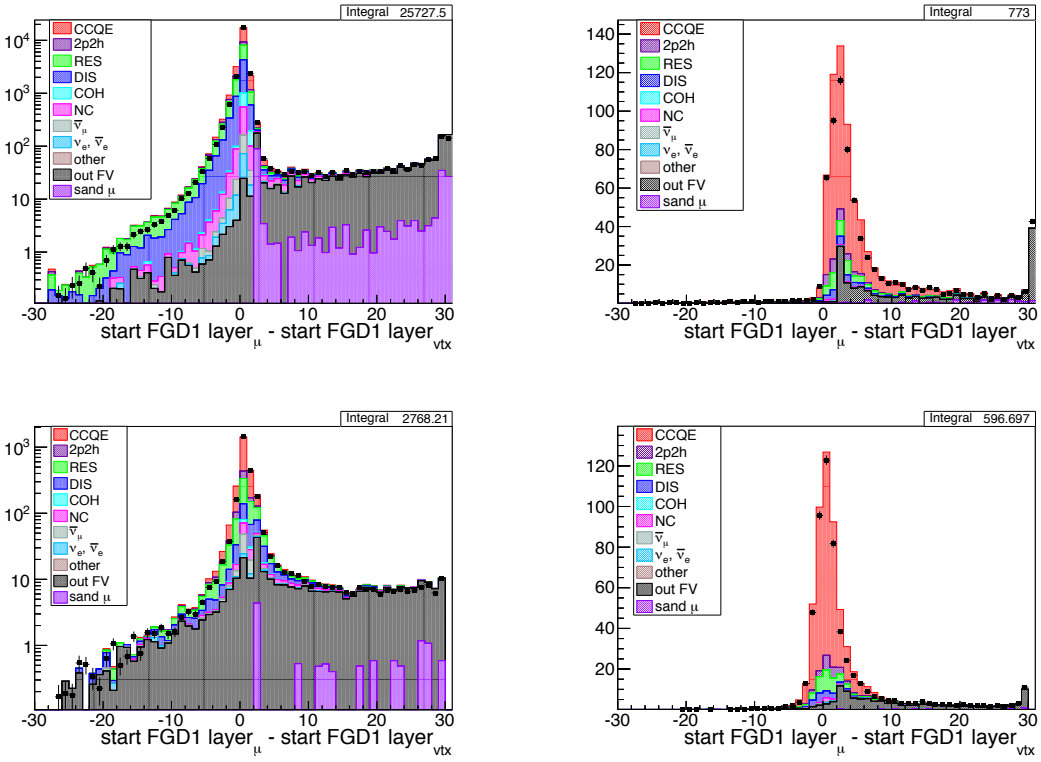


Figure D.2: Difference between the FGD1 layer associated to the reconstructed start position of the $\mu^-$ candidate and the true start position of the vertex for the different samples: FWD (top left), BWD (top right), HAFWD (bottom left), HABWD (bottom right). Colors indicate the true reaction type. Black dots represents the distribution using `GENIE`. In FWD and HAFWD (BWD and HABWD), the vertex migration appears when the difference is negative (positive).

The first conclusion that can be extracted is that percentage of vertex migration produced by hadrons in the selection are of the same order for `NEUT` and `GENIE`.

| | Number of events (OOFV fraction %) | | | |
|---|---|---|---|---|
| | FWD | BWD | HAFWD | HABWD |
| | 26655.7 (4.4) | 798.7 (21.6) | 2857.2 (11.3) | 591.5 (16.8) |
| | 25215.7 (4.4) | 716.2 (22.5) | 2681.0 (10.9) | 542.2 (17.2) |
| + Vertex migration | 5152.5 (7.3) | 628.9 (17.2) | 462.6 (22.0) | 276.4 (30.2) |
| | 3578.2 (10.4) | 552.1 (17.9) | 308.1 (28.1) | 243.0 (32.8) |
| + Produced by hadron | 4927.6 (4.6) | 528.9 (6.6) | 410.9 (17.4) | 189.3 (15.9) |
| | 3349.1 (6.1) | 455.1 (5.8) | 255.9 (20.8) | 157.9 (14.6) |

Table D.1: Number of selected events that fulfill the criteria in each of the samples. The value in parenthesis represent the percentage of events in which the interaction is out of FGD1 FV. First row shows the result for `NEUT` and second for `GENIE`.

An interesting study is to identify which kind of hadrons are producing these migrations. That information is obtained looking for the true contributors that have produced FGD hits, which have been matched to the $\mu^-$ candidate FGD segment. This study has been performed for a subsample of selected events in the BWD sample using `GENIE`. Fig D.3 shows that the main contributor are protons going in the opposite direction of the $\mu^-$ candidate.

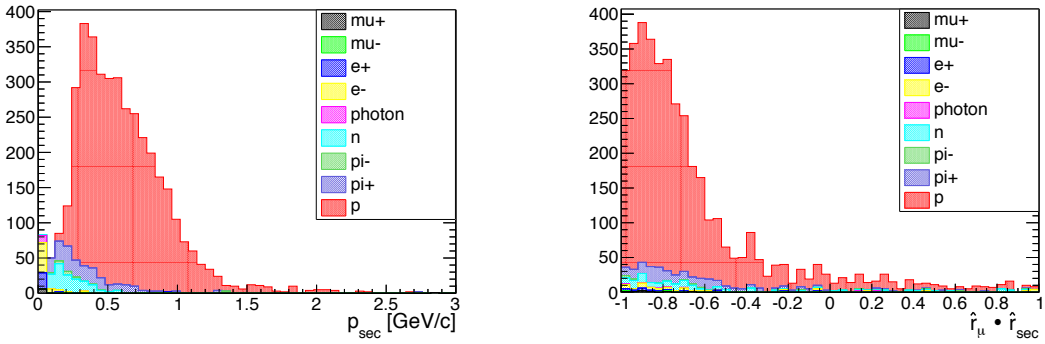


Figure D.3: Momentum of the true contributor producing FGD hits matched to the $\mu^-$ candidate FGD segment (left). Scalar product between the direction of such contributor and the $\mu^-$ candidate is also shown (right). Colors indicate the particle type.

However, preliminary studies in the FWD sample have shown that the true contributors are mainly backward going $\pi^+$ with momentum $\sim$200 MeV/c or protons with momentum greater than 200 MeV/c.

## D.1 From OOFV to FV

From Table D.1, it is possible to infer the impact of the vertex migration from the OOFV to FV due to hadrons. For the low angle selections, the migration is mainly coming from events happening in the dead material between the FGD, TPC and ECAL. From the total number of predicted OOFV events, around 20% are affected by this migration in FWD and BWD samples. For high angles selection, it also includes events happening in the rejected layers at the borders of the FGD in the X and Y directions. From the total number of predicted OOFV events, 22% (37%) are affected by this migration in HAFWD (HABWD).

Those percentage refers to simulation predictions. However, for data the percentage might be completely different. Therefore, a normalization systematic should be associated to this kind of events. Currently, no uncertainty is assumed.

## D.2 From FV to OOFV

When the interaction has happened within the FGD1 FV, the vertex can be migrated to the rejected layers of the FGD1. This can mainly happens when the interaction is happening near the boundaries of the FV.

The amount of events suffering from this process can be estimated. The idea is to rerun the event selection without including the FV cut (see Sec. 8.5). Then, it is possible to count the number of $\mu^-$ candidates that has been reconstructed in the rejected layers but with its true vertex in the FGD1 FV. This study has been done for the FWD sample for `NEUT` (`GENIE`), showing that 1.9% (2.3%) of the $\nu_\mu$ CC interactions happening in the FGD1 FV were migrated to the rejected layers of the FV cut. The result is very similar for both generators.

The rate predicted by the MC might be different in data. This process is directly related with the simulation of hadrons. The problem is that it is very difficult to evaluate the differences between data and MC. To propagate this uncertainty in a very conservative way, a global normalization systematic can be associated to the selection, so the rate of reconstructed events near the edges of the fiducial volume fluctuates. Assuming that the difference between data and MC is of the order of 50% and applying such normalization uncertainty to the events reconstructed in the three closest layers of the

fiducial volume edges, that would lead to a 0.1% uncertainty in the total rate of reconstructed events. Currently, no uncertainty is associated to this effect.

## D.3 Momentum Bias

From Table D.1, it is also possible to infer how many events are affected by the momentum bias due to the vertex migration. Besides, it is interesting to observe the bias in the momentum distribution for each sample (see Fig. D.4). BWD and HABWD selections show a clear bias, while in FWD and HAFWD selections the effect is negligible.

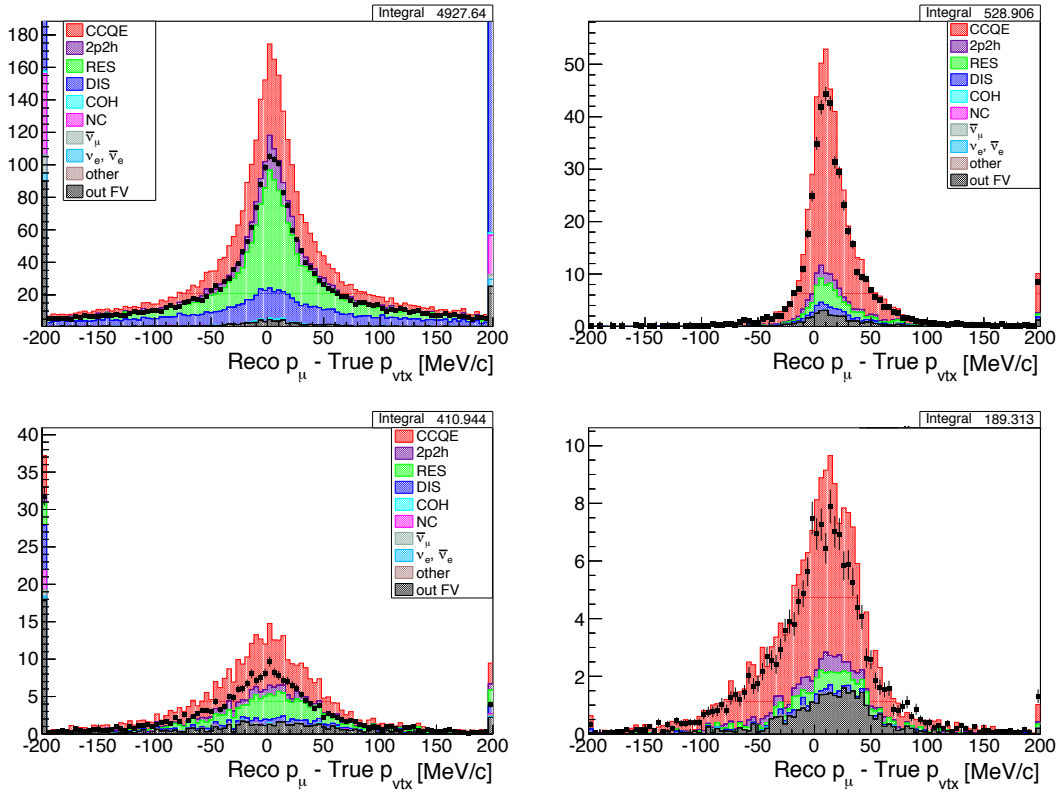


Figure D.4: Difference between the reconstructed and true momentum of the $\mu^-$ candidate for events affected by vertex migration produced by hadrons (last row in Table D.1): FWD (top left), BWD (top right), HAFWD (bottom left), HABWD (bottom right). Colors indicate the true reaction type. Black dots represents the distribution using `GENIE`.

Besides, the mean of the momentum bias in BWD and HABWD selections is around $20 MeV/c$. Fig. D.5 points to the fact that the momentum bias is directly related to the number of migrated layers, with a similar dependency for all the samples. The bias is less evident in the FWD and HAFWD selections

because the amount of migrations is lower.

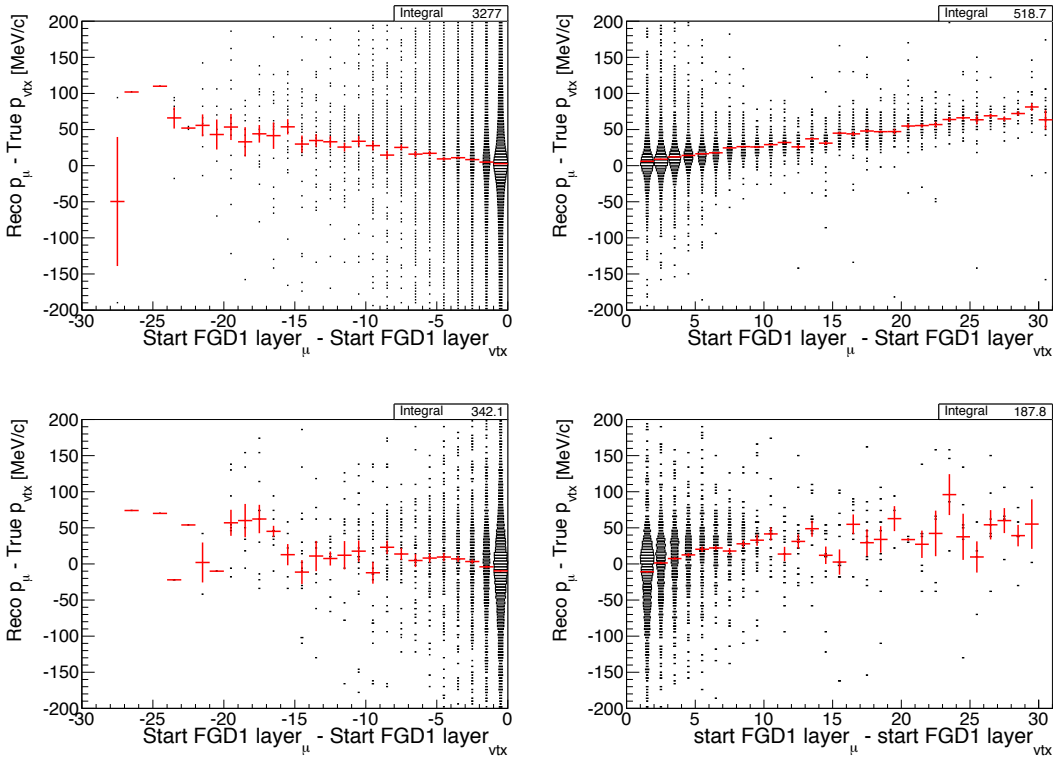


Figure D.5: Difference between the FGD1 layer associated to the reconstructed start position of the $\mu^-$ candidate and the true start position of the vertex versus the difference between the reconstructed and true momentum of the $\mu^-$ candidate for events affected by vertex migration produced by hadrons: FWD (top left), BWD (top right), HAFWD (bottom left), HABWD (bottom right). Red marker indicate the mean momentum difference.

MC prediction of both the amount of migrations and number of layers that the vertex is migrated might not represent correctly the data. To quantify such discrepancy, the energy loss in the FGD1 is compared between data and MC (subtracting to the reconstructed momentum, the reconstructed momentum in the TPC segment). The agreement between data and MC for that distribution is good. Then, it is concluded that the momentum bias is similar.

However, a conservative approach has been followed. The idea is to bias the energy loss in MC until the discrepancy between data and MC is large (defining a threshold factor). It is found that up to 7 MeV/c the energy loss distributions are similar. Therefore, an smearing factor of 7 MeV/c ( 3 layers because the energy loss in plastic for a $\mu^-$ is $\sim$2MeV/cm) is applied to the reconstructed momentum for tracks starting or ending in the FGDs.

# Appendix E

# Efficiency per Reaction Type.

This chapter details the signal efficiency split in different reaction types contained in the CC inclusive interactions. It is important to notice that 2p2h is not implemented in `GENIE` generator, so no efficiency is expected in that case. The coherent channel is not included because the statistic is very low.

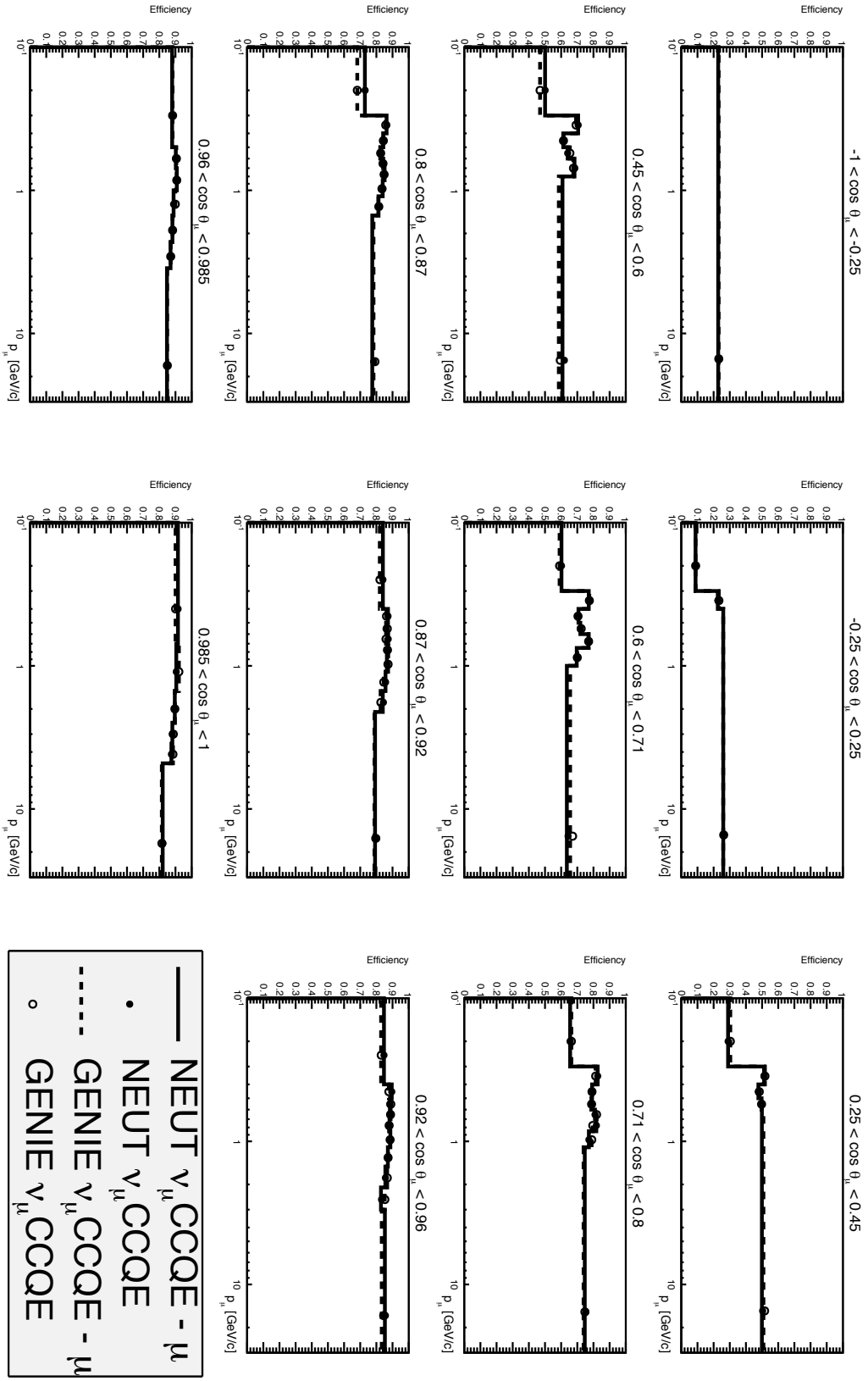


Figure E.1: Reconstruction signal efficiency as function of the momentum and angle of the true $\mu^-$ for CCQE interactions.

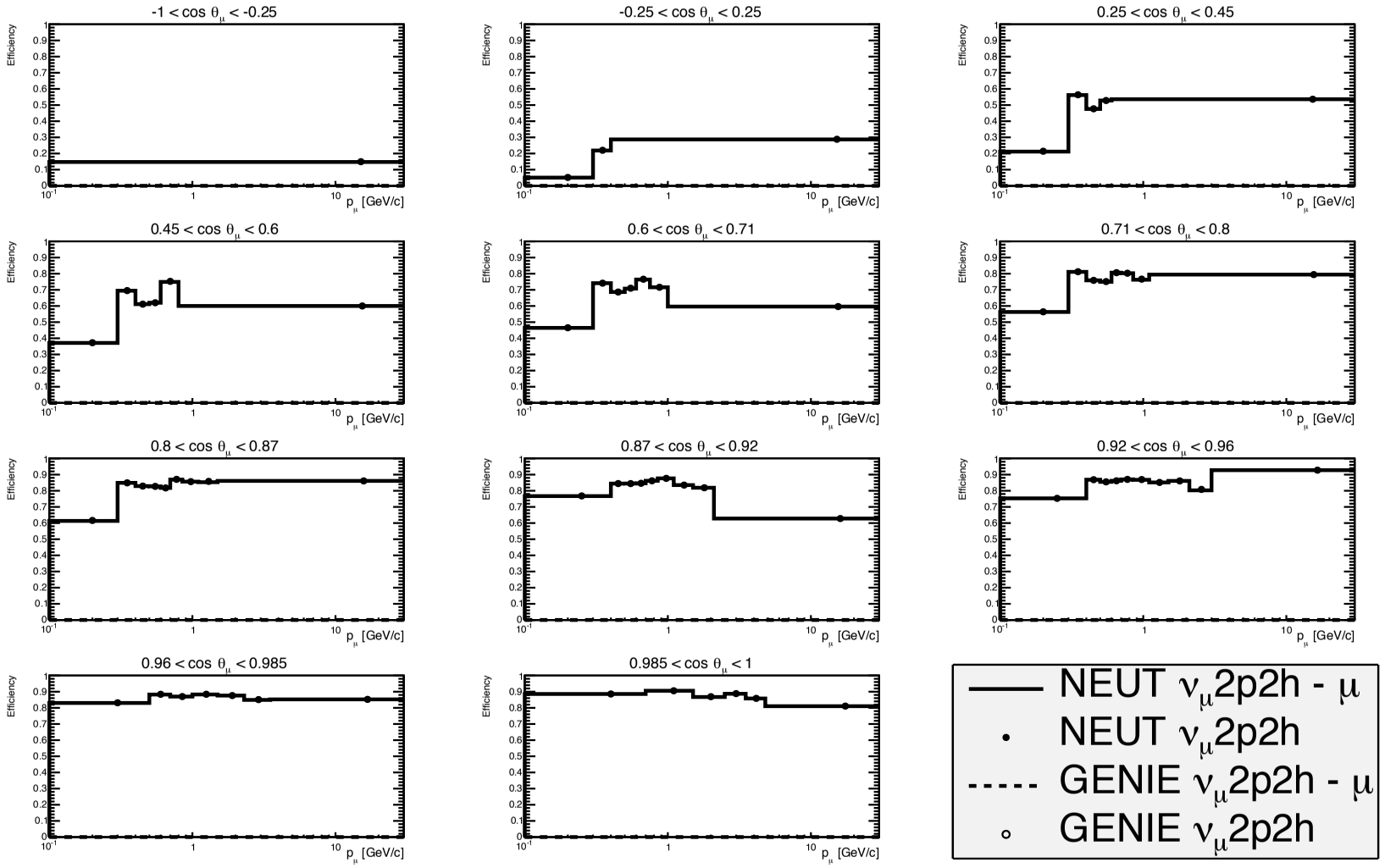


Figure E.2: Reconstruction signal efficiency as function of the momentum and angle of the true $\mu^-$ for 2p2h interactions.

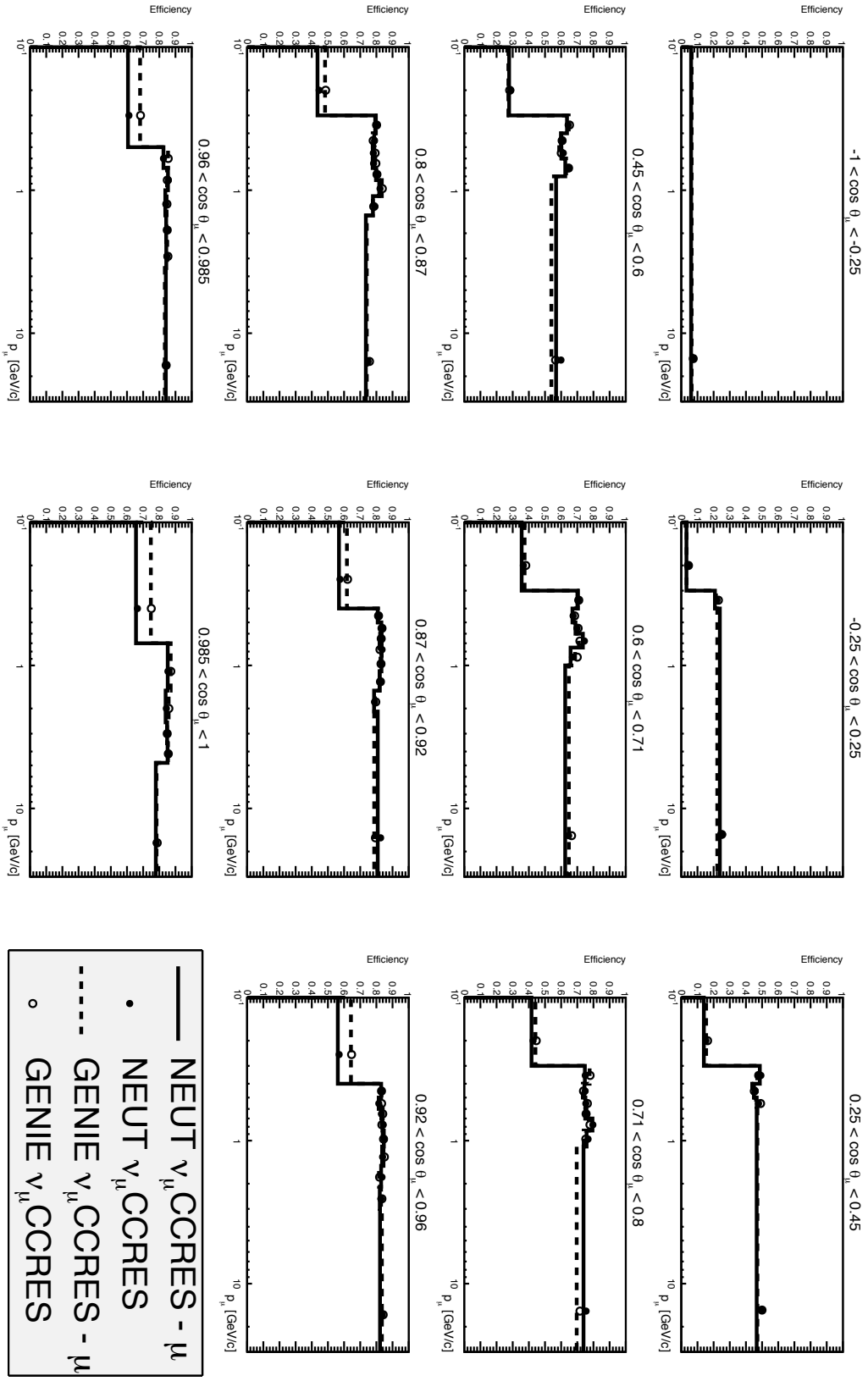


Figure E.3: Reconstruction signal efficiency as function of the momentum and angle of the true $\mu^-$ for CCRES interactions.

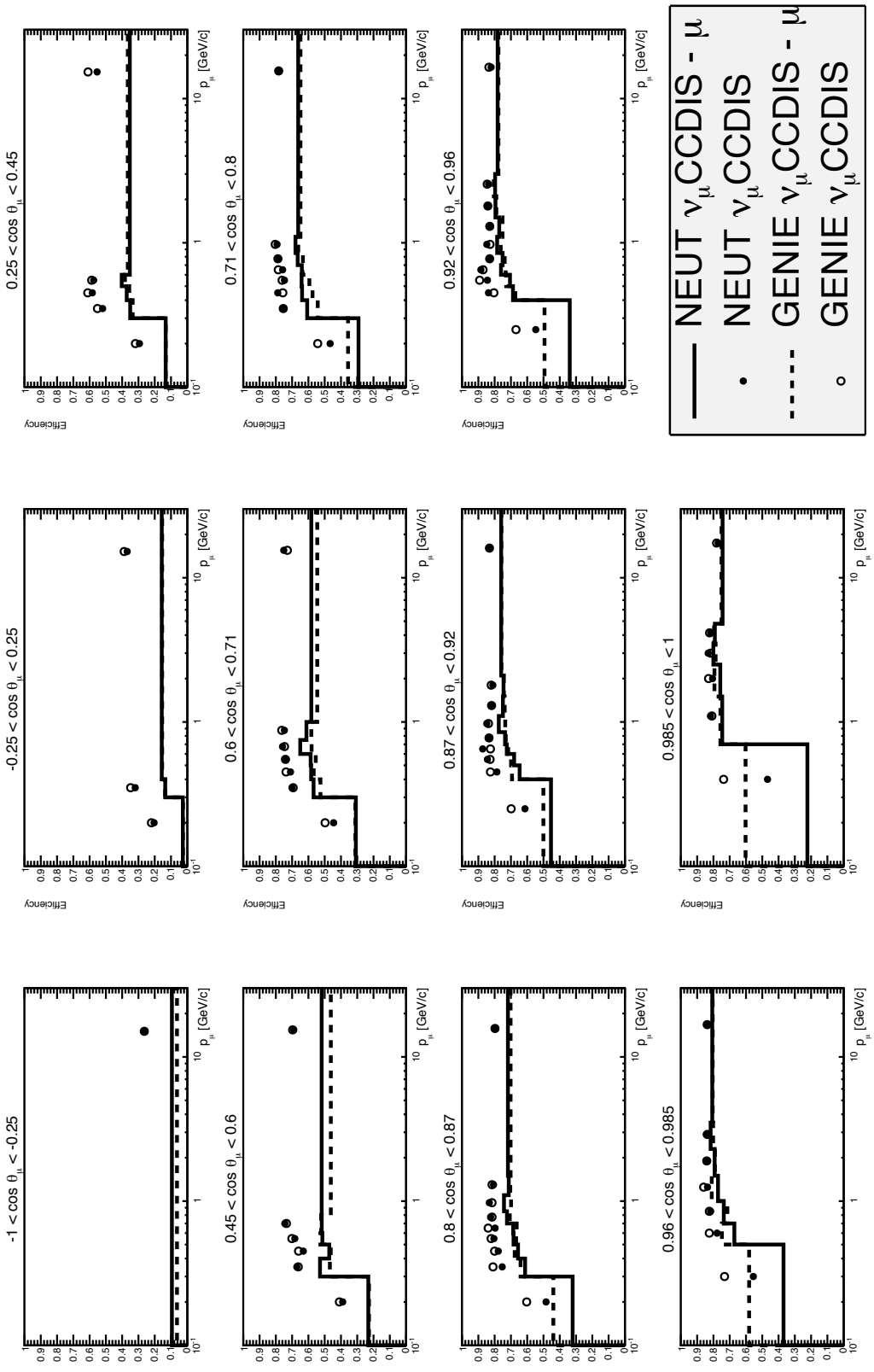


Figure E.4: Reconstruction signal efficiency as function of the momentum and angle of the true $\mu^-$ for CCDIS interactions.

# Appendix F

# Uncertainties Validation

In this chapter, the impact of each source of uncertainty on the cross section result is described in detail. This study is done using the same procedure described in Sec. 10.7.6 using 500 toys.

To begin with, it is important to check that the thrown parameters associated to each systematic uncertainty are behaving properly. In Fig. F.1, the distribution for each parameter is compared with its associated prior after 500 toys. Such distribution is centered at the nominal value of each parameter. Besides, it has a width which correspond to the uncertainty associated to each parameter (small deviations are due to the tight valid range imposed for some theoretical parameter).

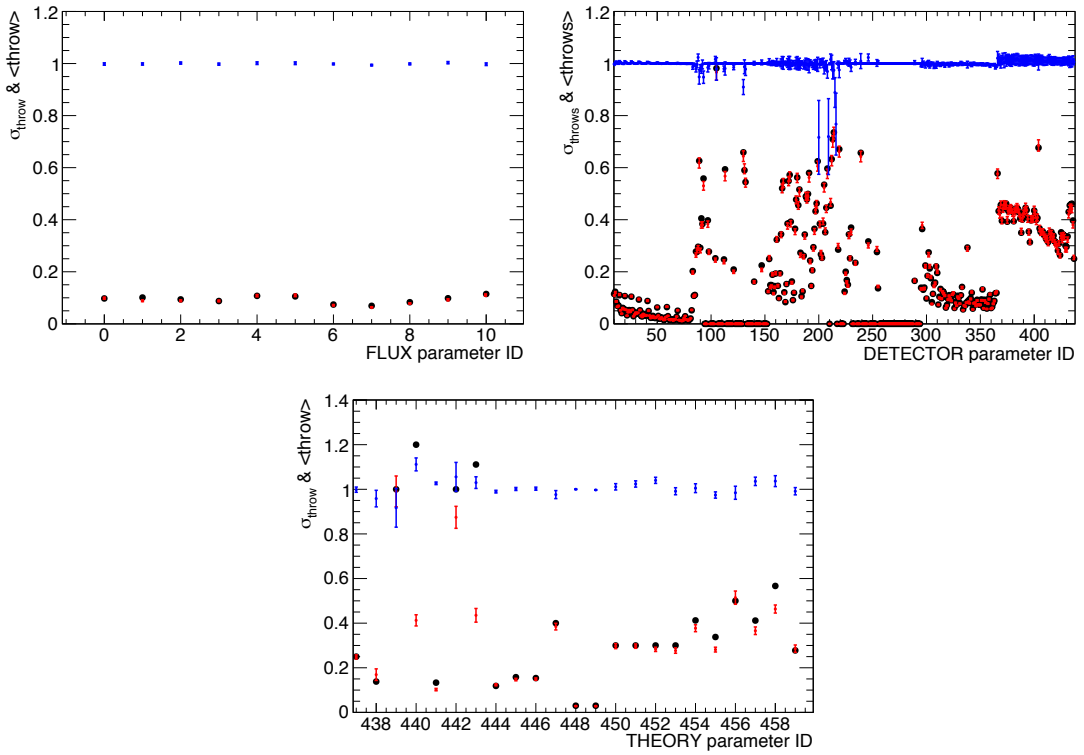


Figure F.1: Comparison between thrown values and prior mean and errors for the parameters associated to each systematics uncertainty. Blue (red) dots indicate the mean (rms) of the distribution for thrown parameters. Black dots represent the prior error obtain from the diagonal of the covariance matrix (prior mean is always one). Flux (top left); detector (top right); modeling (bottom).

An interesting study is to break down the different contributions from Eq. 10.13, so the impact of each uncertainty in the efficiency or number of reconstructed events can be understood. Fig. F.2, Fig. F.3 and Fig. F.4 shows the relative error associated to different terms in Eq. 10.13 when applying fluctuation due to MC statistic, flux and detector uncertainties respectively. In the case of the flux, the cross section uncertainty is dominated by the error in the integrated flux $\Phi$. Meanwhile, for detector and MC statistic the uncertainties are of the same order in the number of reconstructed events (affected by background estimation and smearing matrix) and reconstruction efficiency.

Fig. F.5 and Fig. F.6 shows the relative error associated to different terms in Eq. 10.13 when applying fluctuation due to $\pi$ FSI and cross section modeling systematic uncertainties. In the case of $\pi$ FSI, the uncertainty in the number of reconstructed events dominates (background is sensitive to $\pi$ FSI while reconstruction signal efficiency is not). In the case of cross section modeling, the dominant term is the reconstruction efficiency. However, in the regions with higher background contamination (very low and high momentum regions), the term associated to the number of reconstructed events becomes non negligible.

Furthermore, the result with and without including nuisance parameters for $\pi$ FSI and NC interactions is shown for comparison. It can be seen that in the regions of the phase space were the background is larger, the nuisance parameters are able to constrain the uncertainties.

Finally, it is also interesting to show the impact of the modeling systematics broken down the different parameters that are taken into account (see Sec. 9.2). Fig. F.7 and Fig. F.8 shows the relative error on the total cross section associated to each parameter from $\pi$ FSI. Fig. F.9, Fig. F.10 and Fig. F.11 shows the relative error on the total cross section associated to each parameter from cross section modeling.

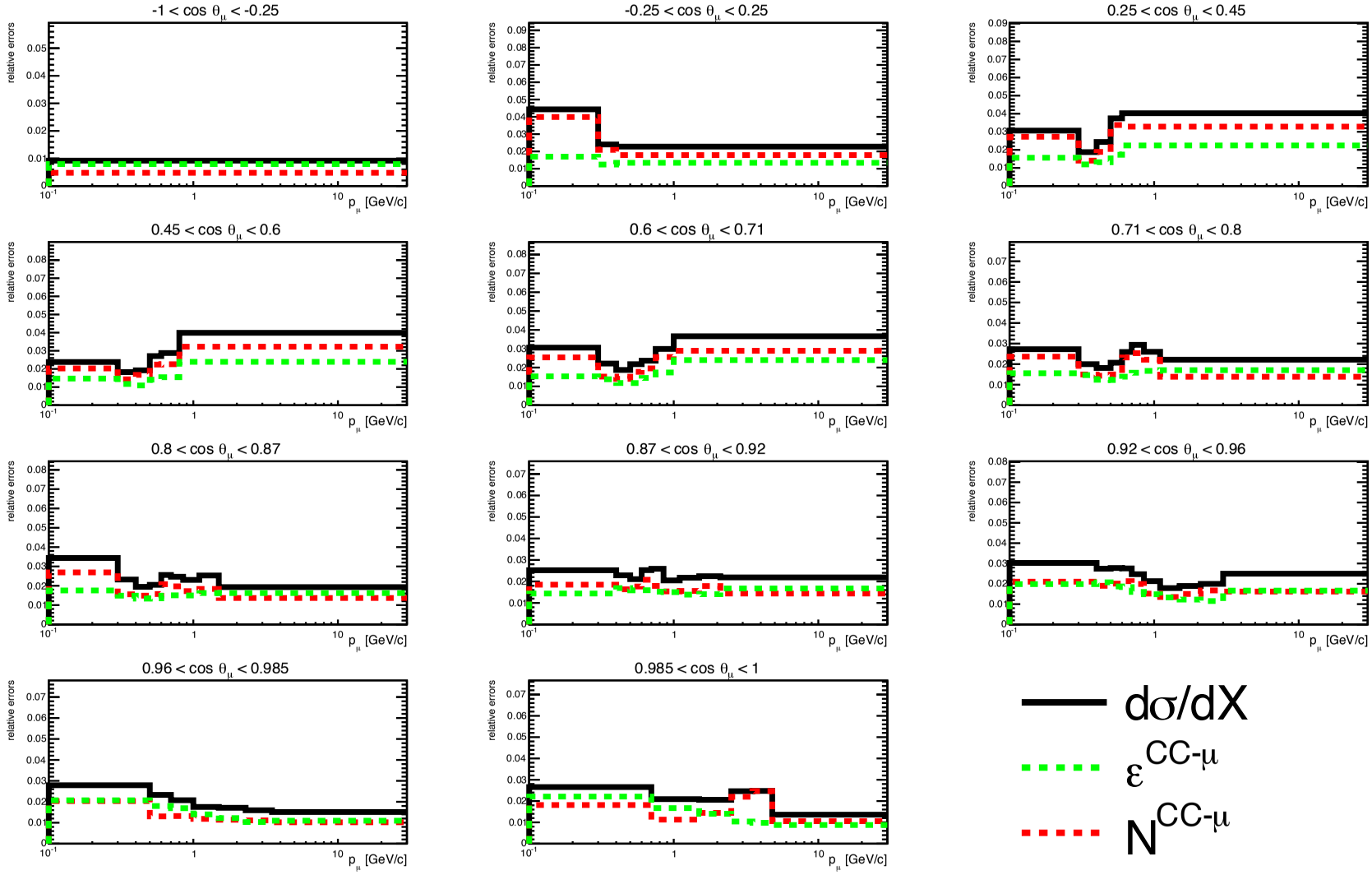


Figure F.2: Relative uncertainty due to MC statistic for cross section (black), efficiency (green) and the number of selected events (red) in Eq. 10.13.

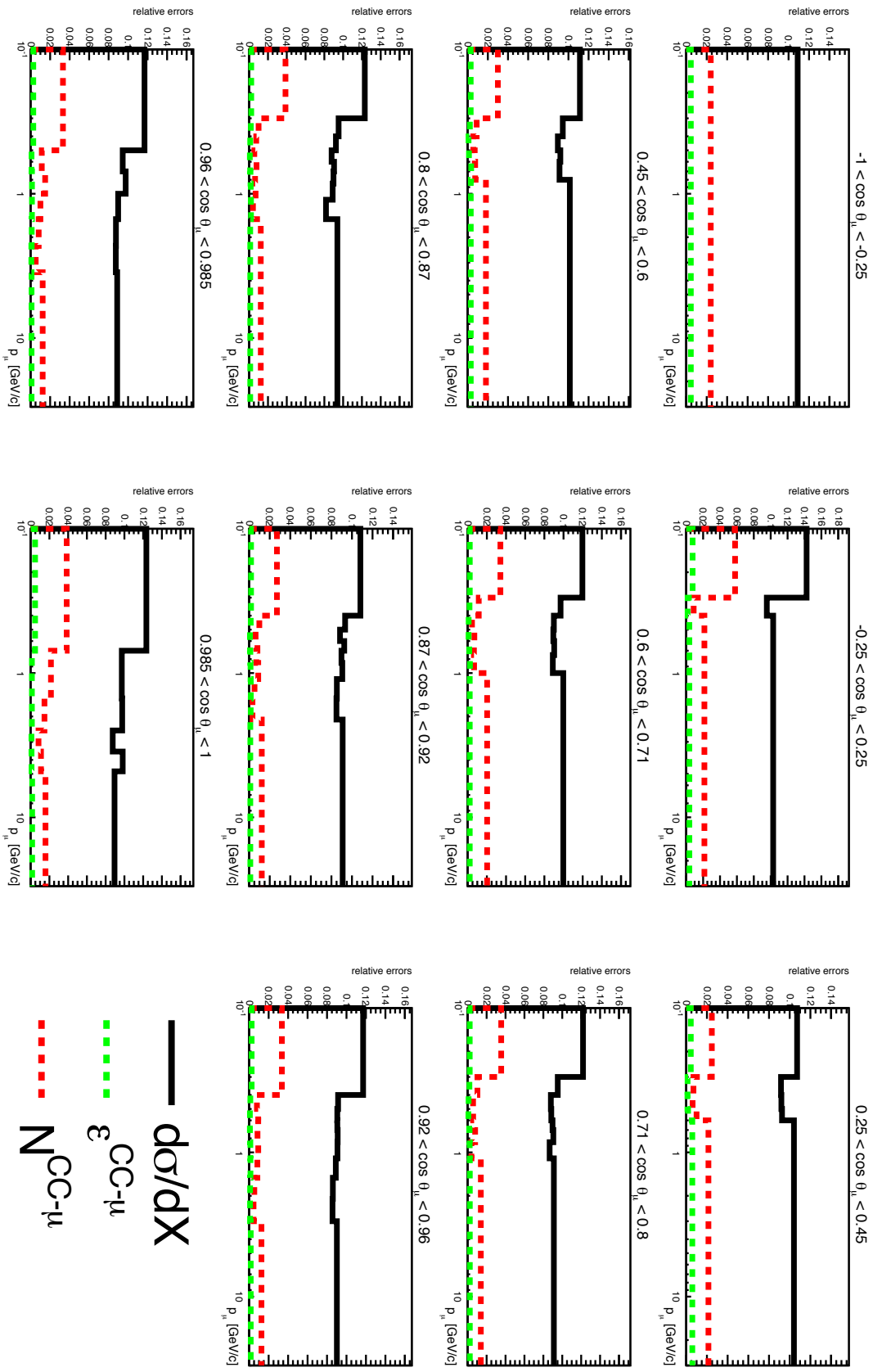


Figure F.3: Relative uncertainty due to flux for cross section (black), efficiency (green) and the number of selected events (red) in Eq. 10.13.

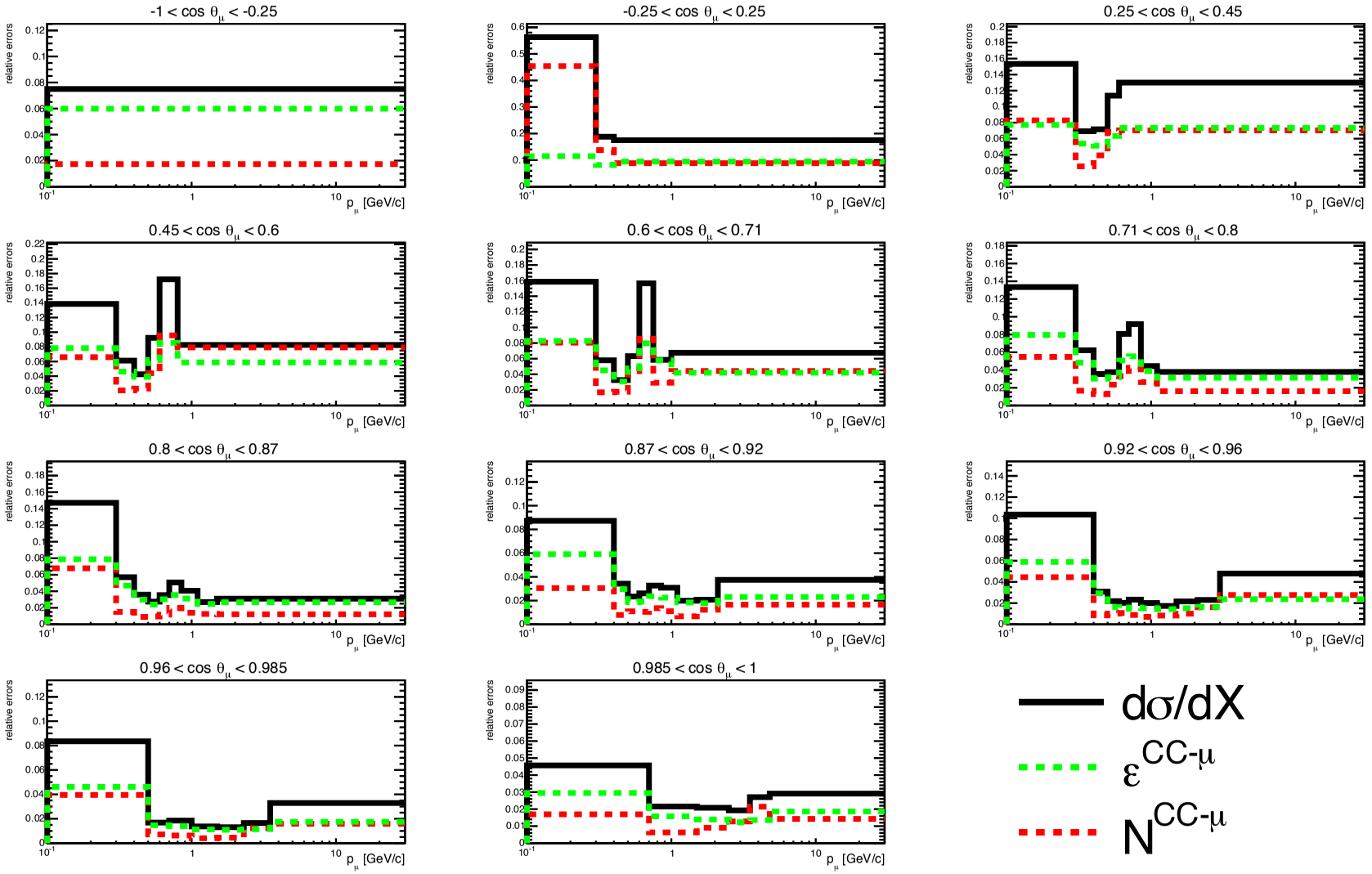


Figure F.4: Relative uncertainty due to detector systematics for cross section (black), efficiency (green) and number of selected events (red) in Eq. 10.13.

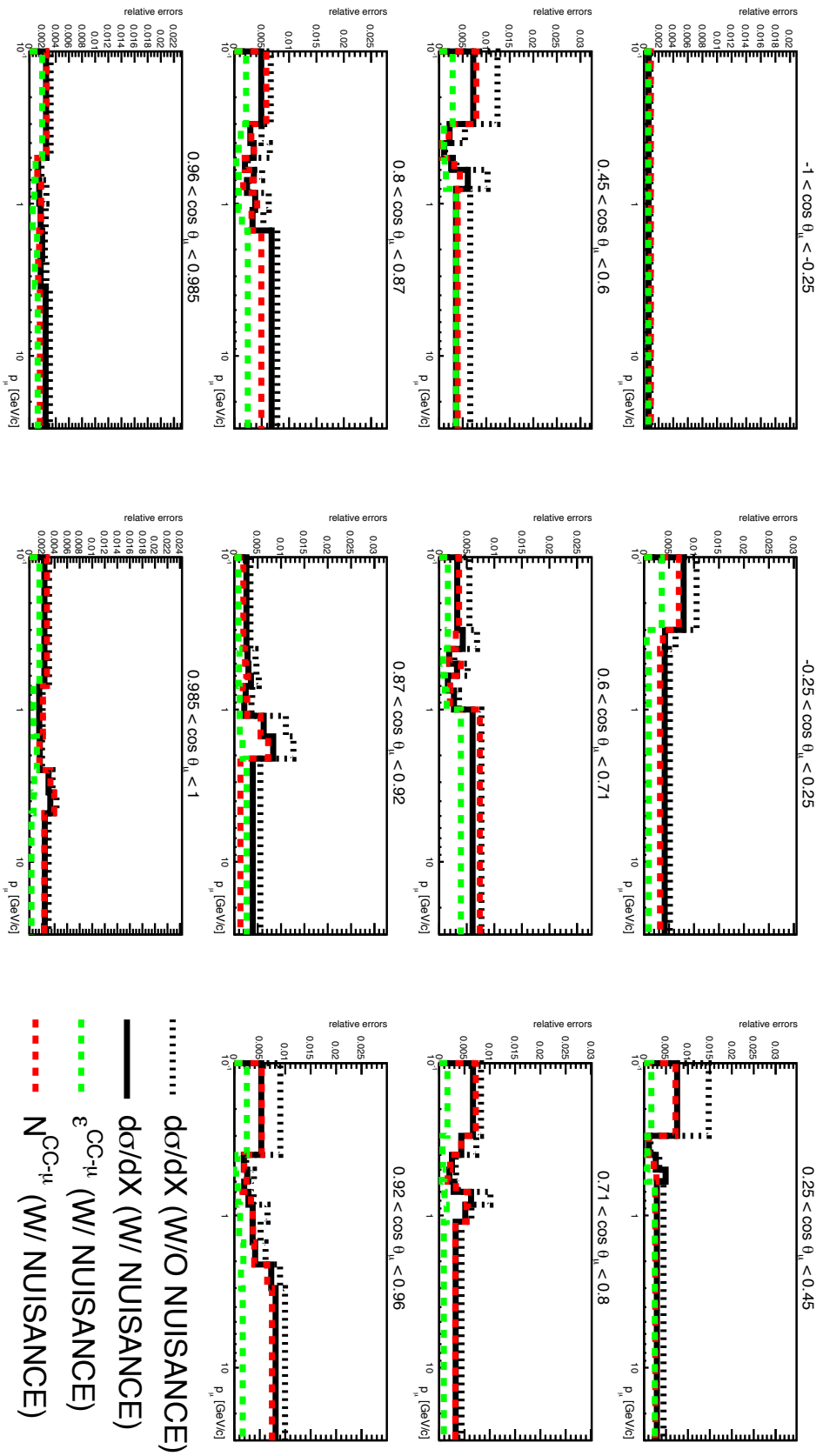


Figure F.5: Relative uncertainty due to $\pi$ FSI modelling for cross section (black), efficiency (green) and the number of selected events (red) when nuisance parameters are included (straight line) and when nuisance parameters are not included (dashed lines).

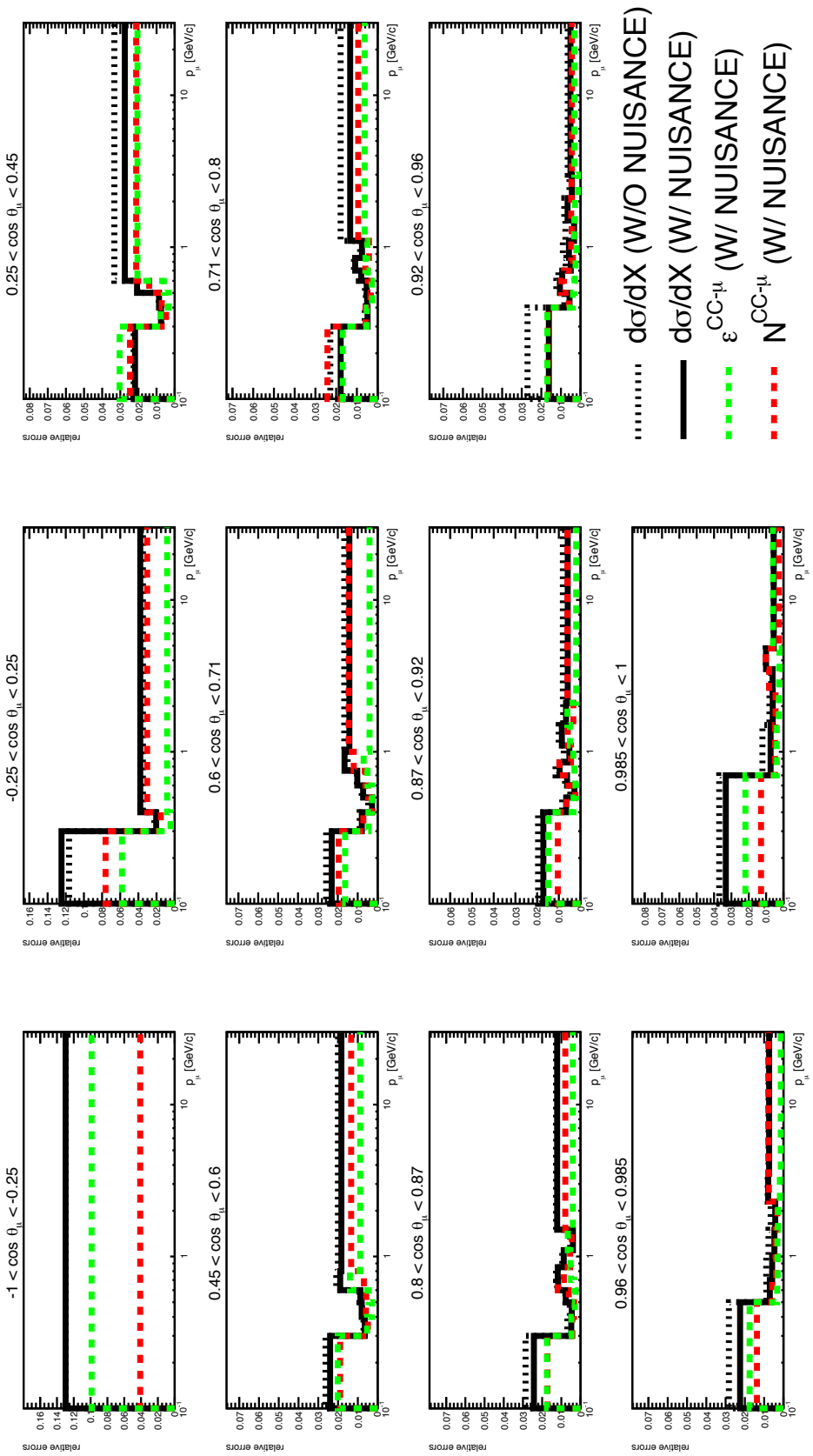


Figure F.6: Relative uncertainty due to cross section modeling for cross section (black), efficiency (green) and the number of selected events (red) in Eq. 10.13 when no nuisance parameters are included (dashed line) or when a nuisance parameter is included for NC interactions (straight lines).

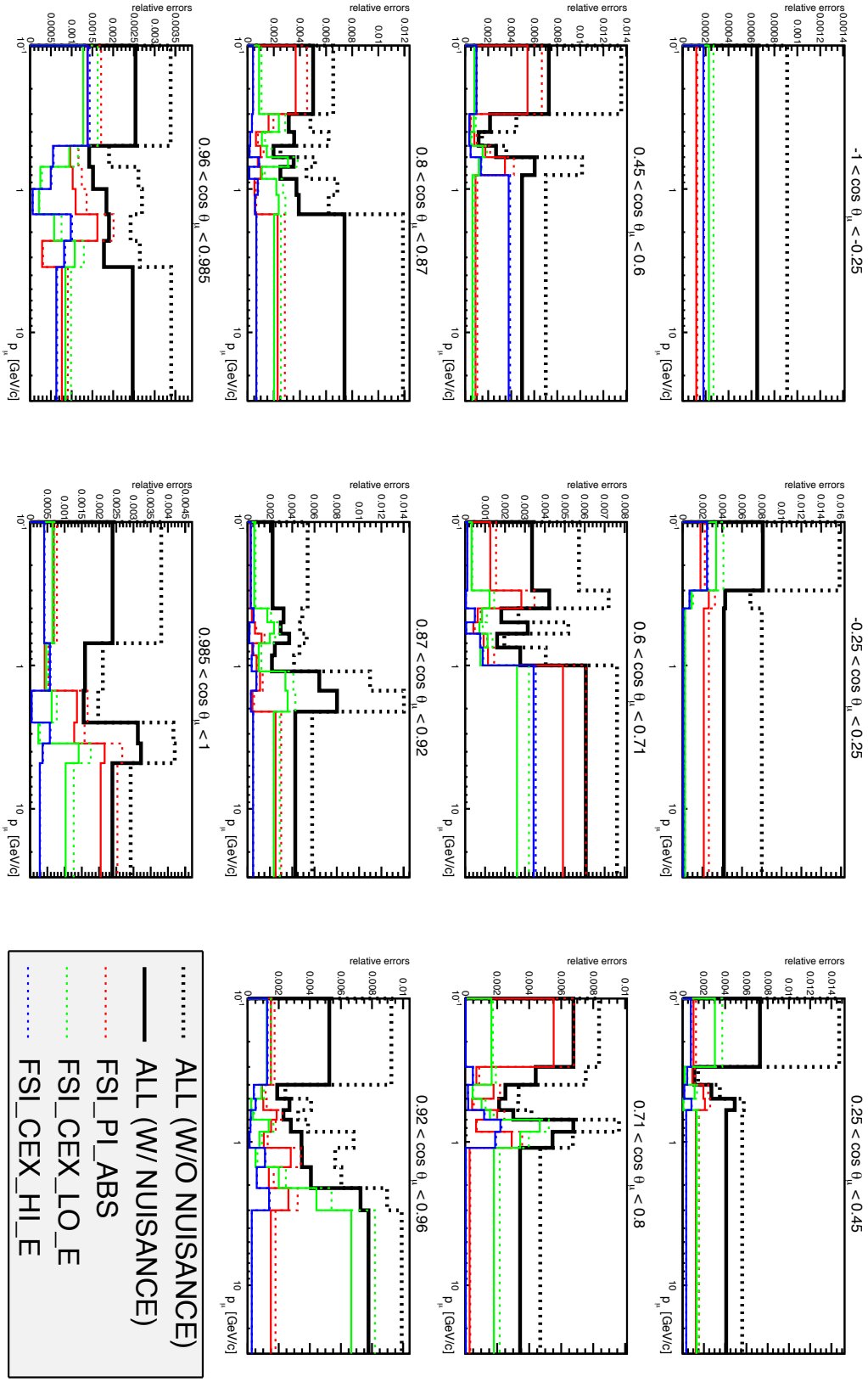


Figure F.7: Relative uncertainty due to $\pi$ FSI modeling for cross section in Eq. 10.13 broken down into the different parameters.

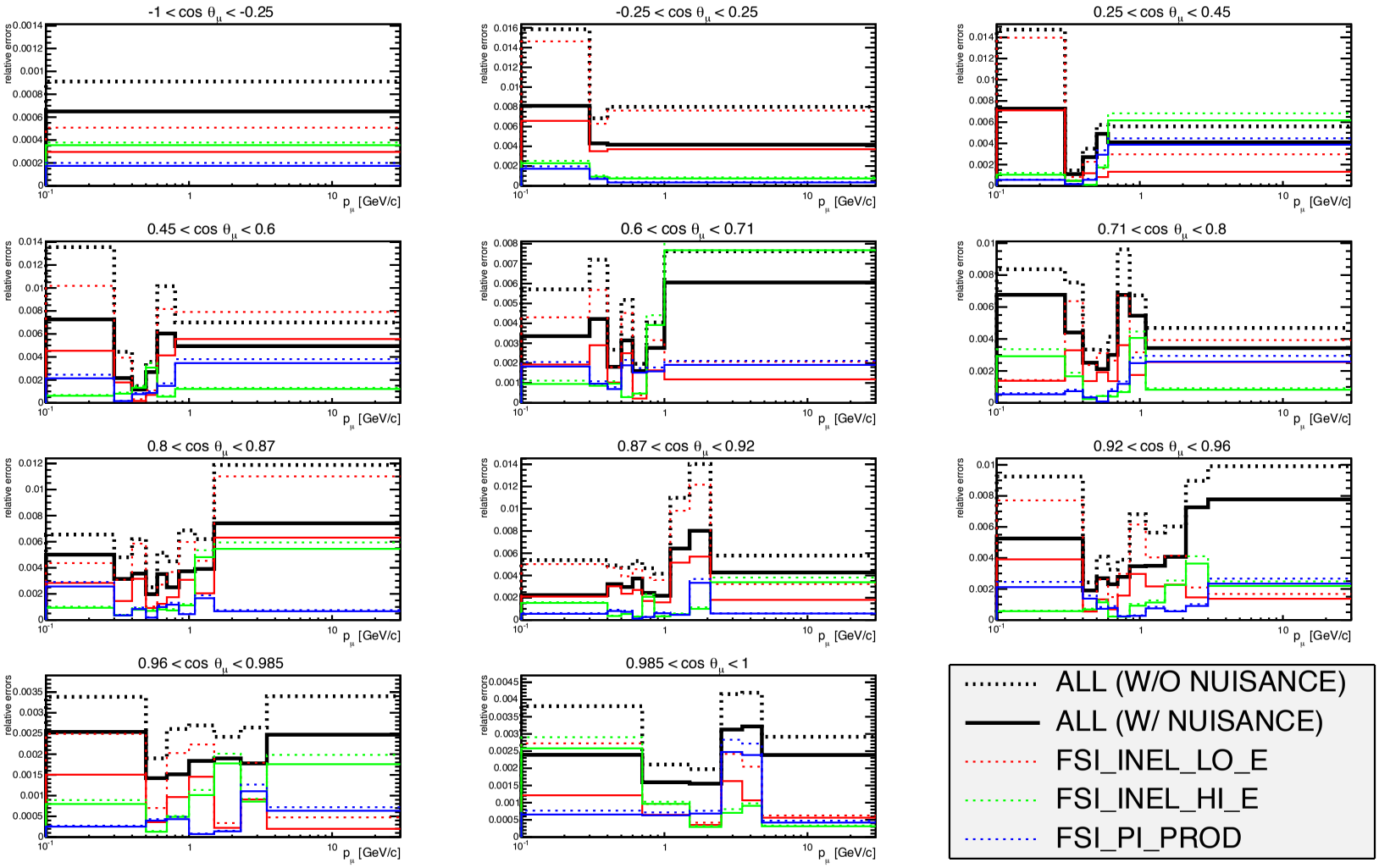


Figure F.8: Relative uncertainty due to $\pi$ FSI modeling for cross section in Eq. 10.13 broken down into the different parameters.

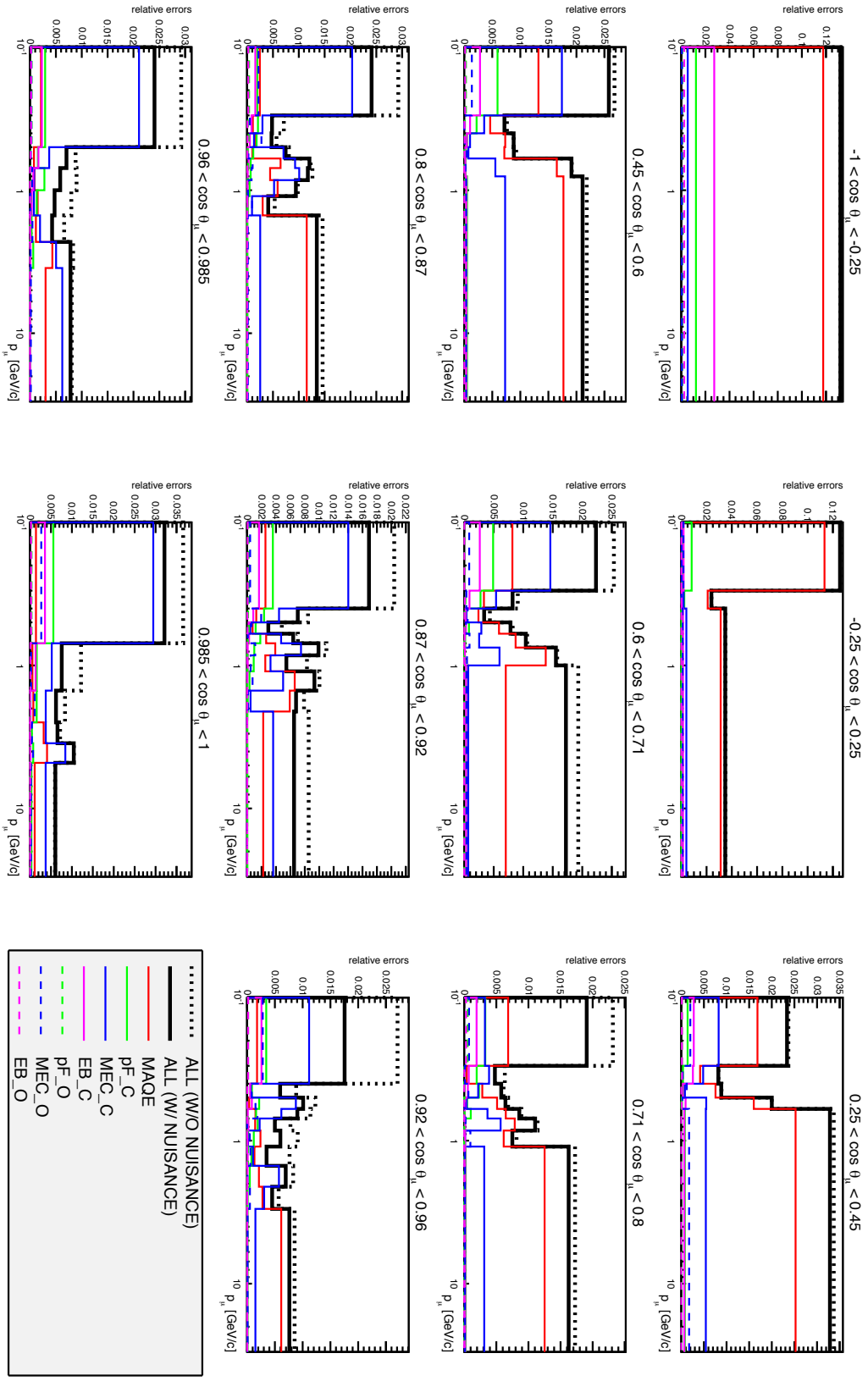


Figure F.9: Relative uncertainty due to cross section modeling for cross section in Eq. 10.13 broken down into the different parameters associated to the modeling of CCQE-like interactions.

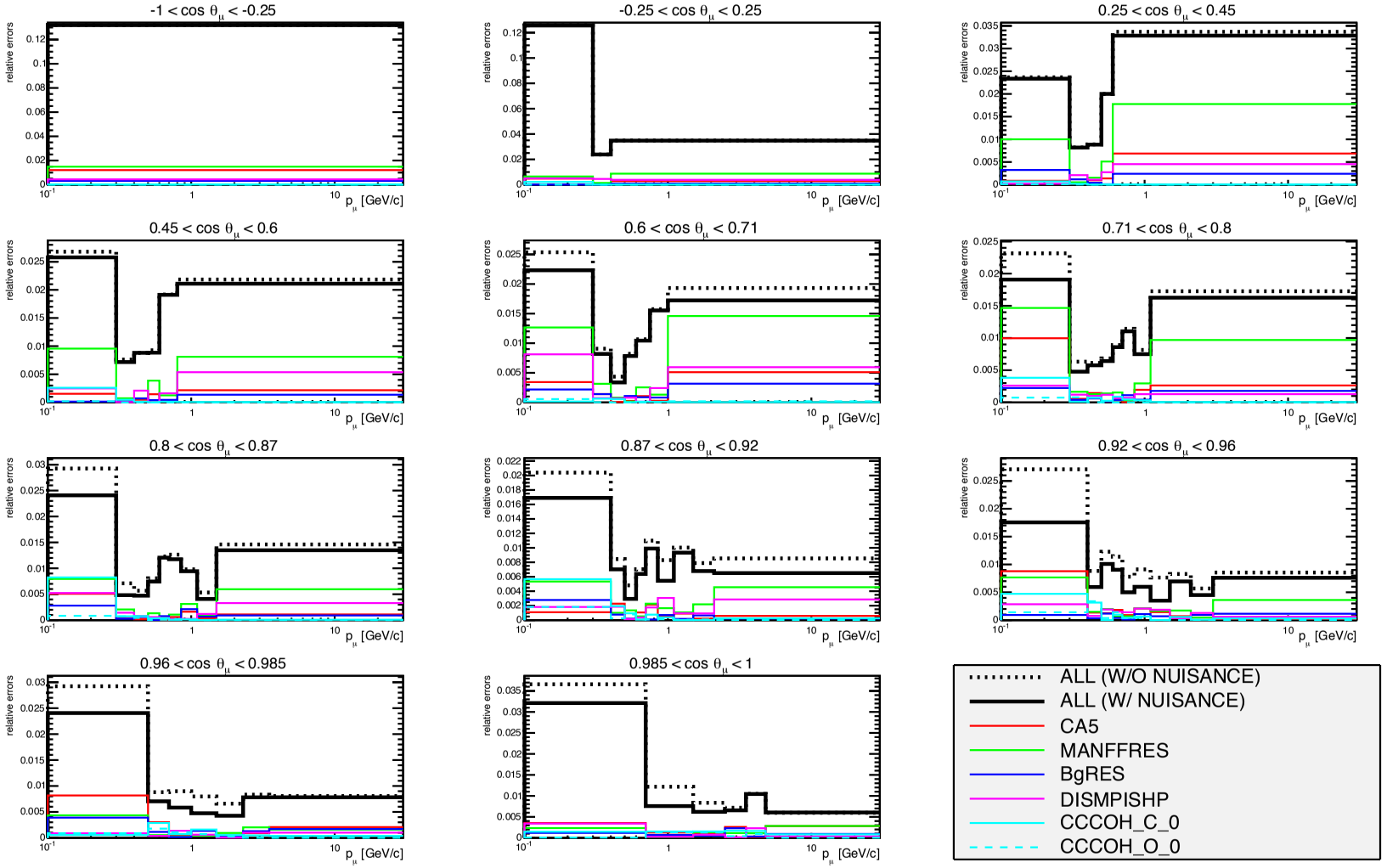


Figure F.10: Relative uncertainty due to cross section modeling for cross section in Eq. 10.13 broken down into the different parameters associated to the modeling of noCCQE-like interactions.

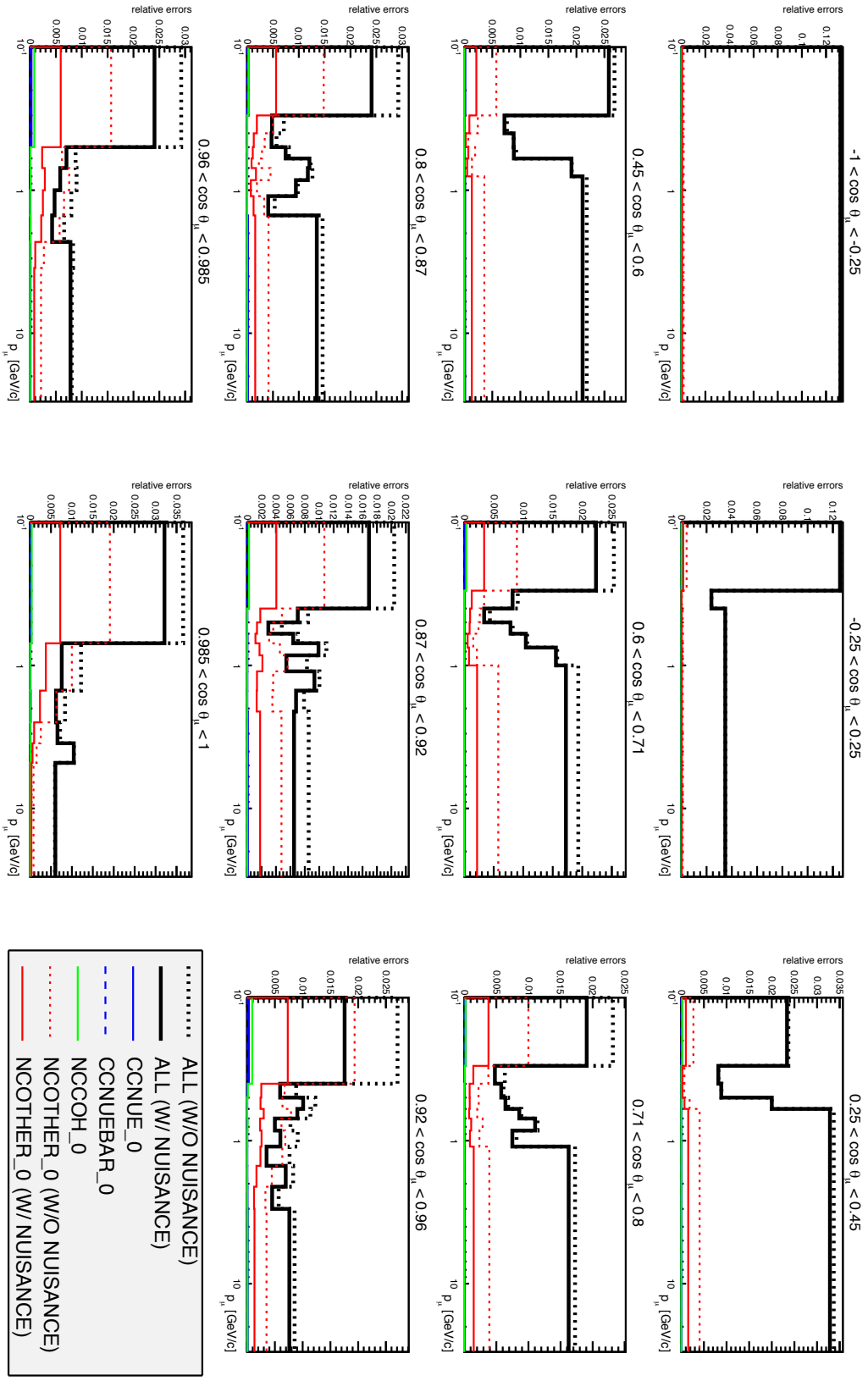


Figure F.11: Relative uncertainty due to cross section modeling for cross section in Eq. 10.13 broken down into the different parameters associated to the modeling of NC and $\nu_e$ interactions.

# Appendix G

# Unfolding Validation

In this chapter, several tests are performed to validate the unfolding algorithm will be discussed. As it was detailed in Sec. 10.1.3, the cross section result is extracted using a maximum likelihood fit.

The performance of the fitted parameters is tested using pulls. Secondly, a bias study will be performed unfolding the MC and using itself as prior. Finally, several fake data samples will be produced and they will be unfolded using as prior both nominal `NEUT` and `GENIE`.

## G.1 Pull Studies

In this section, performance of the fitter machinery is study in detail. The pulls of the free parameters from the fit are a good observable to perform a validation. One can construct "pull" distributions for fitted parameter values from many toy experiments that should have a Gaussian distribution with mean of 0 and width of 1.

The pull for correction factors (see eq. 10.9) is defined as follows:

$$\frac{c_{fit} - 1}{\sigma^2_{fit}} \tag{G.1}$$

Where $c_{fit}$ and $\sigma_{fit}$ are the correction factor and its associated error provided by the minimization algorithm.

For nuisance parameters, the basic idea is that the fitted value should be compared with the true value of the fake dataset.

$$\frac{p_{fit} - p_{nominal}}{\sqrt{\sigma^2_{prior} - \sigma^2_{fit}}} \tag{G.2}$$

Where $p_{fit}$ and $\sigma_{fit}$ is the nuisance parameter and its associated error provided by the minimization algorithm. $p_{nominal}$ is the nominal value of the dial associated to each nuisance parameter. $\sigma_{prior}$ is

the associated uncertainty used to perform the Gaussian throw for each dial (see Sec. 9.2). The pull distribution for each parameter is fitted with a Gaussian function $G(\mu, \sigma)$. The mean and width will be the $\mu$ and $\sigma$ parameters respectively.

### G.1.1 Without Systematics

Data statistical fluctuations are applied to nominal `NEUT`. Then, it is unfolded using nominal `NEUT` as prior. After 500 toys, pulls distribution for the correction factors are fitted to a Gaussian. Pull mean and width are compatible with zero and one respectively (see Fig. G.1). In this case, both methodologies give equivalent results.

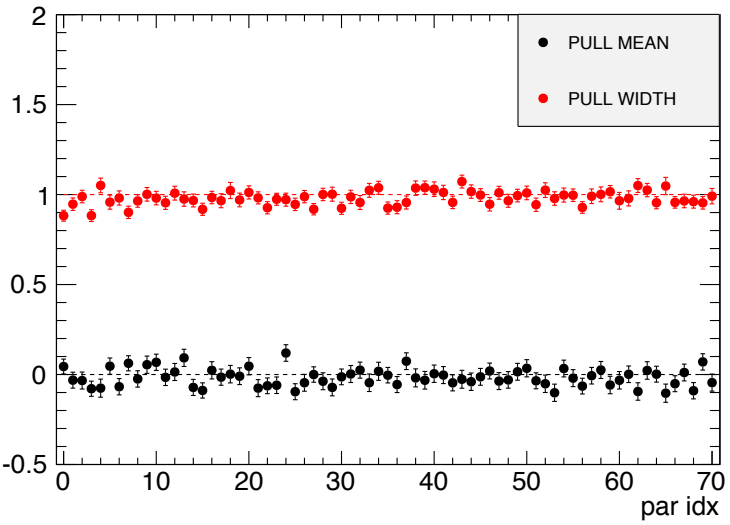


Figure G.1: Pull mean and width for correction factors for 500 toys with statistical variation only.

### G.1.2 With Systematics

In this test, the same methodology is followed. However, apart from statistical fluctuation, systematics uncertainties due to $\pi$ FSI and NC interactions are also taken into account. Therefore, the reconstructed distribution is unfolded using reweighted `NEUT` as prior.

One of the problems is that when including nuisance parameters, the minimization algorithm is not able to compute a reliable error matrix for the free parameters for $\sim 50\%$ of the toys, thus $\sigma_{fit}$ values are not reliable. Therefore, pulls distribution includes only toys in which the error matrix is reliable.

Fig. G.2 shows the mean and width of the pulls after 500 toys are thrown.

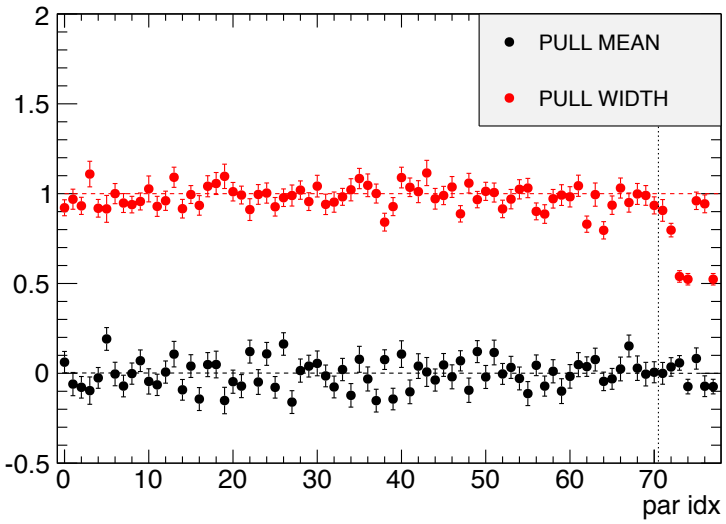


Figure G.2: Pull mean and width for correction factors and nuisance parameters for 500 toys applying systematics (*pi* FSI and NC interactions) and statistical variation.

$\pi$ FSI nuisance parameters do not show a normal distribution for its associated pulls. As it was shown in Sec. 9.2, nuisance parameters associated to $\pi$ FSI are not very sensitive to fluctuation of $\pi$ FSI predictions. Besides, some of them are thrown in a very restricted range and they are highly correlated. These two facts could be the explanation for such deviations in the pull distributions.

## G.2 Bias Study

Another closure test is to check that the average result after unfolding nominal MC with itself as prior does not deviate from the truth nominal MC. Therefore, 500 toys are produced applying systematics and statistical fluctuations to nominal `NEUT`. Then, those distributions are used to unfold the reconstructed distribution from nominal `NEUT`.

The rate of reconstructed events in each bin (of true kinematics) for the fit and the nominal MC should be the same. Then, the bias is computed using the following formula:

$$\hat{N}_t^{CC-\mu,FIT} - \hat{N}_t^{CC-\mu,NOMINAL} \tag{G.3}$$

Two different bias studies has been performed using 500 toys depending on the uncertainties that has been taken into account: statistic and systematic; only systematics. For each bin, the distribution from Eq. G.3 shows a Gaussian behavior, so they are fitted to a Gaussian function $G(\mu, \sigma)$. The bias is obtained from the $\mu$ parameter. Fig G.3 summarizes the relative value of the bias per each bin which is always below 3%.

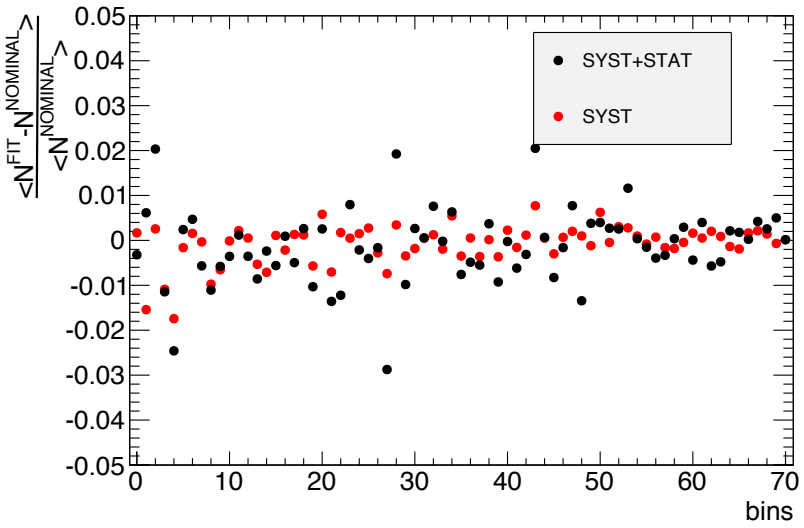


Figure G.3: Mean of the bias between the number of reconstructed event obtained from the fit and the fake data in each true bin. 500 toys were used. Nuisance parameters are included for $\pi$ FSI and NC interactions.

## G.3 Fake Data Tests

In this section several fake dataset will be studied in detail. These fake data are produced either biasing nominal `NEUT` or with an alternative generator `GENIE`. Then, those fake data distribution will be unfolded. Nuisance parameters are included for $\pi$ FSI and NC interactions.

In order to take into account the statistical and systematic uncertainties, the same methodology described in Sec. 10.7 is followed. Thus, the fake data reconstructed distribution will be unfolded with a different prior transfer matrix for each toy experiment.

A $\chi^2$ test can be performed to quantify the difference between average result for the fitted cross section and the true cross section from the fake data set.

$$\chi^2 = \sum_{i=0}^{N_{bins}} \sum_{j=0}^{N_{bins}} \frac{1}{\Delta\frac{d\sigma}{dX_i}\Delta\frac{d\sigma}{dX_j}} \left( \left\langle \frac{d\sigma}{dX_i} \right\rangle - \frac{d\sigma^{FAKEDATA}}{dX_i} \right) \Sigma_{ij}^{-1} \left( \left\langle \frac{d\sigma}{dX_j} \right\rangle - \frac{d\sigma^{FAKEDATA}}{dX_j} \right) \quad \text{(G.4)}$$

### G.3.1 NEUT CCQE Bias

T2KReweight can be used to produce different datasets varying the nuclear model for CCQE interactions. NIWG group did a detailed study fitting some CCQE parameters using external data (see Sec. 9.2). A fake dataset has been produced reweighting the nominal NEUT with the recommended values of those parameters. Table G.1 shows a comparison between those two models.

| | Nominal | Fake data |
|---|---|---|
| Nuclear model | Spectral function | Relativistic fermi gas |
| $M_A^{QE}$ [GeV/c$^2$] | 1.20 | 1.15 |
| $p_F$ $^{12}C$ [MeV/c] | 217 | 223 |
| $p_F$ $^{16}O$ [MeV/c] | 225 | 225 |
| $E_B$ $^{12}C$ [MeV] | 25 | 25 |
| $E_B$ $^{16}O$ [MeV] | 27 | 27 |
| $MEC$ $^{12}C$ % | 100 | 27 |
| $MEC$ $^{16}O$ % | 100 | 27 |
| RPA | - | Relativistic |

Table G.1: Comparison between CCQE/2p2h dials in nominal NEUT and NIWG recommendation.

After 500 toys, the distribution from Eq. 10.13 is computed. The mean and width of such distributions is used to set the average cross section and its associated uncertainty per each bin (see Fig. G.4). Finally, the difference between average result and the fake data cross section is quantify using Eq. G.4 taking into account both systematic and statistical uncertainties (only systematic uncertainties) $\chi^2_{ndof=71} = 3.04259(70.1479)$.

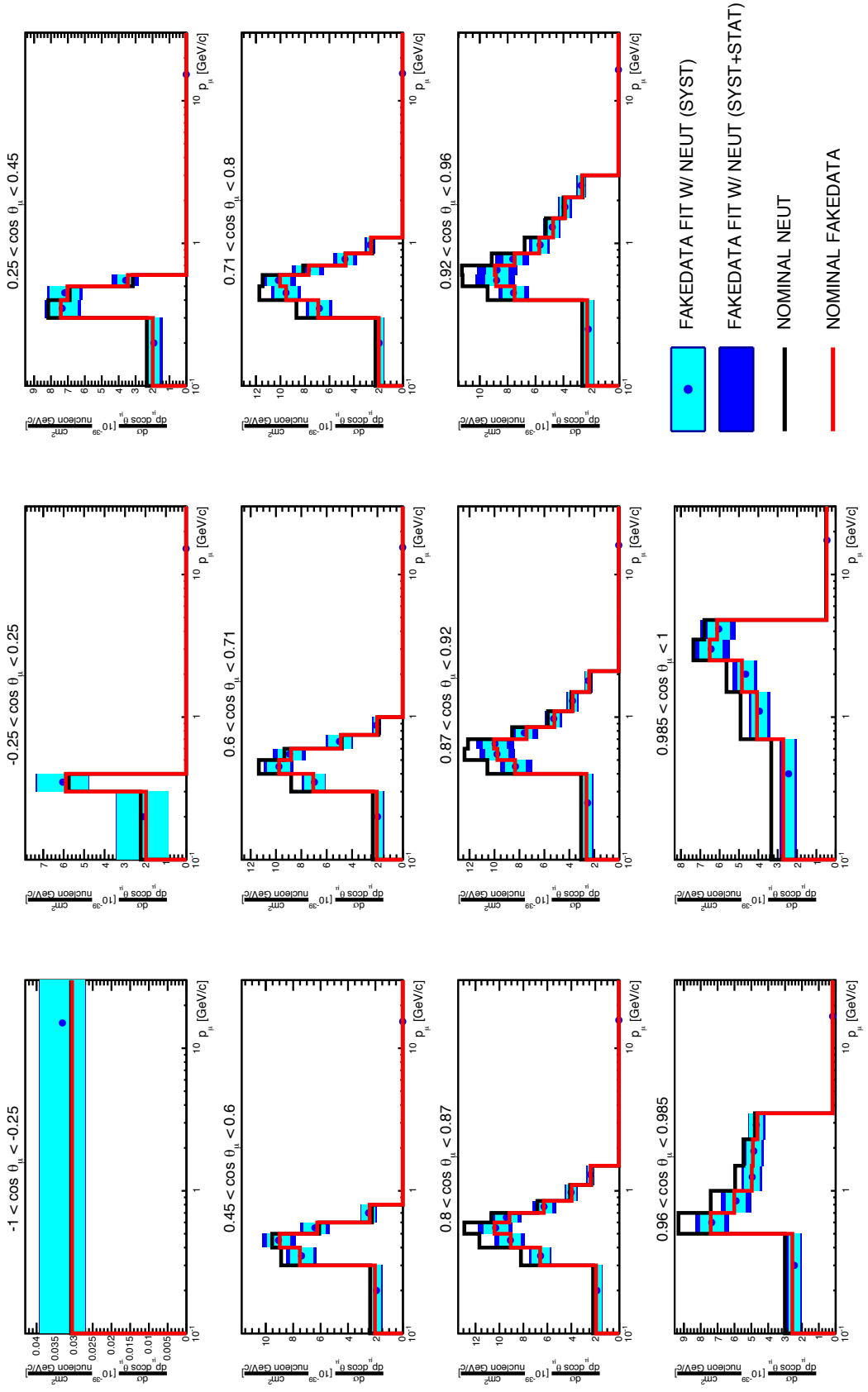


Figure G.4: Flux-integrated double differential cross section per nucleon for nominal NEUT used as prior (black line), nominal NEUT tuned with NIWG recommendation used as fake data (red line) and average result after fitting 500 toys (blue rectangles) after fitting 500 toys.

### G.3.2 NEUT RES Bias

Resonance interactions, in which a $\pi^+$ is produced (apart from the $\mu^-$ and a nucleon), are a non negligible part of the signal at this energy. Nominal NEUT is based on Rein-Sehgal model and three dials can be used to tune this channel (see Sec. 9.2). This model with the current uncertainties is able to describe external data. However, some tension between the normalization of these datasets have been found. Therefore, it is interesting to test the machinery applying a variation to the resonance channel. Thus, the three associated dials will be bias by $+3\sigma$ factor.

After 500 toys, the distribution from Eq. 10.13 is computed. The mean and width of such distributions is used to set the average cross section and its associated uncertainty per each bin (see Fig. G.5). Finally, the difference between average result and the fake data cross section is quantify using Eq. G.4 taking into account both systematic and statistical uncertainties (only systematic uncertainties) $\chi^2_{ndof=71} = 7.179(116.383)$.

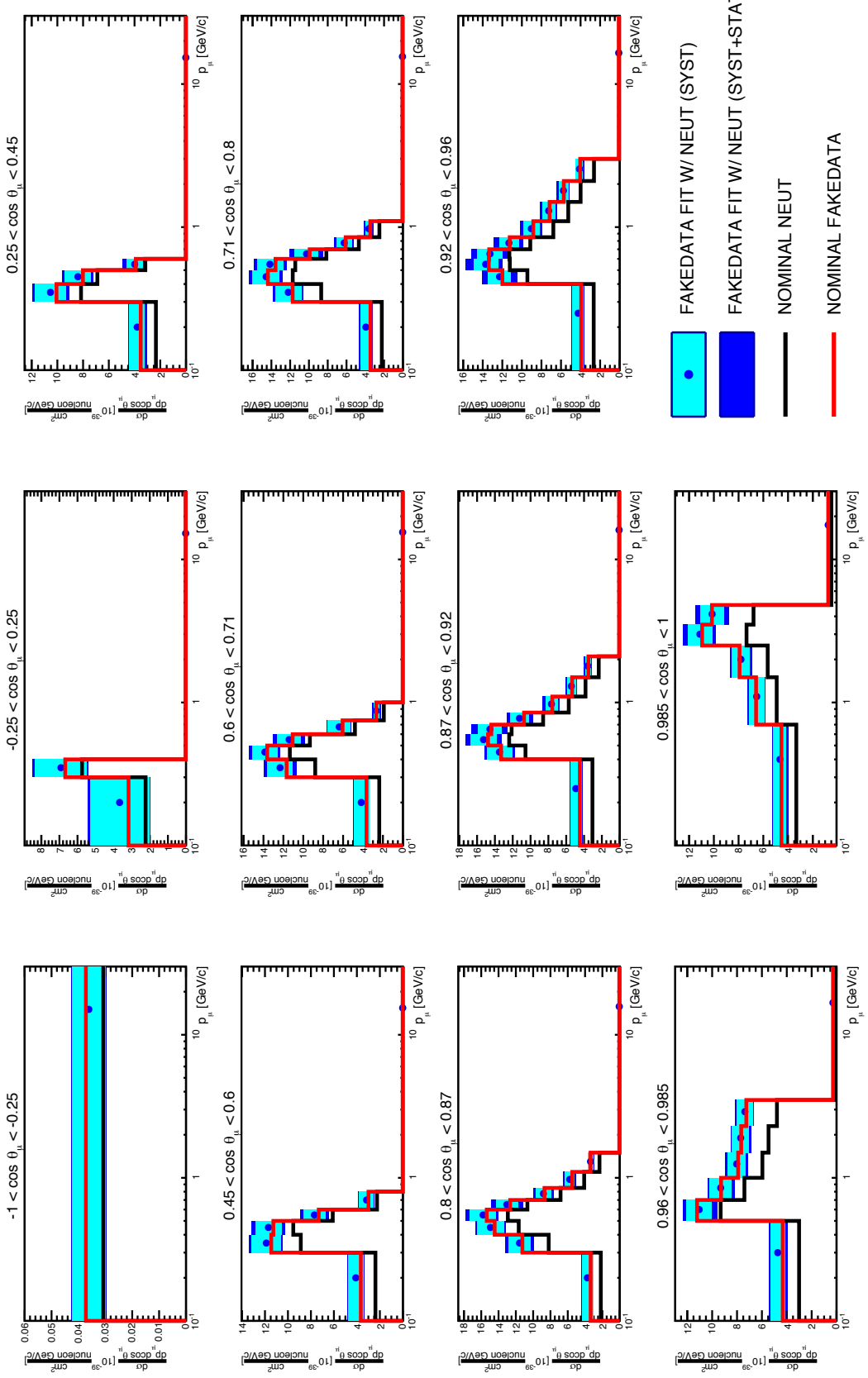


Figure G.5: Flux-integrated double differential cross section per nucleon for nominal MC used as prior (black line), nominal MC tuned by applying a $+3\sigma$ factor to `CA5`, `MANFFRES` and `BgRES` dials used as fake data (red line) and average result after fitting 500 toys (blue rectangles).

### G.3.3 NEUT CC Other Bias

CC other interactions includes CC multi-pi (defined as interactions with more than one $\pi$ produced with an invariant hadronic mass W between 1.3-2.0 GeV) and CC-DIS interactions. The production threshold for this interaction is around 0.6 GeV, thus they are not dominant in this energy range.

In the CC-DIS channel a well known model is used, called PYTHIA, based on parton theory. However, in the multi-pi channel the model used by each generator is different. Current uncertainty is based on external data and it is described in Sec. 9.2. It is interesting to test the machinery applying a variation to CC other channels. Thus, a fake data distribution is generated by scaling up CC other interactions by $+3\sigma$ factor.

After 500 toys, the distribution from Eq. 10.13 is computed. The mean and width of such distributions is used to set the average cross section and its associated uncertainty per each bin (see Fig. G.6). Finally, the difference between average result and the fake data cross section is quantify using Eq. G.4 taking into account both systematic and statistical uncertainties (only systematic uncertainties) $\chi^2_{ndof=71} = 1.48074(31.3175)$.

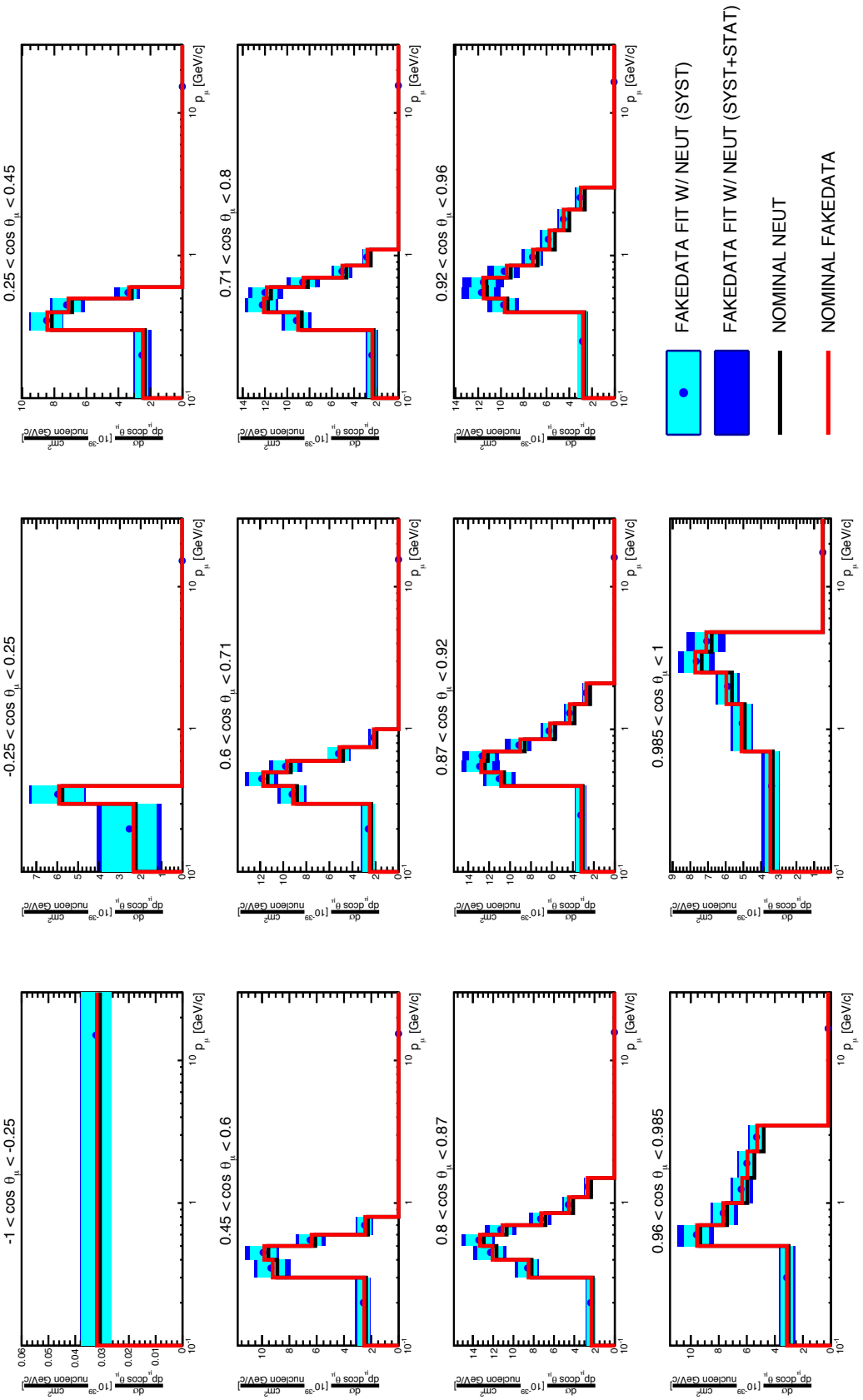


Figure G.6: Flux-integrated double differential cross section per nucleon for nominal NEUT used as prior (black line), nominal NEUT tuned by scaling up CC other interactions by a $+3\sigma$ factor used as fake data (red line) and average result after fitting 500 toys (blue rectangles).

### G.3.4 NEUT Background Bias

NC interactions is the main background in this analysis (apart from out of fiducial volume interaction). Currently, our knowledge about neutral current interactions is limited, so conservatives uncertainties are assumed when modeling these interactions (see Sec. 9.2). Therefore, it is important to check the performance of the machinery when the impact of the background is varied.

A fake dataset is built from nominal NEUT scaling up the NC interaction by a $+3\sigma$ factor, which correspond to a 90% increment of this reaction. Then fake data is unfolded using nominal NEUT.

After 500 toys, the distribution from Eq. 10.13 is computed. The mean and width of such distributions is used to set the average cross section and its associated uncertainty per each bin (see Fig. G.7). Finally, the difference between average result and the fake data cross section is quantify using Eq. G.4 taking into account both systematic and statistical uncertainties (only systematic uncertainties) $\chi^2_{ndof=71} = 1.36534(37.0359)$.

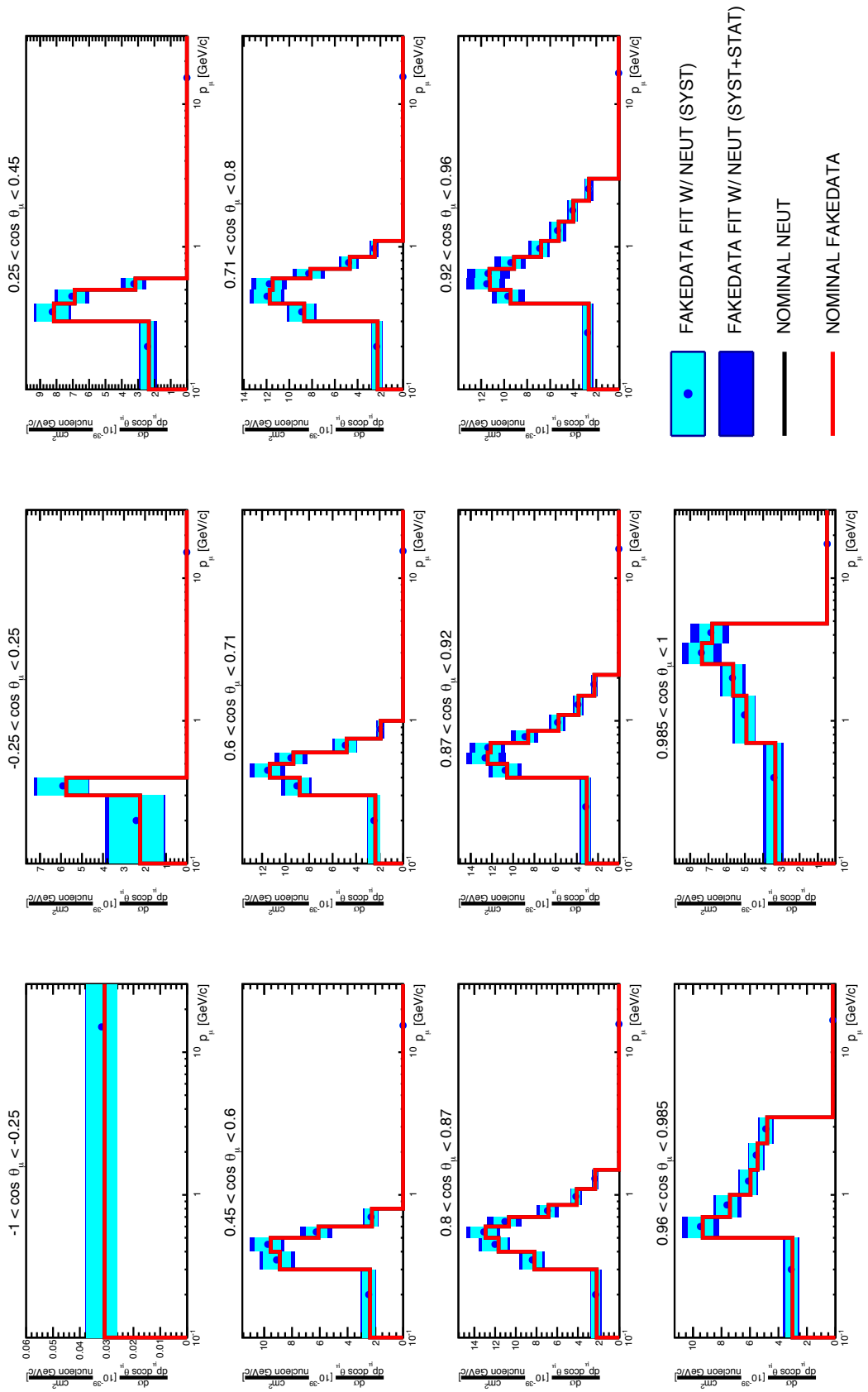


Figure G.7: Flux-integrated double differential cross section per nucleon for nominal NEUT used as prior (black line), nominal NEUT tuned by scaling up by a $+3\sigma$ factor NC interactions used as fake data (same as nominal NEUT) and average result after fitting 500 toys (light blue rectangles).

### G.3.5 GENIE

The alternative generator, called GENIE, is used to produce a fake dataset (normalized to the real data POT). This generator have several differences with the nominal NEUT, mainly the hadron production (see Sec 4.3). Therefore, this test will give an idea of the model dependency of the current fitter.

After 500 toys, the distribution from Eq. 10.13 is computed using as fake data and prior nominal GENIE and NEUT respectively. The mean and width of such distributions is used to set the average cross section and its associated uncertainty per each bin (see Fig. G.8). Finally, the difference between average result and the fake data cross section is quantify using Eq. G.4 taking into account both systematic and statistical uncertainties (only systematic uncertainties) $\chi^2_{ndof=71} = 11.804(576.786)$.

An small bias is observed in the low momentum region for very forward $\mu^-$. This is produced by the efficiency correction, which is significantly different between both generators in that region (see Sec. 10.4).

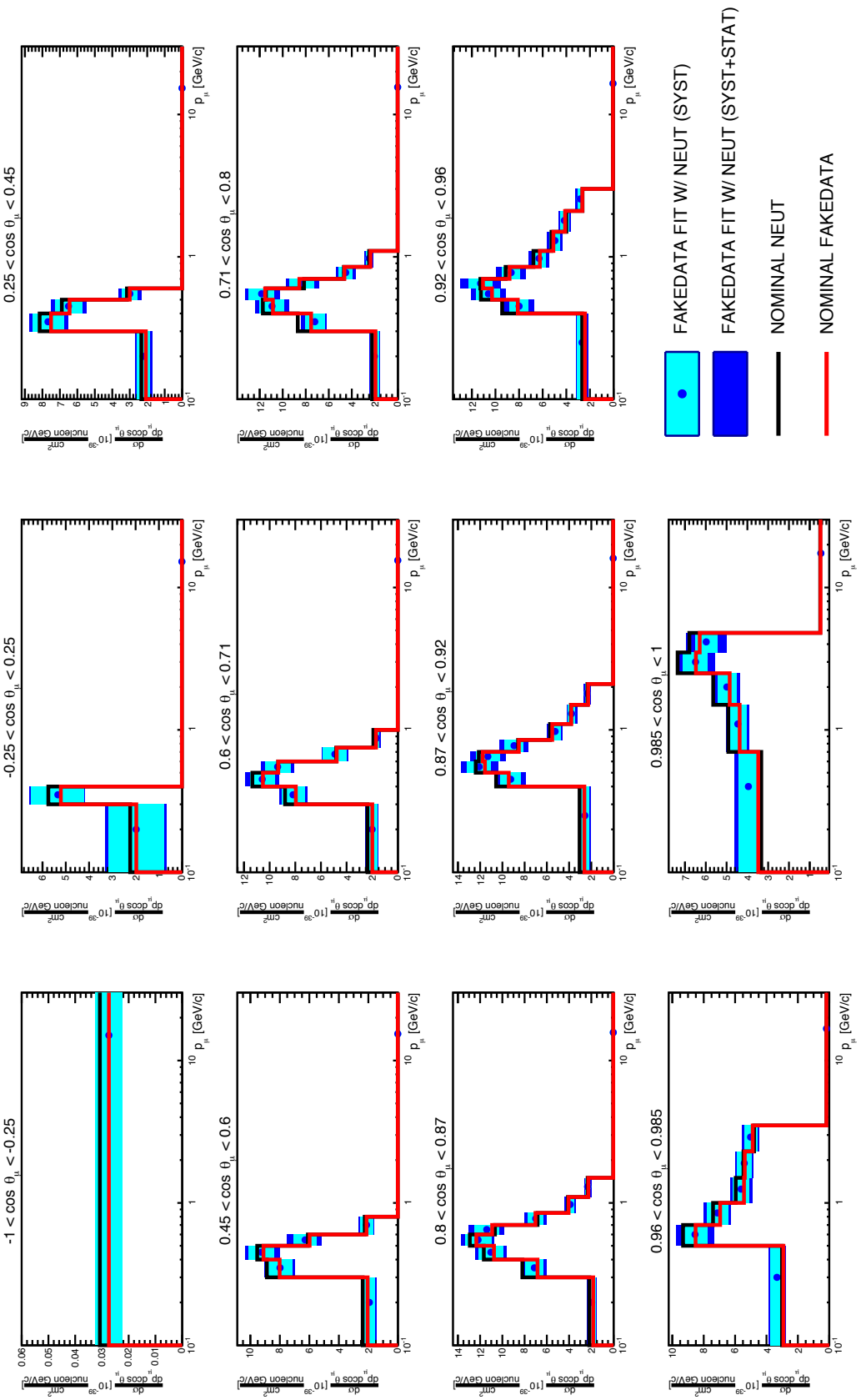


Figure G.8: Flux-integrated double differential cross section per nucleon for nominal NEUT used as prior (black line), GENIE used as fake data (red line) and average result after fitting 500 toys (light blue rectangles).

### G.3.6 Alternative Prior

Using `GENIE` as prior is an important validation for the unfolding. It is also important because it shows how model dependent is the efficiency correction. Therefore, in this test, the fake data distributions are produced with nominal `NEUT`, while `GENIE` is used as prior. An approximation is introduced when performing this test because it uses same response functions for both generators.

After 500 toys, the distribution from Eq. 10.13 is computed. The mean and width of such distributions is used to set the average cross section and its associated uncertainty per each bin (see Fig. G.9). Finally, the difference between average result and the fake data cross section is quantify using Eq. G.4 taking into account both systematic and statistical uncertainties (only systematic uncertainties) $\chi^2_{ndof=71} = 12.3565(581.478)$.

As in the previous fake data test, discrepancies are observed in the very forward and low momentum region. The reason is again the disagreement in the efficiency between both generators (see Fig. 10.8).

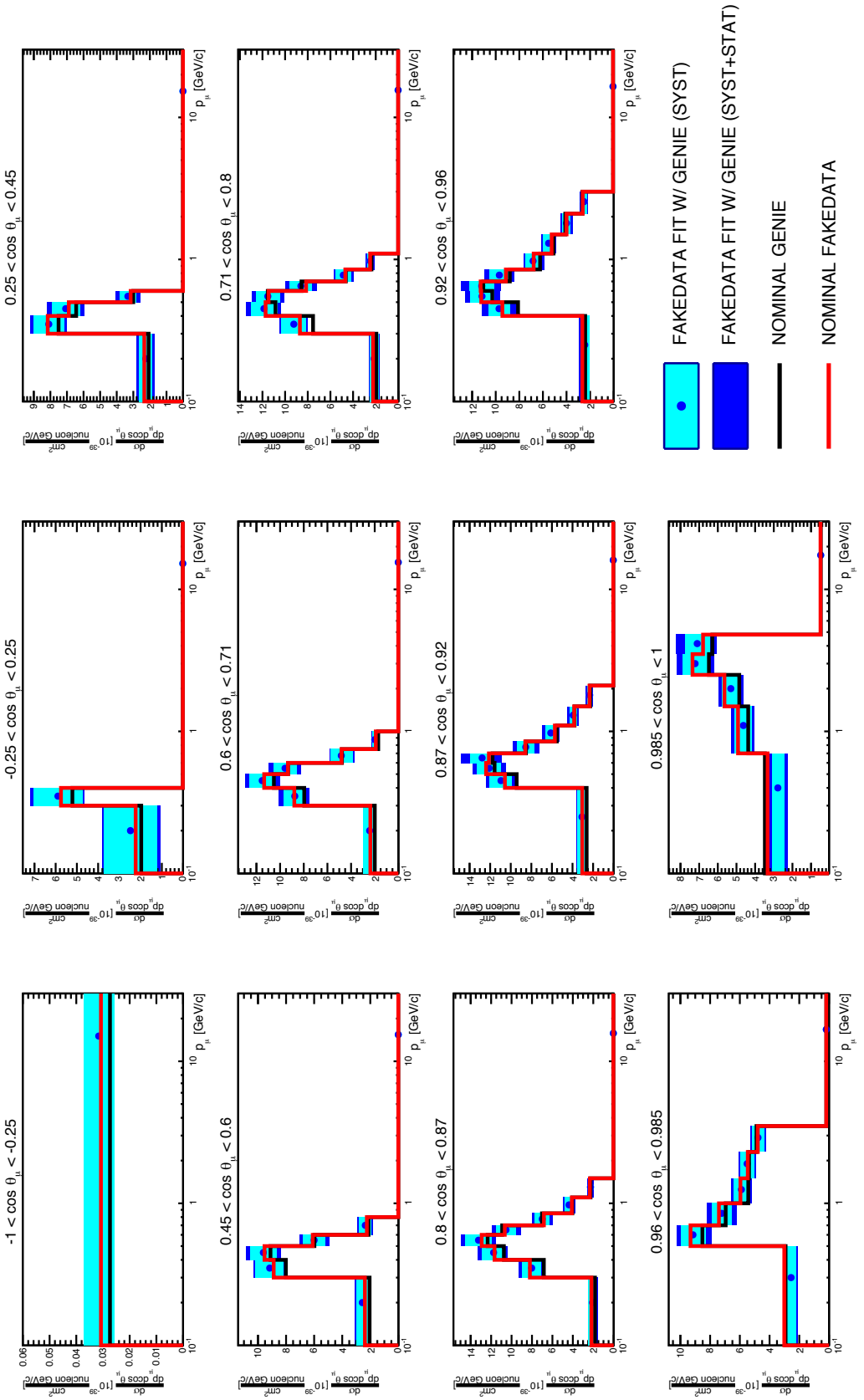


Figure G.9: Flux-integrated double differential cross section per nucleon for `GENIE` used as prior (black line), nominal `NEUT` used as fake data (red line) and average result after fitting 500 toys (light blue rectangles).

## G.4 Sidebands validation

The main features of the sidebands were discussed in Sec. 10.2. They are mainly composed by negative pions going in the forward direction coming out from NC or CCDIS interactions. In the cross section extraction, sidebands has been used to control the uncertainties associated to NC interactions and $\pi$ FSI. In Sec. 10.7.6 it was shown that the impact of the sidebands in the total errors is negligible. The main reason is that the dominant uncertainties are due to statistics and flux normalization, which are not constrained with sidebands. Nonetheless, it is interesting to study the distribution of events in the sidebands when nuisance parameters are included.

Firstly, a fake data study is used as validation step. The same fake data set as in Sec. G.3.4 is used, in which the NC interactions are scale up by a factor 1.9. Fig. G.10 shows the value of the nuisance parameter associated to such dial after 500 toys are fitted using as prior `NEUT` and applying fluctuations due to statistics and systematic uncertainties. The distribution is centered around the bias factor applied to the fake data. Moreover, the rate of event in the sidebands for each reconstructed bin is shown comparing the fake data, prior and fitted distributions. The fake data distribution is better reproduced by the fitted prediction.

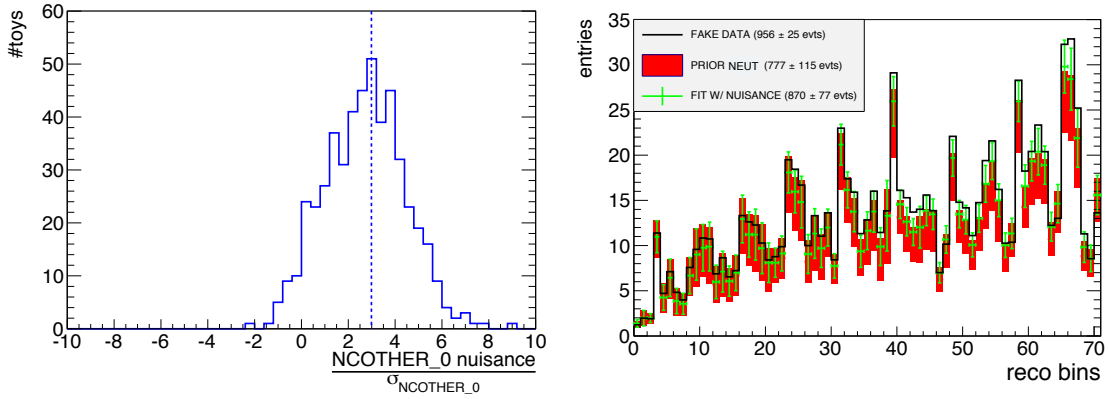


Figure G.10: Left: Distribution of the nuisance parameter associated to the `NCOTHER_0` dial after 500 toys using the same fake data set as in Sec. G.3.4. Dashed line indicates the bias factor applied to the fake data. Right: Number of events in the sidebands for each reconstructed bin. Each column represents a bin going from $0 = [-1 < \cos\theta_\mu < -0.25, 0\text{GeV/c} < p_\mu < 30\text{GeV/c}]$ to $70 = [0.985 < \cos\theta_\mu < 1, 4.8\text{GeV/c} < p_\mu < 30\text{GeV/c}]$.

Secondly, the result from real data are analyzed when the fit is perform using as prior both `NEUT` and `GENIE` (see Fig. G.11). Firstly, it is important to notice that in both cases the nuisance parameter associated to the NC interactions are centered around zero. In this case, the prior and fitted recon-

structed distribution are very similar in the case of NEUT. However, the prior prediction from GENIE underestimate the fitted distribution. It is important to notice that the fitted prediction using as prior NEUT and GENIE is equivalent when including the nuisance parameters.

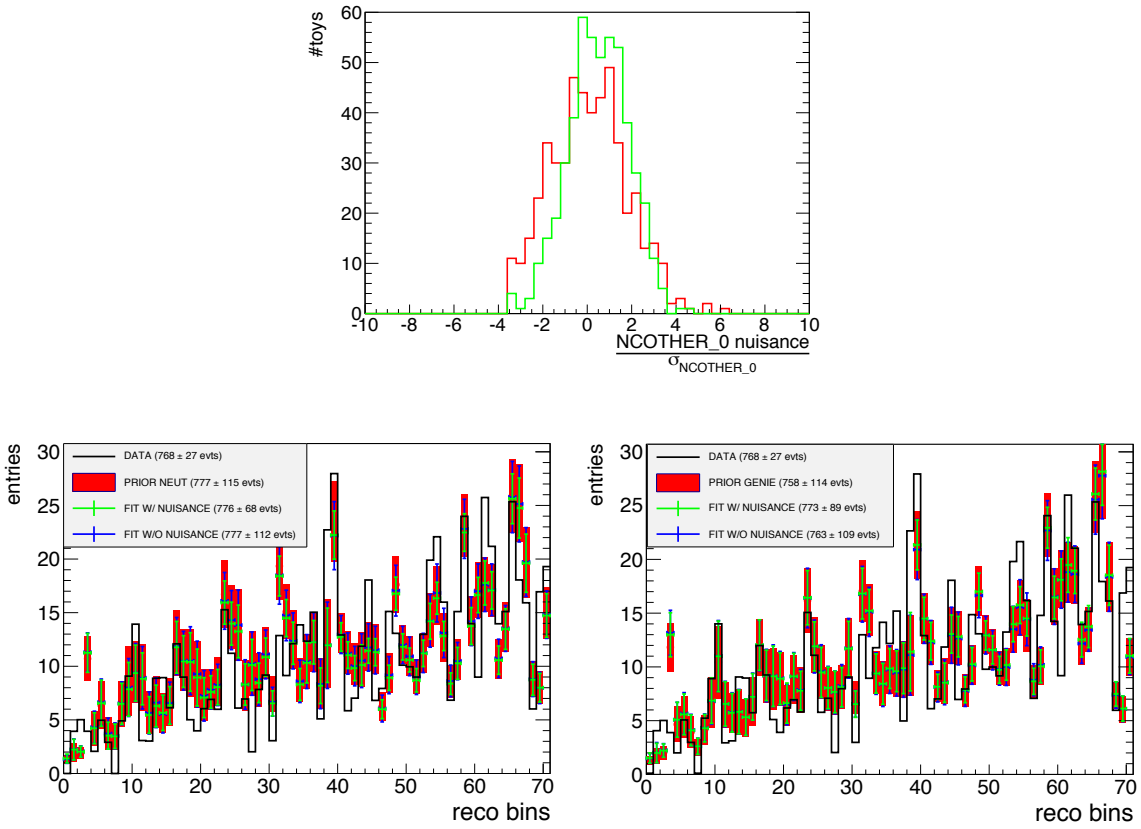


Figure G.11: Top: Distribution of the nuisance parameter associated to the NCOTHER_0 dial after 500 toys fitting the data with NEUT (red) and GENIE (green). Bottom: Number of events in the sidebands for each reconstructed bin after 500 toys fitting the data with NEUT (left) and GENIE (right). Each column represents a bin going from $0 = [-1 < \cos\theta_\mu < -0.25, 0\text{GeV/c} < p_\mu < 30\text{GeV/c}]$ to $70 = [0.985 < \cos\theta_\mu < 1, 4.8\text{GeV/c} < p_\mu < 30\text{GeV/c}]$.

# Bibliography


[1] J. Chadwick, *Possible Existence of a Neutron*, Nature, Volume 129, page 312 (1932).

[2] W. Heisenberg, *Uber den Bau der Atomkerne I*, Zeitschrift fur Physik, Volume 77, Issue 1, page 1 (1932).

[3] E. Fermi, *Versuch einer Theorie der -Strahlen I* Zeitschrift fr Physik, Volume 88, Issue 3, page 161 (1934).

[4] H. Bethe and R. Peierls, *The Neutrino*, Nature, Volume 133, page 532 (1934).

[5] B. Pontecorvo, Chalk River Lab, PD-205 report (1946).

[6] R. Davis, *Attempt to Detect the Antineutrinos from a Nuclear Reactor by the* $Cl^{37}(\nu^-, e^-)A^{37}$ *Reaction*, Physical Review 97, Volume 97, Issue 3, 766 (1955).

[7] F. Reines and C. Cowan *The Neutrino*, Nature, Volume 178, page 446 (1956).

[8] H. Yukawa, *On the Interaction of Elementary Particles I*, Proceedings of the Physico-Mathematical Society of Japan, Volume 17, page 48 (1935).

[9] S. Neddermeyer and C. Anderson, *Note on the Nature of Cosmic-Ray Particles*, Physical Review, Volume 51, Issue 10, 884 (1937).

[10] C. Lattes et al., *Processes involving charged mesons*, Nature, Volume 159, page 694 (1947).

[11] T. Lee and C. Yang, *Question of Parity Conservation in Weak Interactions*, Physical Review, Volume 104, Issue 1, 254 (1956).

[12] C. Wu et al., *Experimental Test of Parity Conservation in Beta Decay*, Physical Review, Volume 105, Issue 4, 769 (1957).

[13] R. Garwin, *Observations of the Failure of Conservation of Parity and Charge Conjugation in Meson Decays: the Magnetic Moment of the Free Muon*, Physical Review, Volume 105, Issue 4, 1415 (1957).

[14] L. Landau, *On the conservation laws for weak interactions*, Nuclear Physics Volume 3, Issue 1, page 127 (1957).

[15] A. Salam, *On parity conservation and neutrino mass*, Il Nuovo Cimento, Volume 5, Issue 1, page 299 (1957).

[16] T. Lee and C. Yang, *Parity Nonconservation and a Two-Component Theory of the Neutrino*, Physical Review, Volume 105, Issue 5, 1671 (1957).

[17] M. Goldhaver et al., *Helicity of Neutrinos*, Physical Review, Volume 109, Issue 3, 1015 (1958).

[18] R. Feynman and M. Gell-Mann, *Theory of the Fermi Interaction*, Physical Review, Volume 109, Issue 1, 193 (1958).

[19] E. Sudarshan and R. Marshak, *Chirality Invariance and the Universal Fermi Interaction* Physical Review, Volume 109, Issue 5, 1860 (1958).

[20] T. Fazzini et al., *Electron Decay of the Pion*, Physical Review Letters, Volume 1, Issue 7, 247 (1958).

[21] F. Reines et al., *Detection of $\bar{\nu}_e - e$ Scattering*, Physical Review Letters, Volume 37, Issue 6, 315 (1976).

[22] G. Danby et al., *Observation of High-Energy Neutrino Reactions and the Existence of Two Kinds of Neutrinos*, Physical Review Letters, Volume 9, Issue 1, 36 (1962).

[23] M. Perl et al., *Evidence for Anomalous Lepton Production in $e^+e$ Annihilation*, Physical Review Letters, Volume 35, Issue 22, 1489 (1975).

[24] DONUT Collaboration, *Observation of tau neutrino interactions*, Physics Letters B, Volume 504, Issue 3, page 218 (2001).

[25] LEP Collaborations, *Tests of the Standard Model*, International Europhysics Conference on High Energy Physics (1999).

[26] S. Weinberg, A Model of Leptons, Physical Review Letters, Volume 19, Issue 21, 1264 (1967).

[27] A. Salam, *Weak and Electromagnetic Interactions*, Proceedings of the Eighth Nobel Symposium, page 367 (1968).

[28] Gargamelle Neutrino Collaboration, *Observation of neutrino-like interactions without muon or electron in the Gargamelle neutrino experiment*, Nuclear Physics B, Volume 73, Issue 1, page 1 (1974).

[29] NuTeV Collaboration, *Precise Determination of Electroweak Parameters in Neutrino-Nucleon Scattering*, Physical Review Letters, Volume 88, Issue 9, 091802 (2002):

[30] D. Griffiths, *Introduction to Elementary Particles*, Wiley-VCH (2008).

[31] B. Pontecorvo, *Mesonium and anti-mesonium* Journal of Experimental and Theoretical Physics, Volume 6, page 429 (1957).

[32] B. Pontecorvo, *Inverse Beta Processes and Nonconservation of Lepton Charge* Journal of Experimental and Theoretical Physics, Volume 7, page 172 (1958).

[33] Z. Maki et al., *Remarks on the Unified Model of Elementary Particles* Progress of Theoretical Physics, Volume 28, Issue 5, page 870 (1962).

[34] B. Pontecorvo, *Neutrino Experiments and the Problem of Conservation of Leptonic Charge* Journal of Experimental and Theoretical Physics, Volume 26, page 984 (1968).

[35] R. Davis, Bulletin of the American Physical Society (1959).

[36] S. Bilenky and B. Pontecorvo, *Quark-lepton analogy and neutrino oscillations*, Physics Letters B, Volume 61, Issue 3, page 248 (1976).

[37] H. Fritsch and P. Minkowski, *Vectorlike weak currents, massive neutrinos, and neutrino beam oscillations*, Physics Letters B, Volume 62, Issue 1, page 72 (1976).

[38] S. Eliezer, A. Swift, *Experimental consequences of e mixing in neutrino beams*, Nuclear Physics B, Volume 105, Issue 1, page 45 (1976).

[39] L. Wolfenstein, *Neutrino oscillations in matter*, Physical Review D, Volume 17, Issue, 9, 2369 (1978).

[40] J. Bahcall et al., *10,000 Standard Solar Models: A Monte Carlo Simulation*, The Astrophysical Journal Supplement Series, Volume 165, Number 1 (2006).

[41] SAGE Collaboration, *Measurement of the solar neutrino capture rate with gallium metal. III. Results for the 20022007 data-taking period*, Physical Review C, Volume 80, Issue 1, 015807 (2009).

[42] GALLEX Collaboration, *GALLEX solar neutrino observations: results for GALLEX IV*, Physics Letters B, Volume 447, Issues 12, page 127 (1999).

[43] GNO Collaboration, *Complete results for five years of GNO solar neutrino observations*, Physics Letters B, Volume 616, Issues 3-4, page 174 (2005).

[44] K. S. Hirata et al., *Observation of B8 solar neutrinos in the Kamiokande-II detector*, Physical Review Letters, Volume 63, Issue 1, 16 (1989).

[45] Super-Kamiokande Collaboration, *Solar neutrino results in Super-Kamiokande-III* Physical Review D, Volume 83, Issue 5, 052010 (2011).

[46] SNO Collaboration, *Independent Measurement of the Total Active* $^8B$ *Solar Neutrino Flux Using an Array of* $^3He$ *Proportional Counters at the Sudbury Neutrino Observatory* , Physical Review Letters, Volume 101, Issue 11, 111301 (2008).

[47] Borexino Collaboration, *Final results of Borexino Phase-I on low-energy solar neutrino spectroscopy* , Physical Review D, Volume 89, Issue 11, 112007 (2014).

[48] M. Maltoni and A. Smirnov, *Solar neutrinos and neutrino physics*, The European Physical Journal A, Volume 52, Issue 87 (2016).

[49] P. Huber, *Determination of antineutrino spectra from nuclear reactors*, Physical Review C, Volume 84, Issue 2, 024617 (2011).

[50] M. Apollonio et al., *Limits on neutrino oscillations from the CHOOZ experiment*, Physics Letters B, Volume 466, Issues 2-4, page 415 (1999).

[51] F. Boehm et al., *Final results from the Palo Verde neutrino oscillation experiment*, Physical Review D, Volume 64, Issue 11, 112001 (2001).

[52] RENO Collaboration, *Observation of Reactor Electron Antineutrinos Disappearance in the RENO Experiment*, Physical Review Letters, Volume 108, Issue 19, 191802 (2012).

[53] Double Chooz Collaboration, *Indication of Reactor* $\bar{\nu}_e$ *Disappearance in the Double Chooz Experiment*, Physical Review Letters, Volume 108, Issue 13, 131801 (2012).

[54] Daya Bay Collaboration, *Observation of Electron-Antineutrino Disappearance at Daya Bay*, Physical Review Letters, Volume 108, Issue 17, 171803 (2012).

[55] RENO Collaboration, *Observation of Energy and Baseline Dependent Reactor Antineutrino Disappearance in the RENO Experiment*, Physical Review Letters, Volume 116, Issue 21, 211801 (2016).

[56] M. Honda et al., *Atmospheric neutrino flux calculation using the NRLMSISE-00 atmospheric model*, Physical Review D, Volume 92, Issue 2, 023004 (2015).

[57] Y. Fukuda et al., *Atmospheric vve ratio in the multi-GeV energy range*, Physics Letters B, Volume 335, Issue 2, page 237 (1994).

[58] D. Casper et al., *Measurement of atmospheric neutrino composition with the IMB-3 detector*, Physical Review Letters, Volume 66, Issue 20, 2561 (1991).

[59] Super-Kamiokande Collaboration, *Evidence for Oscillation of Atmospheric Neutrinos* Physical Review Letters, Volume 81, Issue 8, 1562 (1998).

[60] MACRO collaboration, *Measurement of the atmospheric neutrino-induced upgoing muon flux using MACRO*, Physics Letters B, Volume 434, Issues 34, page 451 (1998).

[61] MINOS collaboration, *Measurements of atmospheric neutrinos and antineutrinos in the MINOS far detector*, Physical Review D, Volume 86, Issue 5, 052007 (2012).

[62] NA61/SHINE Collaboration, *NA61/SHINE facility at the CERN SPS: beams and detector system*, Journal of Instrumentation, Volume 9, page 06005 (2014).

[63] K2K Collaboration, *Measurement of neutrino oscillation by the K2K experiment*, Physical Review D, Volume 74, Issue 7, 072003 (2006).

[64] MINOS Collaboration, *Measurement of the Neutrino Mass Splitting and Flavor Mixing by MINOS*, Physical Review Letters, Volume 106, Issue 18, 181801 (2011).

[65] T2K Collaboration, *Observation of Electron Neutrino Appearance in a Muon Neutrino Beam*, Physics Review Letters, Volume 112, Issue 6, 061802 (2014).

[66] NOVA Collaboration, *First Measurement of Electron Neutrino Appearance in NOvA*, Physics Review Letters, Volume 116, Issue 15, 151806 (2016).

[67] M. Martini et al., *Energy reconstruction effects in neutrino oscillation experiments and implications for the analysis*, Physical Review D, Volume 87, Issue 1, 013009 (2012).

[68] J. Nieves et al., *Neutrino energy reconstruction and the shape of the charged current quasielastic-like total cross section*, Physical Review D, Volume 85, Issue 11, 113008 (2012).

[69] A.Ankowski et al., *Comparison of the calorimetric and kinematic methods of neutrino energy reconstruction in disappearance experiments*, Physical Review D, Volume 92, Issue 7, 073014 (2015).

[70] P. Dirac, *The Quantum Theory of the Emission and Absorption of Radiation*, Proceedings of the Royal Society A, Volume 114 Issue 767, page 243265 (1927).

[71] R. Feynman, *Space-Time Approach to Quantum Electrodynamics*, Physical Review, Volume 76, Issue 6, 769 (1949).

[72] A. Thomas and W. Weise, *The Structure of the Nucleon*, Wiley-VCH (2001).

[73] P. Dirac, *Quantenmechanik der StoBvorgange*, Zeitschrift fr Physik, Volume 38, Issue 11, page 803 (1926).

[74] C. Llewellyn Smith, *Neutrino reactions at accelerator energies*, Volume 3, Issue 5, page 261 (1972).

[75] R. Feynman and M. Gell Mann. *Theory of the Fermi Interaction* Physical Review, Volume 109, Issue 1, 193 (1958).

[76] F. Ernst et al., *Electromagnetic Form Factors of the Nucleon* Physical Review Volume 119, Issue 3, 1105 (1960).

[77] S. Pacetti et al., *Proton electromagnetic form factors: Basic notions, present achievements and future perspectives* Physics Reports, Volume 550-551, page 1 (2015).

[78] J. Reich et al., *A measurement of the beta asymmetry in neutron decay with PERKEO II*, Nuclear Instruments and Methods in Physics Research A, Volume 440, page 535 (2000).

[79] V. Bernard et al., *Axial structure of the nucleon*, Journal of Physics G: Nuclear and Particle Physics, Volume 28, Number 1 (2001).

[80] U. Mosel, *Neutrino Interactions with Nucleons and Nuclei: Importance for Long-Baseline Experiments*, Annual Review of Nuclear and Particle Science, Volume 66, page 171 (2016).

[81] T. Leitner et al., *Charged current neutrino-nucleus interactions at intermediate energies*, Physical Review C Volumne 73, Issue 6, 065502 (2006).

[82] D. Rein and L. Sehgal, *Neutrino-excitation of baryon resonances and single pion production*, Annals of Physics, Volume 133, Issue 1, page 79 (1981).

[83] J. Bjorken, *Asymptotic Sum Rules at Infinite Momentum*, Physical Review, Volume 179 Issue 5, 1547 (1969).

[84] C. Callan and D. Gross, *High-Energy Electroproduction and the Constitution of the Electric Current*, Physical Review Letters, Volume 22, Issue 4, 156 (1969).

[85] R. Feynman, *Very High-Energy Collisions of Hadrons*, Physical Review Letters, Volume 23, Issue 24, 1415 (1969).

[86] M. Gluck et al., *Dynamical parton distributions revisited*, The European Physical Journal C - Particles and Fields, Volume 5, Issue 3, page 461 (1998).

[87] O. Benhar et al., *Electron- and neutrino-nucleus scattering in the impulse approximation regime*, Physical Review D, Volume 72, Issue 5, 05300 (2005).

[88] O. Benhar et al., *Spectral function of finite nuclei and scattering of GeV electrons*, Nuclear Physics A Volume 579, Issues 34, page 493 (1994).

[89] A. Bodek et al., *Effective spectral function for quasielastic scattering on nuclei*, The European Physical Journal C, Volume 74, Issue 3091 (2014).

[90] R. Smith and E. Moniz, *Neutrino reactions on nuclear targets*, Nuclear Physics B, Volume 43, page 605 (1972).

[91] T. Kosmas and E. Oset, *Charged current neutrino-nucleus reaction cross sections at intermediate energies*, Physical Review C, Volume 53, Issue 3, 1409 (1996).

[92] J. E. Amaro et al., *Using electron scattering superscaling to predict charge-changing neutrino cross sections in nuclei*, Physical Review C, Volume 71, Issue 1, 015501 (2005).

[93] M. Martini et al., *Neutrino and antineutrino quasielastic interactions with nuclei*, Physical Review C, Volume 81, Issue 4, 045502 (2010).

[94] J. Nieves et al., *Inclusive charged-current neutrino-nucleus reactions*, Physical Review C, Volume 83, Issue 4, 045501 (2011).

[95] K. Gallmeister et al., *Neutrino-induced reactions on nuclei*, Physical Review C, Volume 94, Issue 3, 035502 (2016).

[96] L. Salcedo et al., *Computer simulation of inclusive pion nuclear reactions*, Nuclear Physics A, Volume 484, Issues 34, page 557 (1988).

[97] R. Merenyi et al., *Determination of pion intranuclear rescattering rates in $\nu_\mu Ne$ versus $\nu_\mu D$ interactions for the atmospheric $\nu$ flux*, Physical Review D, Volume 45, Issue 3, 743 (1992).

[98] C. Andreopoulos et al., *The GENIE neutrino Monte Carlo generator*, Nuclear Instruments and Methods in Physics Research Section A: Accelerators, Spectrometers, Detectors and Associated Equipment, Volume 614, Issue 1, page 87 (2010).

[99] Y. Hayato, *A neutrino interaction simualtion program library NEUT*, Acta Physica Polonica B, Volume 40, Number 9, page 2477 (2009).

[100] R. Bradford et al., *A New Parameterization of the Nucleon Elastic Form Factors*, Nuclear Physics B - Proceedings Supplements, Volume 159, page 127 (2006).

[101] A. Bodek and U. Yang, *Higher twist, $\xi w$ scaling, and effective LO PDFs for lepton scattering in the few GeV region*, Journal of Physics G: Nuclear and Particle Physics, Volume 29, Number 8 (2003).

[102] A. Bodek and U. Yang, *A Unified Model for inelastic eN and $\nu$N cross sections at all $Q^2$*, AIP Conference Procedings, 792, 257 (2005).

[103] Z. Koba et al., *Scaling of multiplicity distributions in high energy hadron collisions*, Nuclear Physics B, Volume 40, page 317 (1972).

[104] T. Sjostrand et al., *PYTHIA 6.4 physics and manual*, Journal of High Energy Physics, Volume 2006, page 26 (2006).

[105] T. Sjostrand, *High-energy-physics event generation with PYTHIA 5.7 and JETSET 7.4*, Computer Physics Communications, Volume 82, Issue 1, page 74 (1994).

[106] K. Graczyk and J. Sobczyk, *Form factors in the quark resonance model*, Physical Review D, Volume 77, Issue 5, 053001 (2008).

[107] K. Kuzmin et al., *Axial masses in quasielastic neutrino scattering and single-pion neutrinoproduction on nucleons and nuclei*, Acta Physica Polonica B, Volume 37, Number 8, page 2337 (2006).

[108] A. Bodek and J. Ritchie, *Further studies of fermi motion effects in lepton scattering from nuclear targets*, Physical Review D, Volume 24, Issue 5, 1400 (1981).

[109] C. De Jager et al., *Nuclear charge- and magnetization-density-distribution parameters from elastic electron scattering*, Atomic Data and Nuclear Data Tables, Volume 14, Issues 56, page 479 (1974).

[110] R. Woods and D. Saxon, *Diffuse Surface Optical Model for Nucleon-Nuclei Scattering*, Physical Review, Volume 95, Issue 2, 577 (1954).

[111] D. Rein and L. Sehgal, *Coherent $\pi^0$ production in neutrino reactions*, Nuclear Physics B, Volume 223, Issue 1, page 29 (1983).

[112] D. Rein and L. Sehgal, *PCAC and the deficit of forward muons in $\pi^+$ production by neutrinos*, Physics Letters B, Volume 657, Issues 4-5, page 207 (2007). Physics Letters B

[113] D. Ashery et al., *True absorption and scattering of pions on nuclei*, Physical Review C, Volume 23, Issue 5, 2173 (1981).

[114] H. Bertini, *Nonelastic Interactions of Nucleons and $\pi$ Mesons with Complex Nuclei at Energies Below 3 GeV*, Physical Review C, Volume 6, Issue 2, 631 (1972).

[115] S. Lindenbaum and R. Sternheimer, *Isobaric Nucleon Model for Pion Production in Nucleon-Nucleon Collisions*, Physical Review, Volume 105, Issue 6, 1874 (1957).

[116] S. Mashnik et al, *CEM03 and LAQGSM03new modeling tools for nuclear applications*, Journal of Physics: Conference Series, Volume 41, page 340 (2006).

[117] SciBooNE Collaboration, *Measurement of inclusive charged current interactions on carbon in a few-GeV neutrino beam*, Physical Review D, Volume 83, Issue 1, 012005 (2011).

[118] NOMAD Collaboration, *A precise measurement of the muon neutrinonucleon inclusive charged current cross section off an isoscalar target in the energy range $2.5 < E_\nu < 40$ GeV by NOMAD*, Physics Letters B, Volume 660, Issues 12, page 19 (2008).

[119] T2K Collaboration, *Measurement of the inclusive $\nu_\mu$ charged current cross section on carbon in the near detector of the T2K experiment*, Physical Review D, Volume 87, Issue 9, 092003 (2013).

[120] T2K Collaboration, *Measurement of the inclusive $\nu_\mu$ charged current cross section on iron and hydrocarbon in the T2K on-axis neutrino beam*, Physical Review D, Volume 90, Issue 5, 052010 (2014).

[121] MINERvA Collaboration, *Measurements of the inclusive neutrino and antineutrino charged current cross sections in MINERvA using the low-$\nu$ flux method*, Physical Review D, Volume 94, Issue 11, 112007 (2016).

[122] NOMAD Collaboration, *A study of quasi-elastic muon neutrino and antineutrino scattering in the NOMAD experiment*, The European Physical Journal C, Volume 63, Issue 3, page 355 (2009).

[123] MiniBooNE Collaboration, *First measurement of the muon neutrino charged current quasielastic double differential cross section*, Physical Review D, Volume 81, Issue 9, 092005 (2010).

[124] MINERvA Collaboration, *Measurement of Muon Neutrino Quasielastic Scattering on a Hydrocarbon Target at $E_\nu \sim 3.5GeV$*, Physical Review Letters, Volume 111, Issue 2, 022502 (2013).

[125] T2K Collaboration, *Measurement of the $\nu_\mu$ charged current quasielastic cross section on carbon with the T2K on-axis neutrino beam*, Physical Review D, Volume 91, Issue 11, 112002 (2015).

[126] T2K Collaboration, *Measurement of double-differential muon neutrino charged-current interactions on C8H8 without pions in the final state using the T2K off-axis beam*, Physical Review D, Volume 93, Issue 11, 112012 (2016).

[127] T2K Collaboration, *The T2K experiment*, Nuclear Instruments and Methods in Physics Research Section A: Accelerators, Spectrometers, Detectors and Associated Equipment, Volume 659, Issue 1, page 106 (2011).

[128] A. Ichikawa, *Design concept of the magnetic horn system for the T2K neutrino beam*, Nuclear Instruments and Methods in Physics Research Section A: Accelerators, Spectrometers, Detectors and Associated Equipment, Volume 690, page 27 (2012).

[129] K. Matsuoka et al., *Design and performance of the muon monitor for the T2K neutrino oscillation experiment*, Nuclear Instruments and Methods in Physics Research Section A: Accelerators, Spectrometers, Detectors and Associated Equipment, Volume 624, Issue 3, page 591 (2010).

[130] T2K Collaboration, *T2K neutrino flux prediction*, Physical Review D, Volume 87, Issue 1, 012001 (2013).

[131] G. Battistoni et al., *The FLUKA code: description and benchmarking*, AIP Conference Proceedings, Volume 896, Issue 1 (2007).

[132] R. Brun et al., *GEANT: Detector description and simulation tool*, CERN-W5013 (1994).

[133] C.Zeitnitz and T.Gabriel, *The GEANT-CALOR interface*, Proceedings of International Conference on Calorimetry in High Energy Physics, Page 376 (1993).

[134] T2K collaboration, *Measurements of the T2K neutrino beam properties using the INGRID on-axis near detector*, Nuclear Instruments and Methods in Physics Research Section A: Accelerators, Spectrometers, Detectors and Associated Equipment, Volume 694, page 211 (2012).

[135] T2K Collaboration, *The T2K ND280 off-axis pizero detector*, Nuclear Instruments and Methods in Physics Research Section A: Accelerators, Spectrometers, Detectors and Associated Equipment, Volume 686, page 48 (2012)

[136] N. Abgrall et al., *Time projection chambers for the T2K near detectors*, Nuclear Instruments and Methods in Physics Research Section A: Accelerators, Spectrometers, Detectors and Associated Equipment, Volume 637, Issue 1, page 25 (2011).

[137] P. Amaudruz et al., *The T2K fine-grained detectors*, Nuclear Instruments and Methods in Physics Research Section A: Accelerators, Spectrometers, Detectors and Associated Equipment, Volume 696, page 1 (2012).

[138] D. Allan et al., *The electromagnetic calorimeter for the T2K near detector ND280*, Journal of Instrumentation, Volume 8 (2013).

[139] S. Aoki et al., *The T2K Side Muon Range Detector (SMRD)*, Nuclear Instruments and Methods in Physics Research Section A: Accelerators, Spectrometers, Detectors and Associated Equipment, Volume 698, page 135 (2013).

[140] S. Assylbekov et al., *The T2K ND280 off-axis pizero detector*, Nuclear Instruments and Methods in Physics Research Section A: Accelerators, Spectrometers, Detectors and Associated Equipment, Volume 686, page 48 (2012).

[141] E. Frank et al., *A dedicated device for measuring the magnetic field of the ND280 magnet in the T2K experiment*, Journal of Instrumentation, Volume 7 (2012).

[142] C. Arnault, *CMT: A software configuration management tool*, International Conference on Computing in High-Energy Physics and Nuclear Physics (2000).

[143] R. Brun et al., *ROOT An object oriented data analysis framework*, Nuclear Instruments and Methods in Physics Research Section A: Accelerators, Spectrometers, Detectors and Associated Equipment, Volume 389, Issues 12, page 81 (1997).

[144] S. Agostinellia et al., *Geant4a simulation toolkit*, Nuclear Instruments and Methods in Physics Research Section A: Accelerators, Spectrometers, Detectors and Associated Equipment, Volume 506, Issue 3, page 250 (2003).

[145] B. Berliner and J. Polk, *CVS - Concurrent version system*, `http://www.nongnu.org/cvs` (2001).

[146] A. Cervera-Villanueva et al., *RecPack a reconstruction toolkit*, Nuclear Instruments and Methods in Physics Research Section A: Accelerators, Spectrometers, Detectors and Associated Equipment, Volume 534, Issues 1-2, page 180 (2004).

[147] DUNE collaboration, *Long-Baseline Neutrino Facility (LBNF) and Deep Underground Neutrino Experiment (DUNE) Conceptual Design Report Volume 2: The Physics Program for DUNE at LBNF* . URL: `http://arxiv.org/abs/1512.06148`.

[148] HyperK collaboration, *Letter of Intent: The Hyper-Kamiokande Experiment. Detector Design and Physics Potential*. URL: `http://arxiv.org/abs/1109.3262v1`.

[149] T2K collaboration, *Proposal for an Extended Run of T2K to* $20 \times 10^{21}$ *POT*. URL: `https://arxiv.org/abs/1609.04111`.

[150] G. Bellettini et al., *Proton-nuclei cross sections at 20 GeV*, Nuclear Physics, Volume 79, Issue 3, page 609 (1966).

[151] HARP Collaboration, *Forward production of charged pions with incident* $\pi^{\pm}$ *on nuclear targets measured at the CERN PS*, Nuclear Physics A, Volume 821, Issues 14, page 118 (2009).

[152] D. Ashery et al., *True absorption and scattering of pions on nuclei*, Physical Review C, Volume 23, Issue 5, 2173 (1981).

[153] A. Saunders et al., *Reaction and total cross sections for low energy* $\pi^+$ *and* $\pi^-$ *on isospin zero nuclei*, Physical Review C, Volume 54, Issue 4, 1745 (1996).

[154] M. Jones et al., *Pion absorption above the* $\Delta(1232)$ *resonance*, Physical Review C, Volume 48, Issue 6, 2800 (1993).

[155] D. Ashery et al., *Inclusive pion single-charge-exchange reactions*, Physical Review C, Volume 30, Issue 3, 946 (1984).

[156] E. Bellotti et al., *The $(\pi^+, \pi N)$ reactions on carbon at 130 MeV: A bubble-chamber experiment*, Il Nuovo Cimento A, Volume 14, Issue 3, page 567 (1973).

[157] I. Navon et al., *True Absorption and Scattering of 125-MeV Pions on Nuclei*, Physical Review Letters, Volume 42, Issue 22, 1465 (1979).

[158] H. Hilscher et al., *An experimental test of the analogy between radiative pion absorption and muon capture in $^{12}C$*, Nuclear Physics A, Volume 158, Issue 2, page 584 (1970).

[159] F. Binon et al., *Scattering of negative pions on carbon*, Nuclear Physics B, Volume 17, Issue 1, page 168 (1970).

[160] C. Wilkinson et al., *Testing charged current quasi-elastic and multinucleon interaction models in the NEUT neutrino interaction generator with published datasets from the MiniBooNE and MINERA experiments*, Physical Review D, Volume 93, Issue 7, 072010 (2016).

[161] MINERvA Collaboration, *Measurement of Coherent Production of $\pi^{\pm}$ in Neutrino and Antineutrino Beams on Carbon from $E_\nu$ of 1.5 to 20 GeV*, Physical Review Letters, Volume 113, Issue 26, 261802 (2014).

[162] SciBooNE Collaboration, *Search for charged current coherent pion production on carbon in a few-GeV neutrino beam*, Physical Review D, Volume 78, Issue 11, 112004 (2008).

[163] SciBooNE Collaboration, *Improved measurement of neutral current coherent $\pi^0$ production on carbon in a few-GeV neutrino beam*, Physical Review D, Volume 81, Issue 11, 111102 (2010).

[164] MINOS Collaboration, *Neutrino and antineutrino inclusive charged-current cross section measurements with the MINOS near detector*, Physical Review D, Volume 81, Issue 7, 072002 (2010).

[165] M. Day and K. McFarland, *Differences in quasielastic cross sections of muon and electron neutrinos*, Physical Review D, Volume 86, Issue 5, 053003 (2012).

[166] T. Golan et al., *NuWro: the Wroclaw Monte Carlo Generator of Neutrino Interactions*, Nuclear Physics B - Proceedings Supplements, Volume 229-232, page 499 (2012).

[167] T2K Collaboration, *Combined Analysis of Neutrino and Antineutrino Oscillations at T2K*, Physics Review Letters, Volume 118, Issue 15, 151801 (2017).